EUROPEAN LABORATORY FOR PARTICLE PHYSICS

CERN-EP/99-104
15 July 1999

Measurement of the Z Resonance Parameters at LEP

The ALEPH Collaboration

Abstract

The properties of the Z resonance are measured from the analysis of 4.5 million Z decays into fermion pairs collected with the ALEPH detector at LEP. The data are consistent with lepton universality. The resonance parameters are measured to be $M_{\mathrm{Z}} = (91.1885 \pm 0.0031)\ \mathrm{GeV}/c^2$, $\Gamma_{\mathrm{Z}} = (2.4951 \pm 0.0043)$ GeV, $\sigma^0_{\mathrm{had}} = (41.559 \pm 0.058)$ nb and, combining the three lepton flavours, $R_\ell = 20.725 \pm 0.039$. The corresponding number of light neutrino species is $N_\nu = 2.983 \pm 0.013$ and the strong coupling constant is $\alpha_s(M_{\mathrm{Z}}) = 0.114 \pm 0.004 \pm 0.002_{\mathrm{QCD}} + 0.005 \log_{10}\left[\frac{M_{\mathrm{H}}}{150\,\mathrm{GeV}/c^2}\right]$. The lepton pair forward-backward asymmetry is measured to be $\mathrm{A}^{0,\ell}_{\mathrm{FB}} = 0.0173 \pm 0.0016$ from which the effective weak mixing angle is derived: $\sin^2\theta^{\mathrm{lept}}_{\mathrm{eff}} = 0.23089 \pm 0.00089$. The measurement of the leptonic width $\Gamma_{\ell\ell} = 84.02 \pm 0.15$ MeV leads to a determination of the effective ρ parameter $\rho^{\mathrm{lept}}_{\mathrm{eff}} = 1.0064 \pm 0.0018$. The data support the Standard Model and favour a light Higgs.

(To be submitted to The European Physical Journal C)

Dedicated to the memory of Elizabeth Bishop Martin who died suddenly on March 16, 1999

The ALEPH Collaboration

R. Barate, D. Decamp, P. Ghez, C. Goy, J.-P. Lees, A. Lucotte, E. Merle, M.-N. Minard, B. Pietrzyk

Laboratoire de Physique des Particules (LAPP), IN^{2}P^3-CNRS, F-74019 Annecy-le-Vieux Cedex, France

R. Alemany, M.P. Casado, M. Chmeissani, P. Comas, J.M. Crespo, E. Fernandez, M. Fernandez-Bosman, Ll. Garrido, E. Graugès, A. Juste, M. Martinez, G. Merino, R. Miquel, Ll.M. Mir, S. Orteu, A. Pacheco, I.C. Park, J. Perlas, I. Riu, F. Sanchez

Institut de Física d'Altes Energies, Universitat Autònoma de Barcelona, E-08193 Bellaterra (Barcelona), Spain[7]

A. Colaleo, D. Creanza, M. de Palma, G. Iaselli, G. Maggi, M. Maggi, S. Nuzzo, A. Ranieri, G. Raso, F. Ruggieri, G. Selvaggi, L. Silvestris, P. Tempesta, A. Tricomi,[3] G. Zito

Dipartimento di Fisica, INFN Sezione di Bari, I-70126 Bari, Italy

X. Huang, J. Lin, Q. Ouyang, T. Wang, Y. Xie, R. Xu, S. Xue, J. Zhang, L. Zhang, W. Zhao

Institute of High-Energy Physics, Academia Sinica, Beijing, The People's Republic of China[8]

D. Abbaneo, A. Bazarko, U. Becker, G. Boix,[6] F. Bird, E. Blucher, G. Bonvicini, P. Bright-Thomas, M. Cattaneo, F. Cerutti, V. Ciulli, G. Dissertori, H. Drevermann, R.W. Forty, M. Frank, T.C. Greening, R. Hagelberg, A.W. Halley, J.B. Hansen, J. Harvey, R. Jacobsen, P. Janot, B. Jost, J. Knobloch, P. Lazeyras, I. Lehraus, P. Maley, P. Mato, J. May, A. Moutoussi, F. Ranjard, L. Rolandi, D. Schlatter, M. Schmitt, O. Schneider, P. Spagnolo, W. Tejessy, F. Teubert, I.R. Tomalin, E. Tournefier, R. Veenhof, W. Wiedenmann, A.E. Wright

European Laboratory for Particle Physics (CERN), CH-1211 Geneva 23, Switzerland

Z. Ajaltouni, F. Badaud, G. Chazelle, O. Deschamps, A. Falvard, C. Ferdi, P. Gay, C. Guicheney, P. Henrard, J. Jousset, B. Michel, S. Monteil, J-C. Montret, D. Pallin, P. Perret, F. Podlyski

Laboratoire de Physique Corpusculaire, Université Blaise Pascal, IN^{2}P^3-CNRS, Clermont-Ferrand, F-63177 Aubière, France

H. Bertelsen, T. Fernley, F. Hansen, J.D. Hansen, J.R. Hansen, P.H. Hansen, A. Lindahl, R. Mollerud, B.S. Nilsson, B. Rensch, A. Wäänänen

Niels Bohr Institute, DK-2100 Copenhagen, Denmark[9]

G. Daskalakis, A. Kyriakis, C. Markou, E. Simopoulou, I. Siotis, A. Vayaki

Nuclear Research Center Demokritos (NRCD), GR-15310 Attiki, Greece

A. Blondel, G. Bonneaud, J.-C. Brient, A. Rougé, M. Rumpf, M. Swynghedauw, R. Tanaka, M. Verderi, H. Videau

Laboratoire de Physique Nucléaire et des Hautes Energies, Ecole Polytechnique, IN^{2}P^3-CNRS, F-91128 Palaiseau Cedex, France

E. Focardi, G. Parrini, K. Zachariadou

Dipartimento di Fisica, Università di Firenze, INFN Sezione di Firenze, I-50125 Firenze, Italy

R. Cavanaugh, M. Corden, C. Georgiopoulos

Supercomputer Computations Research Institute, Florida State University, Tallahassee, FL 32306-4052, USA [13,14]

A. Antonelli, G. Bencivenni, G. Bologna,[4] F. Bossi, P. Campana, G. Capon, V. Chiarella, G. Felici, P. Laurelli, G. Mannocchi,[1,5] F. Murtas, G.P. Murtas, L. Passalacqua, M. Pepe-Altarelli[1], P. Picchi

Laboratori Nazionali dell'INFN (LNF-INFN), I-00044 Frascati, Italy

P. Colrain, I. ten Have, I.S. Hughes, I.G. Knowles, J.G. Lynch, W.T. Morton, C. Raine, P. Reeves, V. O'Shea, J.M. Scarr, K. Smith, A.S. Thompson, R.M. Turnbull

Department of Physics and Astronomy, University of Glasgow, Glasgow G12 8QQ,United Kingdom[10]

O. Buchmüller, S. Dhamotharan, C. Geweniger, P. Hanke, G. Hansper, V. Hepp, E.E. Kluge, A. Putzer, J. Sommer, K. Tittel, S. Werner, M. Wunsch

Institut für Hochenergiephysik, Universität Heidelberg, D-69120 Heidelberg, Germany[16]

R. Beuselinck, D.M. Binnie, W. Cameron, P.J. Dornan,[1] M. Girone, S. Goodsir, E.B. Martin, N. Marinelli, J. Nash, A. Sciabà, J.K. Sedgbeer, E. Thomson, M.D. Williams

Department of Physics, Imperial College, London SW7 2BZ, United Kingdom[10]

V.M. Ghete, P. Girtler, E. Kneringer, D. Kuhn, G. Rudolph

Institut für Experimentalphysik, Universität Innsbruck, A-6020 Innsbruck, Austria[12]

C.K. Bowdery, P.G. Buck, A.J. Finch, F. Foster, G. Hughes, R.W.L. Jones, N.R. Keemer, N.A. Robertson, T. Sloan, S.W. Snow, M.I. Williams

Department of Physics, University of Lancaster, Lancaster LA1 4YB, United Kingdom[10]

L.A.T. Bauerdick, P. van Gemmeren, I. Giehl, K. Jakobs, M. Kasemann, K. Kleinknecht, G. Quast, B. Renk, E. Rohne, H.-G. Sander, M. Schmelling, H. Wachsmuth, R. Wanke, C. Zeitnitz

Institut für Physik, Universität Mainz, D-55099 Mainz, Germany[16]

J.J. Aubert, C. Benchouk, A. Bonissent, J. Carr,[1] P. Coyle, F. Etienne, F. Motsch, P. Payre, D. Rousseau, M. Talby, M. Thulasidas

Centre de Physique des Particules, Faculté des Sciences de Luminy, IN^{2}P^3-CNRS, F-13288 Marseille, France

M. Aleppo, M. Antonelli, F. Ragusa

Dipartimento di Fisica, Università di Milano e INFN Sezione di Milano, I-20133 Milano, Italy

V. Büscher, H. Dietl, G. Ganis, K. Hüttmann, G. Lütjens, C. Mannert, W. Männer, H.-G. Moser, S. Schael, R. Settles, H. Seywerd, H. Stenzel, W. Wiedenmann, G. Wolf

Max-Planck-Institut für Physik, Werner-Heisenberg-Institut, D-80805 München, Germany[16]

P. Azzurri, J. Boucrot, O. Callot, S. Chen, A. Cordier, M. Davier, L. Duflot, J.-F. Grivaz, Ph. Heusse, A. Jacholkowska,[1] F. Le Diberder, J. Lefrançois, A.-M. Lutz, M.-H. Schune, J.-J. Veillet, I. Videau,[1] D. Zerwas

Laboratoire de l'Accélérateur Linéaire, Université de Paris-Sud, IN^{2}P^3-CNRS, F-91898 Orsay Cedex, France

G. Bagliesi, S. Bettarini, T. Boccali, C. Bozzi, G. Calderini, R. Dell'Orso, R. Fantechi, I. Ferrante, F. Fidecaro, L. Foà, A. Giassi, A. Gregorio, F. Ligabue, A. Lusiani, P.S. Marrocchesi, A. Messineo, F. Palla, G. Rizzo, G. Sanguinetti, G. Sguazzoni, J. Steinberger, R. Tenchini, C. Vannini, A. Venturi, P.G. Verdini

Dipartimento di Fisica dell'Università, INFN Sezione di Pisa, e Scuola Normale Superiore, I-56010 Pisa, Italy

G.A. Blair, G. Cowan, M.G. Green, T. Medcalf, J.A. Strong, J.H. von Wimmersperg-Toeller

Department of Physics, Royal Holloway & Bedford New College, University of London, Surrey TW20 OEX, United Kingdom[10]

D.R. Botterill, R.W. Clifft, T.R. Edgecock, M. Edwards, S.J. Haywood, P.R. Norton, J.C. Thompson

Particle Physics Dept., Rutherford Appleton Laboratory, Chilton, Didcot, Oxon OX11 OQX, United Kingdom[10]

B. Bloch-Devaux, P. Colas, S. Emery, W. Kozanecki, E. Lançon, M.-C. Lemaire, E. Locci, P. Perez, J. Rander, J.-F. Renardy, A. Roussarie, J.-P. Schuller, J. Schwindling, B. Vallage

CEA, DAPNIA/Service de Physique des Particules, CE-Saclay, F-91191 Gif-sur-Yvette Cedex, France[15]

S.N. Black, J.H. Dann, H.Y. Kim, N. Konstantinidis, A.M. Litke, M.A. McNeil, G. Taylor

Institute for Particle Physics, University of California at Santa Cruz, Santa Cruz, CA 95064, USA[2]

C.N. Booth, S. Cartwright, F. Combley, M. Lehto, L.F. Thompson

Department of Physics, University of Sheffield, Sheffield S3 7RH, United Kingdom[10]

K. Affholderbach, E. Barberio, A. Böhrer, S. Brandt, H. Burkhardt, E. Feigl, C. Grupen, J. Hess, G. Lutters, H. Meinhard, J. Minguet-Rodriguez, L. Mirabito, A. Misiejuk, E. Neugebauer, G. Prange, F. Rivera, P. Saraiva, U. Schäfer, H. Seywerd, U. Sieler, L. Smolik, F. Stephan, H. Trier

Fachbereich Physik, Universität Siegen, D-57068 Siegen, Germany[16]

M. Apollonio, L. Bosisio, R. Della Marina, G. Giannini, B. Gobbo, G. Musolino, L. Pitis
Dipartimento di Fisica, Università di Trieste e INFN Sezione di Trieste, I-34127 Trieste, Italy

H. Kim, J. Rothberg, S. Wasserbaech
Experimental Elementary Particle Physics, University of Washington, WA 98195 Seattle, U.S.A.

S.R. Armstrong, L. Bellantoni, D. Cinabro, J.S. Conway, P. Elmer, Z. Feng, D.P.S. Ferguson, Y. Gao, S. González, J. Grahl, J.L. Harton, O.J. Hayes, H. Hu, S. Jin, R.P. Johnson, J. Kile, P.A. McNamara III, J. Nielsen, W. Orejudos, Y.B. Pan, Y. Saadi, I.J. Scott, V. Sharma, A.M. Walsh, J. Walsh, J. Wear, Sau Lan Wu, X. Wu, J.M. Yamartino, G. Zobernig
Department of Physics, University of Wisconsin, Madison, WI 53706, USA[11]

[1]Also at CERN, 1211 Geneva 23, Switzerland.
[2]Supported by the US Department of Energy, grant DE-FG03-92ER40689.
[3]Also at Centro Siciliano di Fisica Nucleare e Struttura della Materia, INFN, Sezione di Catania, 95129 Catania, Italy.
[4]Also Istituto di Fisica Generale, Università di Torino, 10125 Torino, Italy.
[5]Also Istituto di Cosmo-Geofisica del C.N.R., Torino, Italy.
[6]Supported by the Commission of the European Communities, contract ERBFMBICT982894.
[7]Supported by CICYT, Spain.
[8]Supported by the National Science Foundation of China.
[9]Supported by the Danish Natural Science Research Council.
[10]Supported by the UK Particle Physics and Astronomy Research Council.
[11]Supported by the US Department of Energy, grant DE-FG0295-ER40896.
[12]Supported by Fonds zur Förderung der wissenschaftlichen Forschung, Austria.
[13]Supported by the US Department of Energy, contract DE-FG05-92ER40742.
[14]Supported by the US Department of Energy, contract DE-FC05-85ER250000.
[15]Supported by the Direction des Sciences de la Matière, C.E.A.
[16]Supported by the Bundesministerium für Bildung, Wissenschaft, Forschung und Technologie, Germany.

Contents

1 Introduction

The large electron-positron collider LEP operated at centre-of-mass energies close to the Z resonance during the years 1989 to 1995. In this paper, final results on the Z resonance parameters from decays into hadrons and charged lepton pairs are presented, based on the full data sample collected by the ALEPH detector from 1990 to 1995. These data correspond to a total integrated luminosity of approximately 160 pb^{-1}, representing more than 4.5 million selected Z decays.

The Z lineshape is studied by measuring the visible cross section at several centre-of-mass energies near to the Z mass. This "energy scan" allows the determination of the mass M_{Z} and the total width Γ_{Z} of the Z boson. The Z partial decay widths and the lepton forward-backward asymmetries are obtained from precise measurements of the cross sections and angular distributions of Z decays to fermions performed at the resonance peak, where the greatest data sample is recorded. These measurements, combined with results on other electroweak observables, provide stringent tests of the Standard Model.

Substantial analysis improvements over previous ALEPH publications and new selections designed to make optimal use of the statistical precision of the data result in a large reduction of the systematic uncertainties. These analyses are described in detail in the following. The results presented here supersede those relative to the years 1990–1992 published in Refs. [1–4].

2 The ALEPH detector

The ALEPH detector is designed to study a wide range of phenomena produced in $\mathrm{e}^+\mathrm{e}^-$ collisions both in the energy range of the Z resonance and at higher energies up to 200 GeV. Emphasis was placed on its hermeticity, on precise measurement of charged particle momenta up to the highest energy, and on good identification of the three lepton flavours. The apparatus and its performance are described in detail elsewhere [5, 6]; only a brief overview is presented here.

The tracking system consists of a silicon vertex detector, a drift chamber and a large time projection chamber, immersed in a 1.5 T magnetic field produced by a superconducting magnet. The silicon vertex detector (VDET) [7], operational from 1991, provides precise track measurements very close to the interaction point. It consists of two concentric layers of double-sided silicon microstrip detectors positioned at average radii of 6.5 cm and 11.3 cm, covering 85% and 69% of the solid angle, respectively. The spatial resolution for the $r\phi$ and z projections (transverse to and along the beam axis, respectively) is 12 μm at normal incidence. The vertex detector is surrounded by a multilayer axial-wire cylindrical drift chamber, the inner tracking chamber (ITC), which is 200 cm long and measures the $r\phi$ positions of tracks at 8 radii between 16 and 26 cm. The average resolution in the $r\phi$ coordinate is 150 μm. The time projection chamber (TPC) is the main tracking detector. It is 440 cm long and provides up to 21 three-dimensional space coordinates and 338 samples of ionisation energy loss (dE/dx) for tracks at radii between 30 and 180 cm. When at least four points are required, tracks are reconstructed down to 15° in polar angle. Azimuthal ($r\phi$) and longitudinal (z) coordinate resolutions of 170 μm of 740 μm, respectively, are obtained. Using the combined information from the TPC, ITC and VDET, a transverse momentum resolution of $\sigma(1/p_{\mathrm{t}}) = 0.6 \times 10^{-3}(\mathrm{GeV}/c)^{-1} \oplus 0.005/p_{\mathrm{t}}$ is achieved.

A particle not synchronous with the beam crossing, such as a cosmic-ray, is reconstructed in the TPC but, if it is out of time by more than $\sim 20\,\mathrm{ns}$, it will either not have any hits in the ITC, or, if the ITC hits are present, they will not be associated with the TPC track. Therefore a cut on the number of ITC hits is effective against cosmic-ray background.

The electromagnetic calorimeter (ECAL) is a lead/proportional wire chamber sampling device of 22 radiation length thickness which surrounds the TPC and is contained inside the superconducting coil. It consists of 36 modules, twelve in the barrel and twelve in each endcap, providing coverage in the angular range $|\cos\theta| < 0.98$. The ECAL is finely segmented into 74,000 projective towers, subtending on average 0.9° in both θ and ϕ at the interaction point. The towers are read out in three sections in depth ("storeys") of four, nine and nine radiation lengths. In addition, signals are available from the wire planes of each module, allowing a check of the energy measurement. The relative energy resolution is $\sigma(E)/E = 0.18/\sqrt{E}+0.009$ with E in GeV.

The return yoke of the magnetic field is a large iron structure fully instrumented to form a hadron calorimeter (HCAL) which also serves as a muon filter. The HCAL consists of 23 layers of streamer tubes 9×9 mm^2 in cross section separated by 5 cm thick iron slabs, giving a total of 7.2 interaction lengths. It is read out in 4,788 projective towers, each with a typical angular coverage of $3.7^\circ \times 3.7^\circ$, corresponding to 4×4 of the electromagnetic towers. Digital signals from each of the tubes are also read out, providing a two-dimensional projection of the shower profile. The relative energy resolution of the calorimeter is $\sigma(E)/E = 0.85/\sqrt{E}$ with E in GeV. In order to avoid the small gaps ("cracks") between modules overlapping, the whole ECAL is rotated in azimuth by two towers with respect to the HCAL.

Outside the iron structure, two double layers of streamer tubes, the muon chambers, provide two space coordinates for particles leaving the detector, thus improving the performance for muon identification. In 1990, only one such double layer was present.

Two different luminosity detectors were used during the LEP lifetime. The first one, LCAL, used from the start to September 1992, is a lead/proportional wire chamber sampling calorimeter of 24.6 radiation length thickness. The LCAL surrounds the beam pipe on both sides of the interaction region at a distance of approximately 270 cm from the interaction point, covering the polar angle region from 46 to 122 mrad. It is read out in projective towers with a typical transverse granularity of 3 cm. Up to 1991 it was used in conjunction with a small angle tracker (SATR) which was removed in 1992 to permit the installation of the second generation luminosity monitor. This second detector, a silicon-tungsten sampling electromagnetic calorimeter (SICAL) [8], was used from September 1992 for the remainder of the data taking. The SICAL consists of two homogeneous cylindrical detectors surrounding the beam pipe at roughly ± 250 cm from the interaction point. The calorimeters cover the polar angle range from 24 to 58 mrad. Twelve layers of tungsten alternate with layers of silicon pad detectors resulting in 23 radiation length thickness. Each layer is segmented into

32 sectors in azimuth, each with 16 radial pad rows 5.225 mm wide. A total of 12,288 pads are read out individually, allowing a full reconstruction of the transverse and longitudinal shower development.

3 Particle identification

The first measurements of lepton cross sections were made using a low statistics data sample accumulated during the early running at the Z peak. For these analyses the detection of leptonic events relied on the kinematic properties of the final states and made limited use of particle identification. Later, with the availability of higher statistics, the particle identification algorithms were significantly improved and more sophisticated analyses were developed for leptonic cross sections and asymmetry measurements. In this section the evolution of the particle identification algorithms from the standard ALEPH approach described in Ref. [6] to those that incorporate more sophisticated techniques is presented.

Electron identification is based on a comparison of the energy deposit in the ECAL with the momentum measured in the tracking system, the transverse and longitudinal energy profiles in the ECAL and the specific ionisation measurement in the TPC. The transverse and longitudinal profiles of the ECAL clusters are also used in a similar manner for photon identification, with the requirement that no charged track point to the cluster. Muons are identified by requiring a hit pattern characteristic of a penetrating particle in the HCAL and hits in the muon chambers.

Based on this information, different particle identification tools were developed in the course of time. The standard ALEPH identification algorithms are applied to the global description of the events using an energy-flow reconstruction algorithm which provides a list of charged and neutral reconstructed objects (electrons, muons, photons, charged or neutral hadrons), characterised by their energies and momenta. This energy-flow particle identification is used by the exclusive tau cross section measurement (Section 10.4.2) and, for muon rejection, by the exclusive electron cross section analysis (Section 10.4.3). The exclusive muon cross section measurement (Section 10.4.1) is also essentially based on the standard criteria, except that it requires a track to be identified as a muon either in the HCAL or in the muon chambers. The efficiency of this muon identification algorithm is discussed in detail in Section 10.4.1.

Although the energy-flow method is a very powerful tool for high-multiplicity final states, a more accurate approach involving a complete reconstruction and identification of each particle can be used for low-multiplicity events. The "global analysis" (Section 10.5) and the method used for the measurement of the lepton forward-backward asymmetries (Section 11) make use of charged particle identification algorithms based on likelihood estimators developed more recently in the context of tau physics [9, 10].

As an example, Table 1 gives the charged particle identification probability, evaluated from the tau Monte Carlo simulation, for an algorithm based on that of Ref. [10], but improved at low momentum. Since these probabilities are close to one, the selection efficiency dependence

Table 1: Identification and misidentification probabilities for electrons, muons, and hadrons produced in one-prong tau decays. The identification is performed for tracks with momentum above 1.3 GeV/c and outside the ECAL cracks for hadrons and electrons.

Tau decays $\rightarrow$ identified as $\downarrow$	e$\nu\nu$	$\mu\nu\nu$	h + n$\pi^0\nu$
electron	0.995	0.000	0.006
muon	0.000	0.992	0.010
hadron	0.005	0.008	0.984

with momentum is small, except at very low momenta. Muon identification is used only above 1.3 GeV/c [10] (2 GeV/c in [9]), introducing a very small bias. Electron identification is extended to lower momenta using dE/dx information.

The probability that an electron is identified as a muon or vice versa is negligible. Figure 1 shows the identification efficiencies for electrons, muons and hadrons (denoted by ε_{e}, ε_{μ} and ε_{h}, respectively) as a function of the particle momenta normalised to the beam energy, and the probability for hadrons to be misidentified as electrons or muons. These distributions are based on Monte Carlo simulations of electron, muon and tau dileptons and two-photon events. The agreement with data was checked on specific samples of hemispheres selected by identifying the opposite side and applying kinematic cuts. These samples originate at high energies from $\mathrm{e^+e^-} \rightarrow \mathrm{e^+e^-}$ and $\mathrm{e^+e^-} \rightarrow \mu^+\mu^-$ events and at low energies from two-photon interactions. This study shows that the efficiencies are reproduced at the 2 per mil level. To check the hadron contamination in the electron or muon samples, a sample of charged hadrons is obtained from $\tau \rightarrow \rho\nu$ decays selected with high purity using a clean π^0 selection. The probability for a charged hadron from this sample to be identified as an electron (muon) differs in data and Monte Carlo by 0.003 (0.002).

Neutral particles are identified as photons or π^0s in the global analysis (Section 10.5) using the algorithms developed for the measurement of hadronic tau branching ratios [11]. Fake photons are rejected from the sample of neutral electromagnetic clusters with a maximum likelihood method. Photons that convert in the detector material are reconstructed by pairing all oppositely charged tracks of a hemisphere with the requirement that at least one of them be identified as an electron. The invariant mass of the pair must be less than 30 MeV/c^2 and the minimal distance between the helices of the two tracks in the xy plane smaller than 0.5 cm. Following this, π^0s are reconstructed by pairing two photons and performing a kinematic mass-constrained fit. When the energy of the π^0 is large (typically above 10 GeV) the two photon showers may no longer be separated. In this case the two-dimensional energy distribution in the plane transverse to the photon direction is used to distinguish between π^0s and single photons. Finally, residual single photons are classified as genuine single photons (from bremsstrahlung, initial and final state radiation, $\omega \rightarrow \pi^0\gamma$ or $\eta \rightarrow \gamma\gamma$ decays), genuine photons from π^0 decays (where the second photon is lost due to the energy threshold or to ECAL cracks) and fake photons.

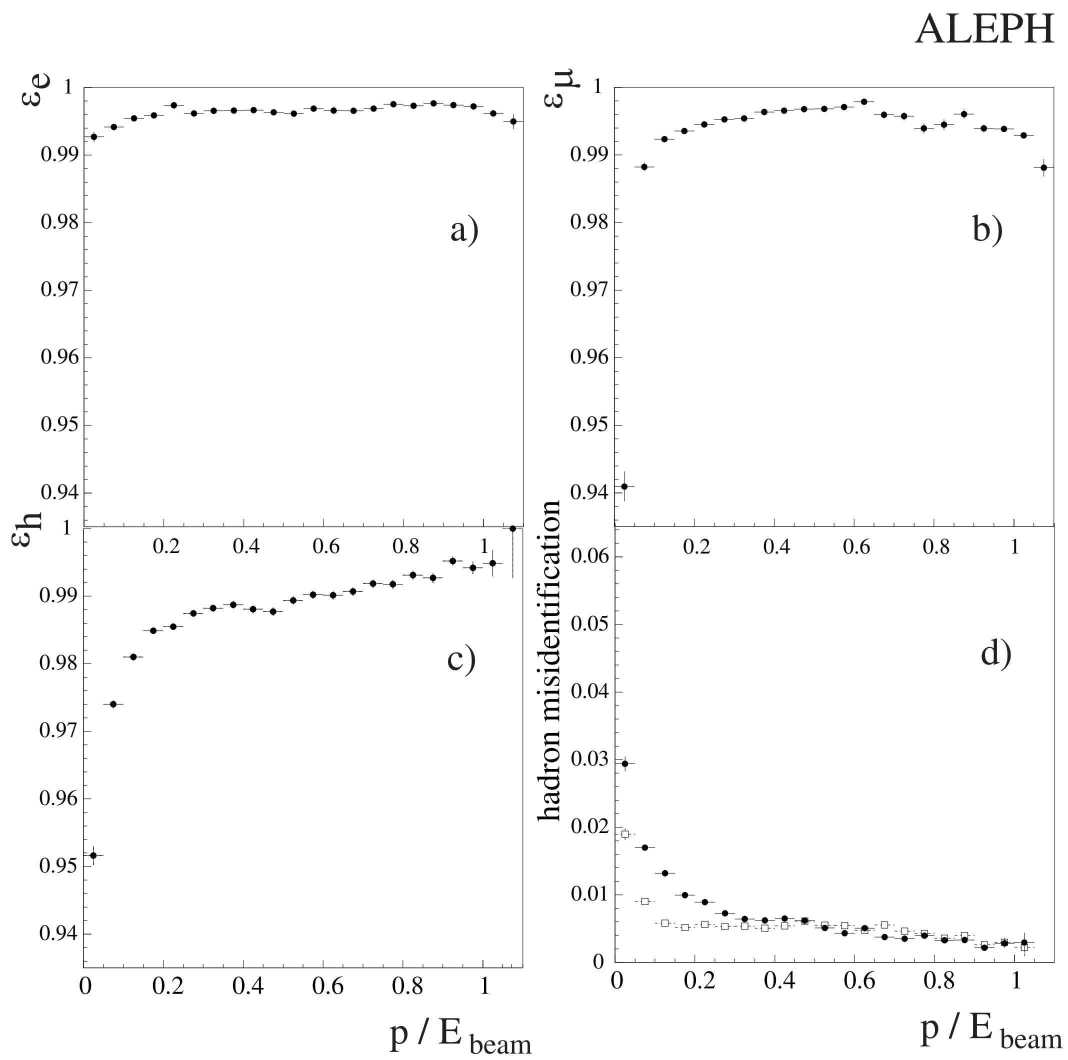

Figure 1: Identification efficiencies for electrons a), muons b) and hadrons c) as a function of the momentum to beam energy ratio. In d) the probability for a hadron to be misidentified as an electron (squares) or a muon (circles) is shown. These distributions are obtained from a Monte Carlo simulation of electron, muon and tau dileptons and two-photon events.

4 The trigger system

The detectors involved in the trigger for Z decay events are HCAL, ECAL, ITC and TPC. All except the TPC cover nearly the same solid angle, which represents approximately 98% of the full solid angle. To monitor the e^+e^- collision rate, trigger signals from the luminosity calorimeters are used, as explained in Section 7. In order to correlate the presence of particle signals in the various detector elements, the apparatus is divided into projective segments of solid angle, which closely follow the mechanical structure of the electromagnetic and hadronic calorimeters.

The trigger is performed in three stages. The first stage (Level 1) provides a fast decision on the presence of electromagnetic energy or of a coincidence between a charged track detected in the ITC and energy or a hit pattern in one of the calorimeters. The second stage (Level 2) verifies some of the Level 1 charged triggers with the TPC tracking information available 50 μs after the beam crossing. A third software stage (Level 3) is used to reject background such as beam-gas interactions and off-momentum particles hitting the vacuum chamber or collimators.

Three complementary triggers are used to select Z decays in Level 1:

- The total energy trigger is derived from the ECAL by separately summing the signals from the wire planes of the barrel and of the two endcap modules. An energy above 6.6 GeV in the barrel, 3.8 GeV in either endcap, or 1.5 GeV in each endcap is typically required by this trigger.
- The electromagnetic track trigger requires a track candidate in the ITC in coincidence with an energy deposit in the ECAL module to which the track is pointing. A track candidate is defined in the rϕ plane by requiring hits in at least five out of the eight ITC layers. The associated ECAL wire energy must typically exceed 1 GeV.
- The muon track trigger is based on an ITC-HCAL coincidence, requiring a track candidate in the ITC in coincidence with four out of twelve double planes of HCAL tubes in the same azimuthal region.

These main triggers do not require validation at Level 2. In addition, two subsidiary triggers are used to calculate the trigger efficiencies.

- An electromagnetic track trigger is defined based on a lower ECAL wire energy threshold ($\sim$200 MeV) but with a more restrictive requirement on the ITC track, which must be defined in space, rather than in rϕ only. This auxiliary trigger has a higher background acceptance than the main triggers. Therefore, it was either down-scaled or tightened by requiring the presence of two track candidates in the drift chamber, validated at Level 2.
- A back-to-back track trigger is constructed by requiring two track segments back-to-back in the ITC. The presence of two such charged particle trajectories must be confirmed by a Level 2 decision.

The trigger rate was typically 4–5 Hz, where Bhabha events in the luminosity calorimeter contribute 2–3 Hz, Z events (at the peak) and two-photon events contribute about 0.5 Hz each, and the remainder is accounted for by cosmic rays, noise and beam related background. The trigger efficiency depends on the characteristics of the selected event sample and is determined in each case from the data using redundant trigger information.

The basic triggers for hadronic events are the total ECAL energy and muon track triggers. These two triggers are independent and each is efficient for more than 99.7% of the hadronic Z decays. Their combined efficiency exceeds 99.999%, with an uncertainty of less than 0.001%, determined by comparing the rates for one or both of the triggers.

For the leptonic final states the main triggers are the total energy, the electromagnetic and muon track triggers. The efficiency of the last two triggers is measured by taking advantage of the availability of the azimuthal trigger information. Since the two leptons or their decay products trigger independently, the single lepton trigger efficiency is measured from the observed number of events in which one or both leptons trigger and is used to calculate the overall efficiency for lepton pairs. Possible correlations due to insensitive regions between the calorimeter modules are found to have a negligible impact on the efficiency. In fact, the bending of the magnetic field prevents back-to-back high momentum tracks from both pointing to insensitive regions between modules. In addition, the low threshold electromagnetic track and back-to-back track triggers are used as auxiliary triggers for muons, and the total energy and back-to-back track triggers for electrons and taus. These studies indicate that the trigger inefficiency for all lepton channels (within the angular acceptance defined in Section 9.2) is smaller than 3×10^{-5}.

Since all charged triggers rely on the ITC, the ECAL total energy trigger, which is independent of the ITC trigger signals, is also used to evaluate a potential bias to the trigger efficiency introduced by the ITC. This study makes use of Bhabha events, which in the ITC behave like $\mu^+\mu^-$ or $\tau^+\tau^-$, but always fire the ECAL total energy trigger. The resulting systematic uncertainty related to the ITC is found to be of the order of few 10^{-5} and is neglected.

As a result of these studies, the trigger inefficiency and the corresponding systematic uncertainty are neglected in the evaluation of the selection efficiency for the hadronic and leptonic channels.

5 LEP energy calibration

Precise knowledge of the energy of the colliding particles at the interaction point is essential for the determination of the Z resonance parameters. An accurate determination of the Z mass and width was achieved by performing energy scans of the Z resonance, which required changing the beam energy around the peak from fill to fill, where one fill typically lasted about 10 hours and delivered an integrated luminosity of several hundred nb^{-1}. In 1993 and 1995, data were recorded at three different energy points, near the maximum of the resonance and about 2 GeV below and above, referred to as "peak", "peak−2" and "peak+2", respectively; data taking in 1992 and 1994 was exclusively at the peak and in 1990 and 1991 data were collected at several different energy points with centre-of-mass energies in the range $|\sqrt{s} - M_{\mathrm{Z}}| < 3\,\mathrm{GeV}$. Details are given in Table 4 of Section 6. In 1995 LEP was operated in "bunch train" mode [12], i.e., with four equally spaced trains of up to four bunches separated by ∼250 ns. The electrostatic separators used to prevent parasitic collisions outside of the experimental areas caused an energy dispersion (i.e., an energy ordering of particles in a bunch) which had to be corrected for.

The uncertainty in the absolute energy scale directly affects the mass, whereas the width is only affected by the error on the difference in energy between energy points. The errors induced on the Z mass and width depend mainly on the high statistics points at peak−2 and peak+2. The effects of the beam energy calibration on the peak cross section and on the forward-backward asymmetries are smaller (see discussion in Section 13).

The determination of the average energy of the beams in LEP [13, 14] is based on the technique of resonant depolarisation [15], characterised by a very high precision (±0.2 MeV) at the time of the measurement. However, these measurements were only performed outside normal data taking, typically at the end of fills. The extrapolation of these precise values of the beam energy at a particular time to the full set of data thus requires corrections for the time-dependence of the magnetic field in the bending dipole magnets and for the changes in energy caused by deformations of the LEP ring. These corrections were performed with a model based on direct measurements of the magnetic dipole fields by nuclear magnetic resonance probes and on tide experiments performed in 1992 and 1993. The agreement of the model with reality is checked by comparison with the precise depolarisation measurements [14].

The energy at the interaction point is not equal to the average beam energy discussed so far. The acceleration of the particles in the radio frequency (RF) cavities as well as dispersion effects can lead to substantial corrections on the mean beam energy. In Aleph, such corrections were small. The RF correction was negligible in 1993 and only ∼1.0 MeV in 1995. The dispersion correction was shown to be negligible in 1993 and amounted to ∼0.5 MeV in 1995.

The mean beam energy was determined every 15 minutes and a luminosity-weighted average was computed for each energy point and used as input to the data analysis. For each of the energy points the mean energy distribution has a typical spread of 10 MeV, including both fill-to-fill variations and variations inside the fill. The errors on these mean energies are summarised in Table 2 for the data sets recorded between 1993 and 1995. These are uncorrelated with the energy errors for the earlier data, 1990–1992, which may be found in Ref. [13]. The errors at the four interaction points are slightly different due to varying RF configurations and beam dispersion. In practice, however, the average matrix common to all LEP experiments was found to be equivalent to that of Aleph, since no change in results is visible within the quoted precision. Data taken in 1993–1995 at the peak during periods prior to the commissioning of the precision energy scans have larger energy uncertainties; these are also given at the bottom of Table 2.

The energy of a given particle in a bunch oscillates around the mean energy with a frequency which is given by the synchrotron tune of the accelerator multiplied by the revolution frequency. The colliding particles are therefore typically not exactly at the mean energy described above. The energy spread δE is determined from the longitudinal size of the bunches, measured from the longitudinal size of the luminous region at the interaction point. The values of the centre-of-mass energy spread determined for Aleph are shown in Table 3. This energy spread, which includes the additional effect due to variations in average beam energies described above, is taken into account when correcting the cross section measured at one energy point to a specific value in centre-of-mass energy.

Table 2: The covariance matrix (in MeV^2) of the errors on the centre-of-mass energies at the ALEPH interaction point for the scan points in 1993–1995.

	1993 peak−2	1993 peak	1993 peak+2	1994 peak	1995 peak−2	1995 peak	1995 peak+2
1993 peak−2	3.42^2	2.75^2	2.59^2	2.25^2	1.27^2	1.17^2	1.19^2
1993 peak		6.69^2	2.63^2	2.38^2	1.12^2	1.18^2	1.14^2
1993 peak+2			2.95^2	2.16^2	1.21^2	1.24^2	1.31^2
1994 peak				3.66^2	1.22^2	1.28^2	1.22^2
1995 peak−2					1.82^2	1.23^2	1.21^2
1995 peak						5.41^2	1.33^2
1995 peak+2							1.73^2
1993 peak-pre-scan	18^2, uncorrelated						
1994 peak-no-sical	10^2, 30% correlated with 1994 peak						
1995 peak-pre-scan	10^2, uncorrelated						

Table 3: Centre-of-mass energy spread. The energy spread in the 1990 and 1991 running periods, consisting of seven energy points each, increases with energy by 1 MeV per GeV. The additional energy spread of approximately 10 MeV from variations in mean beam energy of data taken at an energy point is also included.

	energy spread (MeV)			error (MeV)
	peak−2	peak	peak+2	
1990	48.0	50.0	52.0	±3
1991	44.0	46.0	48.0	±3
1992		51.0		±3
1993	56.4	57.0	57.1	±1.1
1994		56.5		±1.1
1995	56.6	57.2	57.7	±1.3

Spurious longitudinal beam polarisation of the e^+e^- system is estimated in Ref. [16] to be zero, with upper limits of 0.06% at the Z peak and 0.2% at the peak-2 and peak+2 points, leading to upper limits on the additional systematic error on the Z mass and width of 0.2 MeV.

6 Data and Monte Carlo samples

The efficiency of data taking with ALEPH with respect to the integrated luminosities delivered by LEP was 83.4% averaged over all years, reaching 90% in 1995. The inefficiency was equally distributed among three main sources: *i)* operational, mainly due to the detector not being at full voltage when stable beam conditions were reached at the beginning of fill or to high-voltage trips, *ii)* inefficiency associated with the data acquisition dead time, and *iii)* to data acquisition or hardware faults.

6.1 The data sample

The data are divided into 27 different energy points according to centre-of-mass energy and year. Throughout the rest of this paper, the various parts of the LEP data will be referred to using the conventional names specified in Table 4. In 1992, due to the upgrade of the luminosity calorimeter, two different configurations were present for which the data were analysed separately, the 1992 "LCAL" and "SICAL" periods. In 1993 and 1995, the data taking periods were divided into two parts. In the "scan" period, data were collected at three energy points in turn, with frequent LEP energy calibration measurements distributed throughout the period, as discussed in Section 5. Before the start of the scan, data were collected at the peak energy. Such periods for which the LEP energy uncertainties are significantly larger than those of the scan points are referred to as "peak-pre-scan" data. A less accurate SICAL luminosity is available for the periods "peak-no-sical" of 1994 and "peak-pre-scan" of 1995 due to bad LEP background conditions in 1994 and a variable bunch train configuration in 1995 [12]. These data were used only for the measurements of the ratio of the hadronic and leptonic Z decay widths and for the forward-backward lepton asymmetries.

6.2 Monte Carlo samples

To design the selection algorithms and for acceptance corrections, several large Monte Carlo event samples were generated and processed through the complete chain of detector simulation and event reconstruction. The detector simulation takes into account variations in the response of the apparatus from one year to another.

The production of hadronic events incorporates several components. The initial quark-antiquark pair and initial state photon radiation were generated with the program DYMU [17] and then treated by the Lund Parton Shower Model (JETSET version 7.3) [18]. Approximately one million events were generated at the peak and about 300,000 off-peak. In addition to the Lund Parton Shower Model, alternative Monte Carlo models based on different hadronisation mechanisms were also used to generate hadronic events. Two samples of $\sim$200,000 events each were generated with the HERWIG (version 5.8) [19] and ARIADNE (version 4.08) [20] Monte Carlo programs.

Wide-angle Bhabha events were produced using the program UNIBAB [21], an event generator which includes leading log contributions to the electromagnetic radiative corrections to all orders with soft photon exponentiation, as well as contributions from multiple emission of hard collinear photons. UNIBAB includes $O(\alpha)$ electroweak corrections but has no provision for the interference between initial and final state radiation. Approximately 550,000 e^+e^- events were generated at the different centre-of-mass energies in a restricted polar angle region to avoid divergences due to the t channel exchange.

The event generator KORALZ 4.0 [22] was used to produce $\mu^+\mu^-$ and $\tau^+\tau^-$ events. Approximately 900,000 $\mu^+\mu^-$ and 1.9 million $\tau^+\tau^-$ were generated at the different nominal centre-of-mass energies, in proportion to the data collected at each point. KORALZ includes initial and final state bremsstrahlung corrections up to order $O(\alpha^2)$ with

Table 4: Overview of the data sample used. Shown are the luminosity-weighted average energies and the integrated luminosities recorded by ALEPH at the various energy points during the years 1990 to 1995. For the 1994 "peak-no-SICAL" and 1995 "peak-pre-scan" datasets indicative values for the integrated luminosity were estimated using the numbers of selected hadronic events.

Year	"Name"	$\sqrt{s}$ (GeV)	$\mathcal{L}$ (nb^{-1})	$\Delta\mathcal{L}/\mathcal{L}$ stat. error (per mil)
1990	peak−3	88.223	482.0	8.6
	peak−2	89.217	520.1	8.4
	peak−1	90.217	447.2	9.1
	peak	91.215	3624.0	3.2
	peak+1	92.207	554.6	8.4
	peak+2	93.209	597.2	8.2
	peak+3	94.202	641.8	8.0
1991	peak-pre-scan	91.238	4609.2	2.9
	peak−3	88.464	668.4	7.3
	peak−2	89.455	796.8	6.7
	peak−1	90.212	753.2	7.0
	peak	91.207	2937.3	3.6
	peak+1	91.952	693.2	7.5
	peak+2	92.952	677.3	7.6
	peak+3	93.701	796.6	7.1
1992	LCAL	91.276	12297.5	1.8
	SICAL	91.270	8749.0	1.2
1993	peak-pre-scan	91.303	5313.6	1.5
	peak−2	89.432	8069.6	1.2
	peak	91.187	9135.4	1.1
	peak+2	93.015	8690.3	1.2
1994	peak-no-sical	91.219	∼12439.5	
	peak	91.197	42695.2	0.5
1995	peak-pre-scan	91.293	∼12396.0	
	peak−2	89.440	8121.4	2.0
	peak	91.282	4872.5	2.7
	peak+2	92.968	9372.5	2.0

exclusive exponentiation and $O(\alpha)$ electroweak corrections. QED initial-final bremsstrahlung interference in the presence of multiple QED hard bremsstrahlung is however not included. A correction for this effect was evaluated with the Monte Carlo generator KK [23], as described in Section 9.2.

The presence of initial state radiation (ISR) causes the invariant mass of the final state particles including any final state radiation (FSR) to be reduced from $\sqrt{s}$ to $\sqrt{s'}$, where $\sqrt{s'}$ is limited to the range $2m_\mathrm{f} < \sqrt{s'} < \sqrt{s}$. For the generation of $\mathrm{e^+e^-} \to \mathrm{f\bar{f}}$, the minimum invariant mass of the $\mathrm{f\bar{f}}$ system was set to twice the tau mass for lepton pairs, while for hadrons it was set to $0.1\sqrt{s}$. These values, which are applied to the Monte Carlo event generation to determine detector acceptances, coincide with the integration bounds for the ISR used in the fitting function described in Section 13.

Two-photon interaction processes, referred to as $\gamma\gamma$ events throughout this paper, were simulated with the PHOT02 generator [24]. This program allows the generation of events of the type $e^+e^- \rightarrow e^+e^-X$, where X can be either a pair of leptons, in which case the generation is based on an exact QED calculation, or a multihadronic state dominated by the Vector Dominance Model (VDM). For the VDM simulation, the cross section is assumed to be proportional to $A + B/W$, where W is the invariant mass of the hadronic system and A and B are two constants ($A \simeq 100\,\mathrm{nb}$, $B \simeq 1000\,\mathrm{nb\,GeV}/c^2$) [25].

Four-fermion processes of the type $e^+e^- \rightarrow \ell^+\ell^-f\bar{f}$ where ℓ is a lepton and f any fermion were simulated using the four-fermion generator FERMISV [26]; details on the impact of such processes on the lepton cross section measurements are discussed in Section 10.3.

The small-angle Bhabha Monte Carlo event samples used for the luminosity determination are described in Section 7.5.

7 The Luminosity determination

Bhabha scattering $e^+e^- \rightarrow e^+e^-$ is used as the reference reaction to provide the absolute normalisation of other processes. The rate of such events detected in specially designed monitors, LCAL and SICAL, is used to measure the luminosity of the colliding beams, found by dividing the number of selected events by the Bhabha cross section integrated over the acceptance. The effect of the electroweak process $Z \rightarrow e^+e^-$ on the reference cross section is limited by restricting the acceptance to small angles, where the Bhabha rates, dominated by t channel photon exchange, are therefore largely described by QED. The large cross section at small angles gives the further advantage of reducing the statistical uncertainty of the reference measurement. Given the high statistics accumulated each year, leading to small statistical errors on the hadronic cross section measurements, the goal was to achieve a statistical and systematic precision below one per mil.

7.1 Measurement principle

At small angles the lowest order QED Bhabha cross section is

$$\frac{d\sigma}{d\Omega} = \frac{16\,(\hbar c\alpha)^2}{s}\left(\frac{1}{\theta^4}\right) , \tag{1}$$

which integrated over the acceptance gives

$$\sigma^{\mathrm{acc}} = \frac{1040 \text{ nb GeV}^2}{s}\left(\frac{1}{\theta^2_{\mathrm{min}}} - \frac{1}{\theta^2_{\mathrm{max}}}\right) . \tag{2}$$

The scattering angles θ of the electron and of the positron are estimated from their radial position R measured by calorimeters at a defined z position close to the average maximum of the shower. Since the calorimeters are placed at about 2500 mm from the interaction point, one has that $\theta \simeq R/z$. Once the background and detection efficiencies are under control, the limiting source of systematic uncertainty on the measurement is given by the error on the acceptance at the lower θ bound:

$$\frac{\delta\sigma^{\rm acc}}{\sigma^{\rm acc}} \simeq \frac{2\delta\theta_{\rm min}}{\theta_{\rm min}} = 2\left(\frac{\delta R_{\rm min}}{R_{\rm min}} \oplus \frac{\delta z}{z}\right). \tag{3}$$

In order to reach the required precision of one per mil, the lower radial boundary transverse to the beam line has to be known to a precision of $\sim 30\,\mu$m and the z position with respect to the interaction point to a precision of $\sim$ 1 mm. At LEP the size of the luminous region is small ($\sigma_x \simeq 0.14$ mm, $\sigma_y \simeq 0.003$ mm, and $\sigma_z \simeq 7$ mm) but the relative position of the calorimeter with respect to the beam is difficult to measure and to monitor to the required precision. In order to reduce the sensitivity of the luminosity measurement to possible relative displacements of the beam-to-detector system (along the beam line and transverse to it), fiducial cuts define a restricted geometrical acceptance (tight) in one calorimeter and a less restrictive one (loose) in the other, as proposed in Ref. [27]. The assignment of loose and tight is changed from one calorimeter to the other alternatively on an event-by-event basis. This procedure cancels the linear dependence of the cross section upon displacements of the beam crossing position. Only two quantities therefore define the acceptance: the lower radius of the tight selection, measured in the calorimeter reference frame, and the distance along the beam line of the two calorimeters.

The overall precision of the luminosity measurement is then determined from the radial mechanical precision of the calorimeters, its stability in time and the ability to select events close to the boundary of the tight acceptance with minimal bias. The latter is achieved by defining the acceptance boundary along the edge of adjacent detecting elements and selecting the events using the sign of the energy asymmetry $A_{\rm r}$

$$A_{\rm r} = \frac{E_{\rm in} - E_{\rm out}}{E_{\rm in} + E_{\rm out}}, \tag{4}$$

where $E_{\rm in}$ is the energy inside a radial pad-width within the fiducial region and $E_{\rm out}$ is the energy in the adjacent pad-width outside the region.

7.2 The trigger

Triggers used in the luminosity determination must be highly efficient for Bhabha scattering events and redundant to allow independent checks of the trigger efficiency. Furthermore, as the principal source of background to Bhabha scattering at LEP is the accidental coincidence of off-momentum beam particles, a dedicated trigger is set up to allow a precise determination of this contamination.

Three triggers, based on the total energy deposition in the calorimeters, are used:

- A luminosity trigger, which requires a large energy deposit in one of the two calorimeters together with a less restrictive energy requirement in the other. This trigger is called

$(A_{\mathrm{low}} \cdot B_{\mathrm{high}}) + (A_{\mathrm{high}} \cdot B_{\mathrm{low}})$. Typically, the low and high thresholds were 10 (12) GeV and 22 (24) GeV, respectively, for LCAL(SICAL).

- A very high threshold single-arm trigger, which requires energy depositions of at least 35(39) GeV on either side. This is used to determine the efficiency of the luminosity trigger. It is down-scaled to give a small contribution to the overall ALEPH trigger rate.
- A very low threshold down-scaled single-arm trigger, which requires energy depositions of at least 15(9) GeV on either side. This is also down-scaled and is used to estimate the beam related background rate and shape.

The very high threshold single-arm events are used to monitor the efficiency of the luminosity trigger as a function of the energy detected on the opposite side. The overall trigger efficiency is measured to be 100% with a precision better than 0.01%.

7.3 Luminosity analysis

Despite the different characteristics of LCAL and SICAL, a consistent event selection has been applied to the luminosity triggers. A detailed discussion of the SICAL and LCAL luminosity measurements for the data taken from 1990 to 1992 is reported in Refs. [4] and [28].

- Energy cuts: The event selection is based on energy clusters reconstructed in the calorimeters on each side. As Bhabha events generally have radiated photons which may or may not be distinguishable from the "primary" energy cluster, no upper limit on the number of reconstructed clusters is imposed. The one on each side with the highest energy is chosen to define the barycentre position. A typical picture of the energy correlation between the two sides is given in Fig. 2. The energy deposited on each side is required to be larger than 44% of the beam energy while the sum of the two energies must be larger than 60% of the centre-of-mass energy. This set of cuts is used up to and including 1993. The cut on the energy sum is increased in 1994 due to higher contamination from beam-related background. In 1995, bunch train operation [12] required a higher value as the SICAL electronics is not adapted to operation with bunch trains with inter-bunch spacing of a few hundred nanoseconds. Figure 3 shows the evolution of the total energy cut with the year of data taking.
- Radial fiducial cuts: Radial cuts define the Bhabha geometrical acceptance. For the LCAL selection, the tight fiducial region follows the boundaries of the active area, excluding one tower line along the inner edges of the calorimeters and a region at large angles which lies in the shadow of the material from the central detector. The radial energy asymmetry is constructed using the energy measured in nearby towers.

  For the SICAL selection, the tight fiducial region is defined as the radial boundary between adjacent pads situated at a radius of 7.67 cm. In the selection the radial energy asymmetry is constructed using the energy summed over two layers in depth at 6 and 8 radiation lengths. Showers near the boundary of the tight fiducial region are fully contained in the calorimeter.

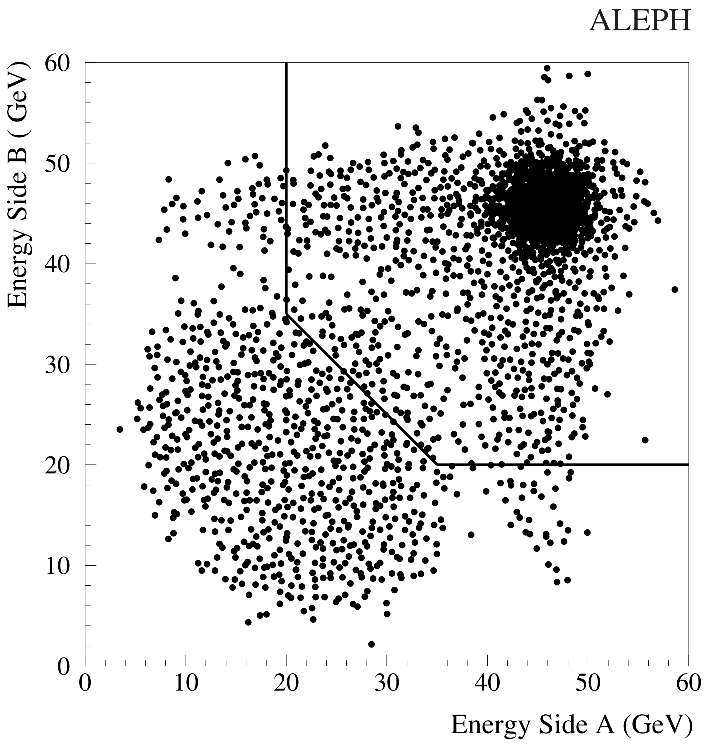

Figure 2: SICAL highest reconstructed cluster energy on side A versus highest reconstructed cluster energy on side B for clusters satisfying radial and azimuthal requirements. The entries around 20 GeV originate from accidental coincidences of off-momentum beam particles. More than 99.9% of the Bhabha events satisfy the energy cut requirements.

- Acoplanarity cut: Bhabha events are essentially coplanar, except in the presence of radiated photons. An acoplanarity cut based upon the two clusters' azimuthal difference, $170° \leq \Delta\phi \leq 190°$ (LCAL), $150° \leq \Delta\phi \leq 210°$ (SICAL), is used to further remove the remaining off-momentum beam background, without severely cutting away the radiative Bhabha events.

The reference cross sections at the peak in the fiducial acceptance for LCAL and SICAL are $\sim$25 nb and $\sim$84 nb, respectively. Their precise values are evaluated each year according to the beam energy and the measured geometrical position of the detectors.

The values of the measured integrated luminosity and statistical uncertainty for each energy are reported in Table 4. In 1995, due to the bunch train operation mode, the trigger was sampling in turn each of the bunches of the train, resulting in a larger statistical error.

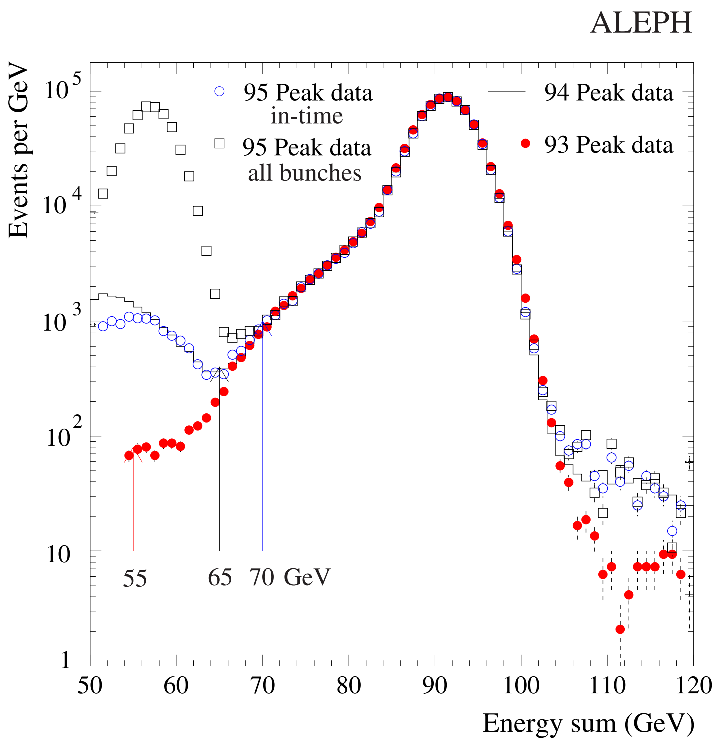

Figure 3: SICAL energy sum distribution for clusters satisfying radial and azimuthal requirements. The different levels of beam-related background and the bunch train operation in 1995 necessitated the evolution of the cut on the energy sum as indicated by the arrows.

7.4 Systematic uncertainties and correlations

The systematic uncertainty from trigger efficiency arises from the statistical significance of the single arm trigger sample used to measure it (see Section 7.2).

The background to the luminosity selection originates almost entirely from two sources:

- accidental coincidences of off-momentum beam particles; these are evaluated using the single arm triggers;
- QED production of two or more hard photons that is indistinguishable from a Bhabha scattering in the calorimeters; the evaluation of this process leads to a correction of 0.016% that is applied to the accepted Bhabha cross section.

The largest systematic uncertainty results from the definition of the geometrical acceptance of the tight selection. It has three components:

- The internal mechanical precision of the calorimeter. Survey of the LCAL cathode pad positions and repeated measurements of reference marks are consistent with an average error of 120 μm. Precise measurements of the SICAL support plates under operating temperature performed at the end of 1992 allow an accurate determination of the thermal distortion and this resulted in a reduction of the total effective radial uncertainty from 18 μm in 1992 to to 9 μm in 1993.

- The external alignment of the two calorimeters. The dominant term is their relative distance along the beam line, that is known with a precision of about 500 μm.
- The precision on the fiducial cut. This includes two sources of uncertainty. The first arises from the knowledge of the pad-to-pad energy calibration, that is known to better than 0.7%. The second originates from the precision of the electromagnetic shower description in the simulation. Because of the pad curvature, the energy asymmetry is not zero at the pad boundary. This offset is about 20 μm and is stable within 7 μm for large variations of the simulation parameters.

Reconstruction efficiency and possible event migration from overlays of Bhabha events with off-momentum particles have been carefully studied and found to have a negligible effect. The systematic uncertainty induced by the cut on the energy sum increases with the value of

Table 5: Summary of luminosity measurement relative systematic uncertainties in units of 10^{-5}. The theoretical errors marked with † corresponds to BHLUMI (version 2.01) [29] used for the 1991 and 1992 cross section calculations while the 1990 cross section was evaluated with BABAMC. The improved BHLUMI (version 4.04) [30, 31] was used for later years.

Source of relative uncertainty	$\Delta\mathcal{L}/\mathcal{L}$ (10^{-5})						
	LCAL			SICAL			
	1990	1991	1992	1992	1993	1994	1995
Trigger efficiency	1	1	1	1	0.2	0.6	3
Background estimation:							
- Off-momentum e^+ or e^-	4	4	4	18	3	0.7	0.9
- Physics sources ($e\gamma$, $\gamma\gamma$)	20	20	20	10	10	10	10
Absolute radial fiducial boundary:							
- Mechanical precision	210	210	210	58	29	29	29
- External alignment	120	70	70	49	46	47	46
- Fiducial cut precision	247	247	247	50	30	34	34
Energy cuts	234	100	100	15	4	15	38
Acoplanarity cut	100	30	30	5	5	5	5
Bunch train operation							1.2
SUBTOTAL	430	348	348	95	63	69	76
Simulation statistics	190	140	140	120	24	24	26
TOTAL experimental error	470	375	375	153	67	73	80
Theoretical error	320	210†	210†	160†	61	61	61
TOTAL error	570	430	430	221	91	95	101

Table 6: Summary of luminosity measurement correlated relative systematic uncertainties for two sets of typical years (1991–1992) for LCAL and (1993–1995) for SICAL in units of 10^{-5}.

Source of relative uncertainty	Correlated syst. uncertainties LCAL 1991–1992	SICAL 1993–1995
	$\Delta\mathcal{L}/\mathcal{L}$ (10^{-5})	
Background estimation	20	10
Absolute radial fiducial boundary:		
- Mechanical precision	210	27
- External alignment	35	15
- Fiducial cut precision	125	30
Energy cuts	100	4
Acoplanarity cut	30	5
SUBTOTAL	269	44
TOTAL correlated experimental error	269	44
Theoretical error	210	61
TOTAL Correlated error	341	75

the cut due to the steep dependence of the measured cross section on this variable (Fig. 3). The energy sum requirement had to be increased in 1994 due to the larger contamination induced by beam-related background and in 1995 due to the bunch train operation mode, resulting in a significant contribution to the overall systematic uncertainty.

A summary of the absolute luminosity systematic errors is presented in Table 5 for LCAL luminosity measurements from 1990 to 1992 and SICAL luminosity measurements from 1992 to 1995. They are expressed as relative errors. Typical correlated systematic errors are given in Table 6 for two years (1991–1992 for LCAL, 1993–1995 for SICAL). Particular care was given to the evaluation of correlated errors between energy points within the same year. Table 7 gives the correlation coefficients $\sigma^2_{\mathrm{corr}}/(\sigma_{\mathrm{year1}}\sigma_{\mathrm{year2}})$ between luminosity errors for all the years.

7.5 Theoretical uncertainty

Two different Bhabha generators are used in the luminosity analyses: BABAMC [32] in 1990 and two successive versions of BHLUMI for the later years. BHLUMI version 2.01 [29] is used for the analysis of the data up to 1992, with a 0.210% theoretical uncertainty in an LCAL-like acceptance and a 0.160% theoretical uncertainty in a SICAL-like acceptance. BHLUMI version 4.04 [30, 31] is used in later years, with a 0.061% error in a SICAL-like acceptance. Version 4.04 of BHLUMI allows an improved calculation of the contribution of the Z resonance to the small angle Bhabha scattering process and includes second-order terms in the leading logarithmic approximation for the multi-photon YFS [33] exponentiation. The Z contribution implementation was cross-checked against the BABAMC calculations performed for the analysis of the four energy points of the 1993 scan [34] and found to be in good agreement. Table 8 summarises the total theoretical uncertainty for the LCAL- and SICAL-like

Table 7: Summary of correlation coefficients between the luminosity systematic errors in the different run periods. Only nonzero terms are quoted. The correlation between LCAL and SICAL is entirely due to the use of the same generator BHLUMI version 2.01.

	LCAL				SICAL		
Year	1990	1991	1992 LCAL	1992 SICAL	1993	1994	1995
1990	1.	0.376	0.376	0.202			
1991		1.	0.629	0.269			
1992 LCAL			1.	0.269			
1992 SICAL				1.	0.280	0.268	0.252
1993					1.	0.651	0.612
1994						1.	0.586
1995							1.

Table 8: Summary of the total theoretical relative uncertainty (in %) for a generic calorimetric detector and an angular range within 3°–6° (LCAL-like) and 1°–3° (SICAL-like) at LEP. Here L is defined as $L = \log(s/m_{\mathrm{e}}^2)$.

BHLUMI version	2.01		4.04
	LCAL	SICAL	SICAL
Missing photonic $\mathcal{O}(\alpha^2 L)$	0.15	0.15	0.027
Missing photonic $\mathcal{O}(\alpha^3 L^3)$	0.03	0.008	0.015
Vacuum polarisation	0.08	0.05	0.04
Light pairs	0.08	0.04	0.03
Z exchange	0.12	0.03	0.015
TOTAL (quadratic sum)	0.21	0.16	0.061

acceptances at LEP.

8 Measurement of the hadronic cross section

Two independent methods were developed to select events from hadronic Z decays. One selection is based on charged-track properties, the second on calorimetric energy deposits. Their combination leads to a reduced systematic error which matches the statistical uncertainty of $\sim 0.05\%$ on the hadronic cross section. Both methods have an efficiency close to 100% and the two selected data samples overlap to the extent of 96%.

The hadronic cross section is defined within the phase space $\sqrt{s'/s} > 0.10$. The rate of events generated with $\sqrt{s'/s} < 0.10$ and accepted by the selection is found to be negligible ($\mathcal{O}(10^{-6})$).

8.1 Selection based on charged tracks

The hadronic selection based on charged tracks requires at least five well measured tracks in the TPC originating from the interaction region with a charged-track energy sum (assuming pion masses) E_{ch} greater than 10% of the centre-of-mass energy. The tracks must have a polar angle $|\cos\theta| < 0.95$, which ensures that at least six TPC pad rows are crossed, and at least four reconstructed coordinates. They are required to originate from within a cylinder of 2 cm radius and 20 cm length centred at the interaction point and parallel to the beam axis. The distribution of signal and background processes before selection is illustrated in Fig. 4, which shows that $q\overline{q}$ events are well isolated from background processes. Lepton pairs are removed by the cut on track multiplicity, whereas two-photon interactions are rejected by the charged-track energy sum requirement.

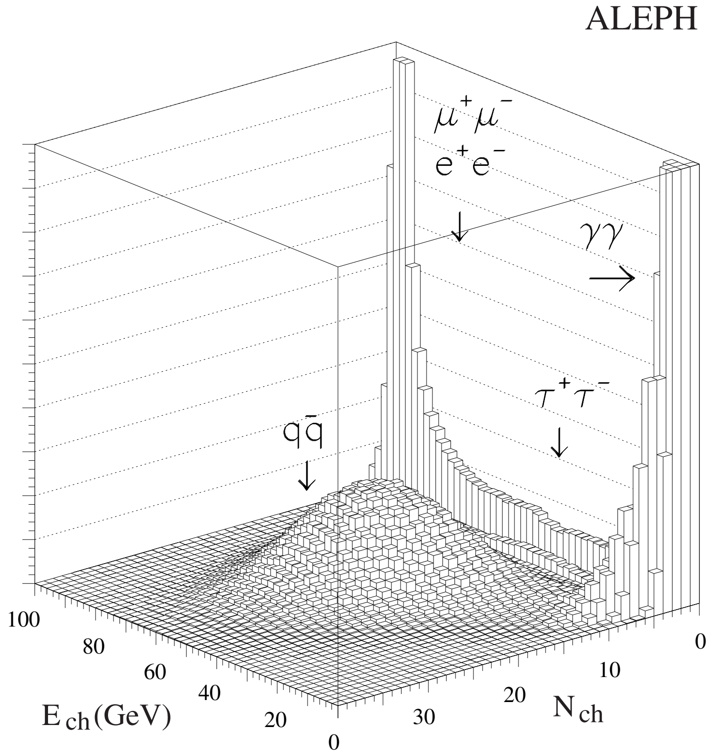

Figure 4: Distribution of charged multiplicity N_{ch} versus charged-track energy E_{ch} for events passing the Z triggers.

More than 85% of the rejected hadronic Z events are discarded by both the charged-track energy sum and the multiplicity cuts. The selection yields an overall efficiency of 97.48±0.02%

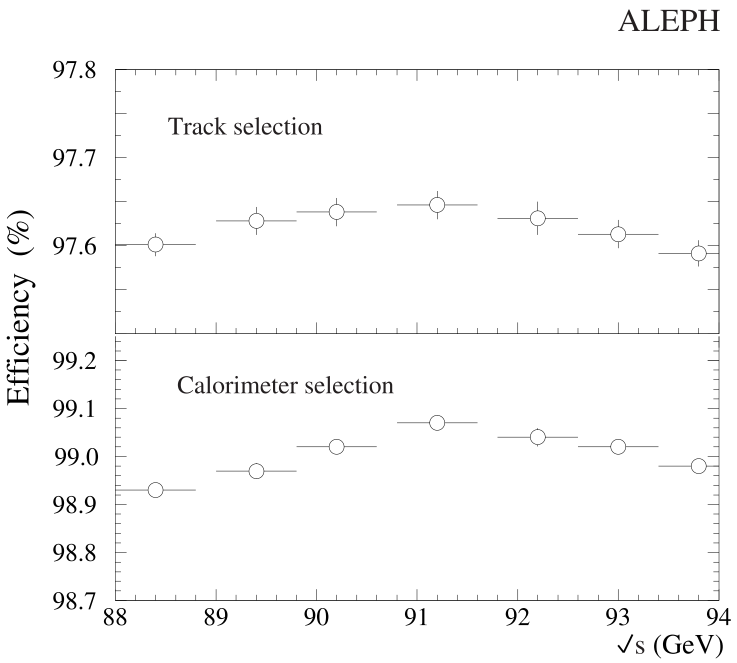

Figure 5: Efficiency as a function of centre-of-mass energy for both selections.

at peak energy, the losses originating mainly from events at low polar angle.

The dependence of the efficiency upon $\sqrt{s}$ was studied using a fully simulated Monte Carlo sample at the peak energy, weighted with off-peak Monte Carlo events generated at kinematic level only. This weighting procedure was checked with fully simulated Monte Carlo samples at peak+2 and peak−2. The resulting efficiencies, shown in Fig. 5, decrease slightly (by less than 0.1%) for centre-of-mass energies away from the Z peak. This is a result of ISR because events of the type $e^+e^- \rightarrow f\bar{f}\gamma$ with a small invariant mass of the $f\bar{f}$ system have a lower detection efficiency. Since this process is non-resonant, its relative contribution is larger away from the Z peak, and the efficiency is correspondingly reduced.

Background from beam-gas interactions is estimated from the number of events in which the vertex position along the beam is outside the 20 cm cylinder. It is found to be negligible.

The background originating from dilepton events is estimated from Monte Carlo. Both contaminations from electrons and muons are found to be negligible, whereas the background arising from $\tau^+\tau^-$ events is estimated to be 0.32%. Its uncertainty gives a 0.03% contribution to the systematic error.

The background from the two-photon process $e^+e^- \rightarrow e^+e^- +$ hadrons contributes one of the largest sources of uncertainty on the cross section arising from this selection. This

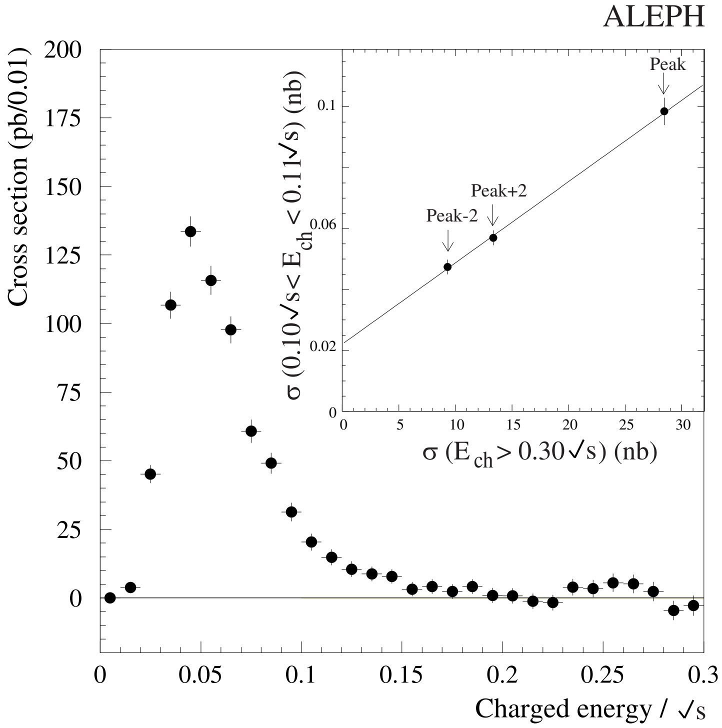

Figure 6: Observed non-resonant hadronic cross section as a function of the normalised charged-track energy. Insert: total hadronic cross section in the charged-track energy interval $(0.10,0.11)\sqrt{s}$ as a function of the cross section for events with charged-track energy greater than $0.3\sqrt{s}$ at three different centre-of-mass energies (peak−2, peak+2, peak). The offset of the straight line fit is the non-resonant contribution for the energy interval $(0.10,0.11)\sqrt{s}$.

background is dominant for events with E_{ch} below $0.1\sqrt{s}$ and is negligible for energies above $0.3\sqrt{s}$. The contamination in the accepted sample is estimated from the data by exploiting the different $\sqrt{s}$ dependence of the resonant (signal) and non-resonant (background) contributions. As an example, the insert of Fig. 6 shows, for three different values of $\sqrt{s}$, the correlation between the cross section for the low E_{ch} interval $(0.10,0.11)\sqrt{s}$, where non-resonant background is expected, and the cross section for $E_{ch} > 0.3\sqrt{s}$, where only Z decays contribute. Assuming a linear dependence, the offset of a straight line fit is a measure of the non-resonant cross section in the low-energy bin $(0.10,0.11)\sqrt{s}$. Similar fits are performed for other bins of charged energy below $0.3\sqrt{s}$ and the resulting non-resonant cross section is shown in Fig. 6 as a function of the charged-track energy. The value of the total non-resonant background in the selected sample is taken as the sum bin by bin of the non-resonant cross section in the interval $(0.1,0.3)\sqrt{s}$. Within errors, this estimate is found to be independent of the choice of the cutoff energy.

In order to determine the level of non-resonant contribution for the different data taking periods, it is necessary to use samples with homogeneous triggering conditions. Four separate determinations of the non-resonant background were performed by splitting the data sample into subsamples from the years 1990, 1991 + 1992, 1993 + 1994 and 1995. The statistical errors are treated as uncorrelated between the different periods.

An additional source of systematic error on the measurement of the two-photon background comes from the fact that events with initial state radiation can mimic a non-resonant process. This effect was evaluated by Monte Carlo and the corresponding cross section was found to be (6.5±4.8) pb where the uncertainty is taken as correlated between the different periods. After subtraction of this ISR contribution from the non-resonant cross section, the two-photon background is measured (from the 1993 + 1994 data sample) to be (78.1 ± 12.0) pb, corresponding to $(0.26 \pm 0.04)\%$ of the peak hadronic cross section.

Another source of systematic uncertainty arises from the accuracy of the hadronisation modelling which affects the charged-track multiplicity and energy distributions. Discrepancies between Monte Carlo and data for these variables affect the efficiency calculation, especially for quark pairs produced at low angle. For these events a fraction of the charged tracks is lost because of the requirements on the track angular acceptance. In order to check the hadron selection efficiency evaluated with the Monte Carlo simulation, real events which are well contained in the detector ($|\cos\theta_{\mathrm{thrust}}| < 0.2$) are used. These events are rotated in space according to the expected thrust angular distribution and the acceptance is calculated by again applying the selection requirements. The same procedure is repeated for fully simulated events and an efficiency difference of $(0.05 \pm 0.03)\%$ is observed for the 1994 data. This is used to assess the systematic uncertainty on the cross section associated with the hadronisation modelling. The same study was repeated for the different energy points with similar results.

Since events with fewer than five charged tracks are not included in the rotated sample, the procedure described above does not check how well this class of events is reproduced in the simulation. To verify this, $\mathrm{q\overline{q}}$ events are selected by a cut on the charged multiplicity in one of the two event hemispheres defined by a plane perpendicular to the thrust axis. A comparison of the multiplicity spectrum in the opposite hemisphere is made between data and Monte Carlo. This comparison leads to a conservative systematic uncertainty of 0.02% after having verified that multiplicities in the two hemispheres are uncorrelated to first order. From the agreement between the data and Monte Carlo distributions of the selection variables and of several individual track parameters, such as the number of hits per track or the transverse track momentum, a further systematic error of 0.02% is derived. The uncertainties related to the Monte Carlo simulation of the detector response are treated as correlated between all points.

All the errors assigned to detector response, Monte Carlo, background and modelling are summarised in Table 9. Combining them yields a total systematic error for the track-based selection of 0.087% at the peak energy.

8.2 Selection based on calorimeters

The other, independent, event selection uses calorimetric data to select hadronic Z decays within a slightly larger acceptance than that for the track based selection. First, a preselection is applied which demands an ECAL energy, as measured by the wire readout, above 7 GeV in the barrel or 1.5 GeV in each endcap and in addition the sum of the ECAL wire energy and HCAL energy from the analogue readout (validated by the digital readout to remove possible noise) is required to be above $0.2\sqrt{s}$. These requirements reduce the two-photon

Table 9: Efficiency, background and systematic errors for the two hadronic selections at the peak point. The values given for the two-photon and Bhabha background are those valid for the 1993 + 1994 data sample.

	Hadronic selection	
	Charged tracks	Calorimeter
Efficiency (%)	97.48	99.07
Background:		
$\tau^+\tau^-$ (%)	0.32	0.44
$\gamma\gamma$ (pb)	78±12	48±9
($\gamma\gamma$ in % of peak cross section)	(0.26)	(0.16)
e^+e^- (pb)	negl.	23 ± 8
(e^+e^- in % of peak cross section)	negl.	(0.08)
$\mu^+\mu^-$	negl.	negl.
Source of systematic uncertainty (%):		
MC simulation of detector response	0.02	0.09
Hadronisation modelling	0.06	0.03
MC statistics	0.02	0.02
Background:		
$\tau^+\tau^-$	0.03	0.05
$\gamma\gamma$	0.04	0.03
e^+e^-	negl.	0.03
Total systematic uncertainty	0.087	0.116
Combined	0.071	

event contamination to a small level. A time window of ±100 ns around the beam crossing, measured on ECAL signals, removes most of the cosmic-ray background. Additional cuts are imposed on events with fewer than five charged tracks to suppress the background from lepton pairs:

- Bhabha events are removed on the basis of their large localised energy deposition in the ECAL; the two most energetic ECAL clusters are required to have energies smaller than 35 and 25 GeV, respectively. Two particular angular regions, the area of overlap between barrel and endcap, where the energy resolution is degraded, and the low angle region, where part of the event may be lost due to ECAL geometrical acceptance, require special care. For these regions, an additional cut is applied, requiring that the summed energy of the two largest ECAL clusters be smaller than 84% of the total calorimetric energy.

- $Z \to \tau^+\tau^-$ events are removed on the basis of their characteristic collimated back-to-back jet structure. The thrust measured with the calorimeters must be less than 0.996 and the minor value of the energy tensor must be larger than 0.03. After these cuts the remaining τ-pair background, estimated from simulated data, is small (0.44%) and is subtracted from the cross section.

- $Z \to \mu^+\mu^-$ decays that pass the initial calorimetric cuts because they have a radiated photon are removed by rejecting events with exactly two tracks, each with four or more associated hits in the outer ten layers of the HCAL. The remaining μ-pair background is negligible.

- Remaining cosmic-ray background within a 100 ns window around the beam crossing is removed as follows: events with exactly one track are rejected unless this track points to the vertex cylinder (2 cm radius and 20 cm length). Events are also rejected if they have fewer than two ECAL clusters of more than 3 GeV. The residual cosmic-ray contamination is calculated on the basis of the properties of the events outside the time window and is found to be negligible.

The selection gives an overall efficiency of 99.07% at the peak energy. Its dependence upon $\sqrt{s}$ is shown in Fig. 5.

The main systematic error arises from the overall calorimeter energy determination. From electrons in the data with energies between 1 and 15 GeV (the energy domain relevant for this analysis) an uncertainty of $\pm 0.5\%$ is determined for the electromagnetic energy scale, the determination being repeated for each data taking period. In a similar way, a typical $\pm 2\%$ uncertainty on the hadronic energy scale is extracted from a year by year calibration using charged pions and from a pre-calibration based on test beam data. These calibration uncertainties induce a 0.09% systematic error on the efficiency evaluation with a correlation between the years of the order of 10%.

The error arising from the modelling of the parton shower was determined by comparing the detector response to hadronic events from different Monte Carlo generators (JETSET, HERWIG and ARIADNE). The selection efficiencies determined from these generators agree within the statistical error. An uncertainty of 0.03% is therefore assigned, corresponding to the statistical significance of the check. This error is treated as fully correlated between energy points and years.

The systematic errors arising from background contamination are treated as correlated between years and energy points, the main contribution coming from the uncertainty on the τ-pair background contribution. This background is estimated from a sample enriched in τ-pairs obtained by selecting events with fewer than seven tracks and $|\cos\theta_{\mathrm{thrust}}| < 0.6$. For this sample the Monte Carlo simulation predicts a τ contamination of 17% after the calorimetric selection. A fit to the total energy distribution in this τ-pair enriched sample allows one to separate the hadronic and τ components and shows that the measured τ yield agrees with the prediction within 11%, leading to an additional 0.05% uncertainty.

Events from two-photon processes are very efficiently suppressed by the preselection. The possible remaining background was estimated using the events in the interval $(0.20,\, 0.35)\sqrt{s}$, where the two-photon events are concentrated. The same method was used as for the track-based selection. As an example, from the 1993 + 1994 data sample a background contribution of (48 ± 9) pb was estimated, which corresponds to $(0.16 \pm 0.03)\,\%$ of the peak hadronic cross section.

The remaining Bhabha background is studied in a similar way. As it is concentrated at small angles, an enriched sample, obtained by selecting events with fewer than five tracks and $|\cos\theta|>0.95$, is compared with the full sample as a function of the beam energy. Here, the background term is dominated by Bhabha events from the t channel exchange. An an example, an estimated background of (23 ± 8) pb is removed from the cross section calculation for the 1993 and 1994 data samples combined. Four separate determinations of the two-photon and Bhabha background were performed corresponding to four different time periods, as for the track-based selection, with uncertainties fully correlated within a given period and uncorrelated between periods.

Combining all the errors, summarised in Table 9, gives a total systematic error of 0.116% for the calorimetric selection.

8.3 Combination of the two hadronic selections

The hadronic cross sections are computed for each of the two selections. Although the calorimetric selection uses track counting to some extent for background rejection, it is largely independent of the efficiency of the TPC. Therefore, the measured cross sections are averaged and the systematic error on the average is reduced. The statistical errors are combined taking into account the 96% event overlap between the two samples. To combine the systematic uncertainties, correlations between the two analyses are taken into account as follows:

- The τ-pair background contributes to the two selections; in both cases it is estimated from Monte Carlo, and the number of τ events common to both samples over the total leads to a 72% correlation between the two corresponding systematic uncertainties.
- Uncertainties arising from the imperfect detector simulation of tracks or calorimetric energy deposits are considered as uncorrelated; this includes errors related to the calorimeter calibration uncertainties.
- Uncertainties associated with the $q\overline{q}$ hadronisation modelling are estimated with two different methods: from data for the charged-track based selection, and comparing Monte Carlo and data for the calorimetric selection. These contributions are treated as uncorrelated.
- Non-resonant background contributions have been studied for the two selections and from their overlap a 28% correlation is evaluated.

The two measurements are compared for each energy point and found to be in good agreement within the uncorrelated statistical errors as shown in Fig. 7. They are combined, taking into account the above mentioned correlations. The resulting systematic error is 0.071% at peak energy. Table 21 in Section 12 summarises the combined hadronic cross section results for the different energy points. Typical values of the systematic error correlations are 68% between peak points of different years and 95% between points of the same year.

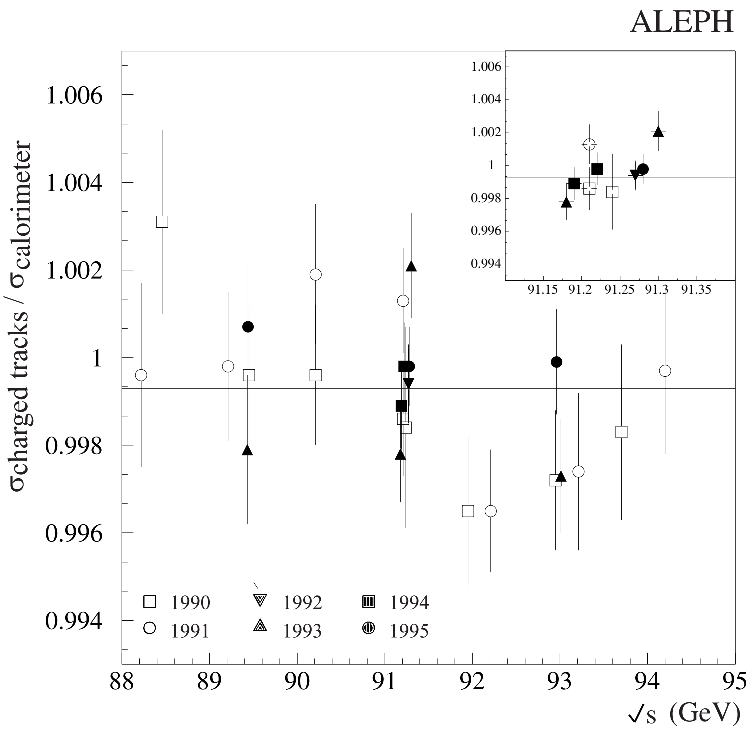

Figure 7: Ratio of cross sections of the two hadronic selections as a function of centre-of-mass energy. The insert is an enlargement of the measurements around the Z peak.

9 Aspects common to all leptonic Z decays

9.1 Definitions and preselection

The analyses developed to measure the lepton cross sections and forward-backward asymmetries share some common definitions which are specified here.

Two variables are employed to select charged particle tracks originating from the interaction region: d_0, which measures the distance of closest approach of the tracks to the beam axis and z_0, defined as the z coordinate of the point on the track where d_0 is measured. Tracks having at least four measured space coordinates in the TPC, $|d_0| < 5$ cm and $|z_0| < 10$ cm will be hereafter referred to as "good".

An electromagnetic cluster is accepted as a photon candidate if its energy exceeds 350 MeV and if its barycentre is at least 2 cm from the closest charged track extrapolation. Clusters reconstructed in the luminosity calorimeters LCAL and SICAL are excluded from the analysis.

The acollinearity η is defined as 180° minus the angle between the two lepton directions. Depending on the various analyses, these directions are based either on the leading tracks or on the jet momenta.

The scattering angle θ^* between the incoming e^- and the outgoing negative lepton is defined as

$$\cos\theta^* = \frac{\cos\left[\frac{1}{2}\left(\theta_{\ell^-} - \theta_{\ell^+} + \pi\right)\right]}{\cos\left[\frac{1}{2}\left(\theta_{\ell^-} + \theta_{\ell^+} - \pi\right)\right]}, \tag{5}$$

where θ_{ℓ^-} and θ_{ℓ^+} are the polar angles of the lepton and antilepton, respectively. The variable $\cos\theta^*$ gives the centre-of-mass scattering angle even in the case of hard collinear radiation from one of the initial state leptons.

A loose preselection, which is common to all of the lepton-pair channels, is applied mainly to suppress hadronic events, as well as background from beam-gas, two-photon and cosmic ray events. This preselection demands a number of good tracks between two and eight and at least one good track with momentum exceeding 2 GeV/c. If more than four good tracks are found, the event is divided into two hemispheres by a plane perpendicular to the thrust axis. Each of the tracks is then required to form an angle β with respect to the sum of the track momenta in the same hemisphere such that $\cos\beta > 0.85$. After this preselection, the data sample consists of approximately 85% dileptons, 10% $\gamma\gamma$ and 5% $\mathrm{q\overline{q}}$ events.

9.2 Acceptance

The phase space acceptance of the selections is defined by a cut in $\cos\theta^*$, $|\cos\theta^*| < 0.9$, and a cut on the acollinearity, which is generally $\eta < 20^\circ$ for the lepton cross section measurements and slightly looser for the forward-backward asymmetries (as specified in Section 11). Assuming an angular distribution proportional to $1 + \cos^2\theta^*$, the condition $|\cos\theta^*| < 0.9$ alone reduces the acceptance to 85.7%. For the $\mathrm{e^+e^-}$ final state the $\cos\theta^*$ range is restricted to the range -0.9 to $+0.7$ to minimise the contribution from the t channel, leading to an s channel angular acceptance at the peak of approximately 72.4%.

The acceptance, determined with KORALZ, is corrected with the event generator KK to take into account QED ISR-FSR interference. This correction is of the order of a few 10^{-4} ($(2.5 \pm 0.6)10^{-4}$ at the peak [35]).

Under the assumption of a single photon collinearly radiated from the initial state, the acollinearity cut is equivalent to a polar angle dependent cut on the invariant mass $\sqrt{s'}$ of the final state particles, according to the expression

$$\frac{s'}{s} = \frac{\sin\theta_{\ell^+} + \sin(\theta_{\ell^+} + \eta) - |\sin\eta|}{\sin\theta_{\ell^+} + \sin(\theta_{\ell^+} + \eta) + |\sin\eta|}\,. \tag{6}$$

From this equation, the reduction of phase space induced by a 20° acollinearity cut corresponds approximately to $\sqrt{s'} > 0.8\sqrt{s}$.

As explained in Section 8.1 for the hadronic final state, the different amount of photon emission as a function of centre-of-mass-energy induces a variation of the acceptance. For the leptonic channel, this variation is typically of the order of 2% and is taken into account in the acceptance calculation.

9.3 Treatment of the t channel

Three different contributions enter into the $e^+e^- \to e^+e^-$ process, the s channel, the t channel and the interference between the two. Throughout this paper, the sum of the t channel and interference terms will be referred to as the t channel contribution to the cross section and denoted σ_{sub}. The accuracy of the correction for the t channel contribution is limited by the present generators or formulae used to calculate it. In order to keep this uncertainty on the cross section below 0.1%, the angular range is restricted to $-0.9 \leq \cos\theta^* \leq +0.7$ since the t channel contribution dominates at small polar angles. This contribution is evaluated theoretically, and subtracted in order to extract the s channel cross section. After this subtraction the e^+e^- final state can be treated, for the leptonic width, in the same manner as the other lepton channels.

The theoretical treatment of the t channel is based on the semi-analytical program ALISTAR, a slightly modified version of the program ALIBABA [36] which allows the cross section to be calculated in $\cos\theta^*$ rather than $\cos\theta$. ALISTAR incorporates photonic corrections using the leading-log approach and includes first-order non-log terms. In addition, weak corrections are fully incorporated to first order.

Table 10 gives the values of the total cross sections and of the subtraction cross sections calculated with ALISTAR within the angular acceptance. The t channel contributes 12% of the total cross section at $\sqrt{s} = M_Z$. Therefore, to have an accuracy of order 0.1% on the s channel, one must subtract the t channel with a 1% precision.

Three different sources of systematic errors on the subtraction cross section are considered. These are errors due to theoretical uncertainties, to numerical precision in the analytical program and finally to the variation of the results with respect to the input parameters.

The theoretical uncertainty is estimated from missing terms, mainly QED corrections, which do not include sub-leading second order terms proportional to $\alpha^2 L$, with $L = \log(s/m_e{}^2)$, and initial-state pair production. Also missing are some weak corrections. The overall theoretical uncertainty is estimated in Ref. [37] to be 1.1 pb at the peak, and is almost independent of the centre-of-mass energy, as shown in Table 11.

The numerical stability of ALISTAR arises mainly from the fact that some of the non-leading log terms are evaluated using a numerical integration over a five-dimensional phase space. This leads to an accuracy of approximately 0.3 pb regardless of energy.

A further source of possible uncertainty in the value of the subtraction cross section arises from the errors associated with the input parameters. The only non-negligible variation

Table 10: Total e^+e^- cross section σ_{tot} and subtraction cross section σ_{sub} as a function of energy, calculated with ALISTAR inside the angular acceptance -0.9 $\leq \cos\theta^* \leq +0.7$.

$\sqrt{s}$ (GeV)	88.46	89.44	90.21	91.20	91.95	92.97	93.70
σ_{tot}(pb)	420.2	612.3	907.25	1219.4	911.81	502.9	359.2
σ_{sub}(pb)	219.1	241.6	248.32	144.8	36.20	5.9	11.9

Table 11: Summary of the systematic errors in the t channel cross section calculation.

Nominal energy	Peak−3	Peak−2	Peak−1	Peak	Peak+1	Peak+2	Peak+3
Theoretical error (pb)	1.1	1.2	1.2	1.1	1.2	1.1	1.0
Numerical error (pb)	0.3	0.3	0.3	0.3	0.3	0.3	0.3
Input parameters (pb)	-	-	-	0.5	0.2	-	-
Total error (pb)	1.1	1.2	1.2	1.2	1.2	1.1	1.0

comes from the uncertainty on M_{Z} through the interference term, which is proportional to $(\sqrt{s} - M_{\mathrm{Z}})$.

The three sources of uncertainties are summarised in Table 11 for each energy point. Their values are added in quadrature to obtain the final uncertainties. At the peak, the total error is 1.2 pb and represents 0.11% of the s channel cross section within the acceptance; the uncertainty induced on the Bhabha forward-backward asymmetry amounts to 0.0011.

10 Measurement of the lepton cross sections

Two analyses were developed to measure the lepton cross sections. The first one, referred to as *exclusive*, is based on three independent selections each aimed at isolating one lepton flavour and still follows the general philosophy of the analysis procedures described in Refs.[1–4]. The second one, called *global*, is new: after a common rejection of hadron and $\gamma\gamma$ contaminations, the dilepton candidates are exclusively classified in one of the three lepton categories. For the lepton cross section the statistical error is of the order of 0.15% and both analyses are designed to reduce the systematic uncertainties to a matching level of less than 0.1%.

10.1 Cross section definition

The cross sections for the lepton final states are defined to be inclusive of the emission of any number of photons. They are evaluated within the phase space $\sqrt{s'} > 2m_\tau$.

The total cross section for the process $e^+e^- \to \ell\ell$ is computed as

$$\sigma_{\ell\ell} = \frac{1}{\varepsilon_{\mathrm{acc}}} \left(\frac{N_{\mathrm{sel}}(1 - f_{\mathrm{bkg}})}{\varepsilon_{\mathrm{sel}} \mathcal{L}} - k\sigma_{\mathrm{sub}} \right) + \delta\sigma_{\ell\ell}^{\ell\ell\mathrm{V}} , \quad (7)$$

where N_{sel} is the number of selected events, f_{bkg} is an energy dependent background fraction, $\mathcal{L}$ is the time integrated luminosity, $\varepsilon_{\mathrm{acc}}$ is the acceptance (discussed in Section 9.2) and $\varepsilon_{\mathrm{sel}}$ is the selection efficiency inside the acceptance. The coefficient k is equal to one for $\ell = \mathrm{e}$ and zero otherwise. In fact in the case of $\mathrm{e^+e^-} \to \mathrm{e^+e^-}$, because only the s channel is sensitive to the Z resonance parameters, the cross section is defined as the pure s channel part, i.e., the t channel cross section σ_{sub} within the acceptance is subtracted. Since, after this subtraction, the Bhabha angular distribution is the same as for muons, the acceptance calculation is based on $\mu^+\mu^-$ events from the Monte Carlo KORALZ . The term $\delta\sigma_{\ell\ell}^{\ell\ell\mathrm{V}}$ represents a correction which takes into account the different selection efficiency for signal events in the $\ell^+\ell^-\mathrm{V}$ topology, where V is any pair of fermions. This will be discussed further in Section 10.3.

10.2 Systematic uncertainties due to preselection and acceptance

The main sources of systematic uncertainty associated with preselection and acceptance definition arise from tracking inefficiencies and from any systematic mis-measurement of the angles, namely $\cos\theta^*$ and acollinearity.

Track losses are mainly due to charged particles which are badly reconstructed because they enter a TPC insensitive region or have low momentum. For electrons there is an additional component due to loss of tracks following hard bremsstrahlung in the material of the inner detector. A comparative study between Monte Carlo and data is made based on $\mathrm{e^+e^-}$ events tagged with the calorimeters. Good agreement is found within the statistical errors of the test which are quoted as systematic uncertainties (Table 12). Since an independent study is performed each year, the systematic errors are fully correlated between different energy points of the same year, but uncorrelated between different years. The systematic uncertainty related to the TPC cracks and reconstruction problems is fully correlated for the three lepton flavours.

The sources of angular systematic errors considered are the position of the TPC end-plates, the knowledge of the TPC drift velocity and the energy and spatial resolution of neutral particles in the calorimeters. Of these sources, only the first one is found to give a non-negligible effect, which is estimated using toy Monte Carlo techniques.

For $\mathrm{e^+e^-}$ final states, the possible error in the determination of the $\cos\theta^*$ sign, for ambiguous cases when both leptons have the same measured charge, must also be considered due to the asymmetric acceptance. This induces a negligible systematic uncertainty on the acceptance, as discussed in Sections 10.4.3 and 10.5.2. The accuracy of the simulation of the acollinearity depends on the description of initial and final state radiation. This is checked by comparing in data and Monte Carlo muon events rejected by the acollinearity cut. Agreement is observed and the systematic error is set to the statistical power of the test. All uncertainties related to systematic mis-measurements of the angles are treated as fully correlated between all points and lepton flavours.

Table 12 summarises the main sources of systematic uncertainty discussed in this section.

10.3 Four-fermion processes

The four-fermion processes relevant for the dilepton selection are $\mathrm{e^+e^-} \to \ell^+\ell^-\mathrm{f\bar{f}}$, where ℓ is a lepton and f any fermion. The corresponding four groups of gauge-invariant diagrams are shown in Fig. 8. Here, only diagrams of group (a), (b) and (c) are considered, while diagrams of group (d), corresponding to $\gamma\gamma$ events, are discussed in Sections 10.4 and 10.5 as a source of background.

Table 12: Sources of systematic error on the dilepton cross sections due to preselection and acceptance requirements for peak 1994 data; values are expressed as a percentage of the dilepton cross sections.

Source of relative uncertainty (%)	e^+e^-	$\mu^+\mu^-$	$\tau^+\tau^-$
TPC Tracking	0.05	0.03	0.03
$\cos\theta^*$	0.02	0.01	0.01
ISR/FSR sim.	0.03	0.03	0.03
Total acceptance	0.06	0.04	0.04
MC statistics	0.05	0.06	0.07

With the pair of fermions (either $\ell^+\ell^-$ or $f\overline{f}$) with the lowest invariant mass denoted by V, these processes can be classified in two ways: $q\overline{q}V$ where V is a pair of leptons and $\ell^+\ell^-V$ where V is any pair of fermions. Events with the $q\overline{q}V$ topology are to be treated as background to the lepton selection while those with the $\ell^+\ell^-V$ topology are to be considered as signal because this is how the inclusive leptonic cross section is defined. This definition is motivated by the near complete cancellation of the contribution from diagrams 8(a), 8(b) and 8(c) with the interference of the two-loop final state vertex correction diagram with the lowest order one. As a result, the inclusive leptonic cross section is not singular in the limit of vanishing lepton masses.

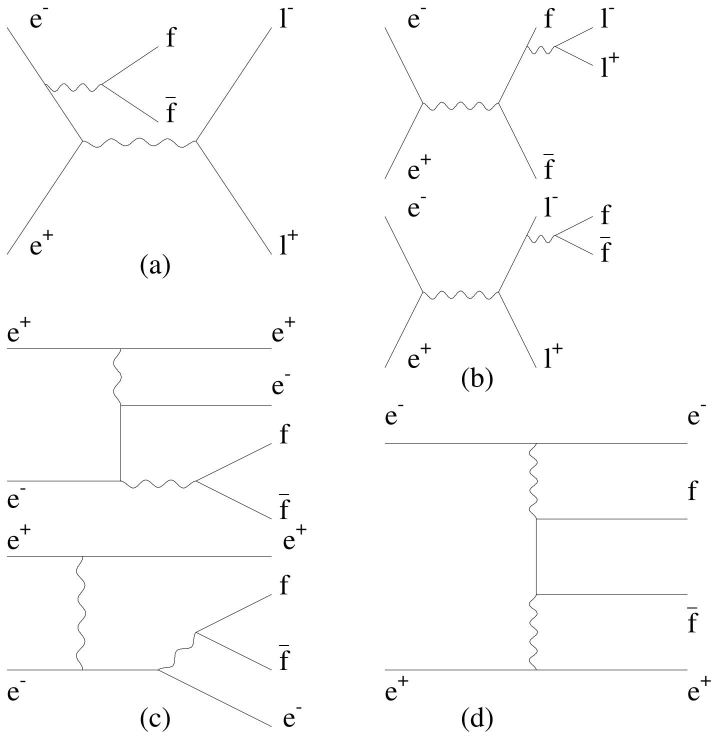

Figure 8: Diagrams contributing to $\ell\ell V$ processes.

The $\ell^+\ell^-$V events are included in the final cross sections but they are not taken into account by UNIBAB and KORALZ. Consequently, it is necessary to consider these events separately in the efficiency calculation. Samples of e^+e^-V, $\mu^+\mu^-$V and $\tau^+\tau^-$V events were produced with the four-fermion generator FERMISV. The efficiency $\varepsilon_{\ell\ell\mathrm{V}}$ of the selection procedure for these events was calculated and, where different from the standard efficiency $\varepsilon_{\ell\ell}$, a correction $\delta\sigma_{\ell\ell}^{\ell\ell\mathrm{V}}$ was applied to the cross section according to the expression $\delta\sigma_{\ell\ell}^{\ell\ell\mathrm{V}} = (\varepsilon_{\ell\ell} - \varepsilon_{\ell\ell\mathrm{V}})\,\sigma_{\ell\ell\mathrm{V}}$. Details on the size of these corrections for the different leptonic final states are given in Sections 10.4 and 10.5. For all selections, the $\ell\ell$V correction is affected by a systematic uncertainty arising from the simulation which is estimated in Ref. [38] to be lower than 5%. Another source of systematic uncertainty common to all selections comes from the procedure used to separate, in the Monte Carlo simulation, $\ell^+\ell^-$V events with V$\rightarrow$ $q\overline{q}$, which are signal, from $q\overline{q}$V events with V$\rightarrow$ $\ell^+\ell^-$, which are background, when both $q\overline{q}$ and $\ell^+\ell^-$ pairs have high masses (around 20–30 GeV/c^2). Since this ambiguity arises in less than 10% of the events, a systematic uncertainty of 10% is attributed to the $\ell^+\ell^-$V correction.

10.4 Exclusive cross section measurements

10.4.1 Exclusive muon cross section measurement

The muon-pair events are selected by taking advantage of the low charged multiplicity, the high momenta of the two muons and the characteristic energy deposition pattern in the detector.

Kinematic selection

The preselection and $\cos\theta^*$ cuts described in Sections 9.1 and 9.2 are applied; the lepton directions are defined as the momenta of the two leading tracks, which are required to be oppositely charged. The acollinearity cut depends on the event topology as described below.

To reduce the contamination from cosmic events and beam related background, events are accepted only if the total number of ITC hits associated to the two leading tracks is at least two, if the two leading tracks have $|d_0| < 2\,\mathrm{cm}$ and $|z_0| < 5\,\mathrm{cm}$, and if the sum of their momenta is less than $1.5\sqrt{s}$. The acceptance $\varepsilon_{\mathrm{acc}}$ from Monte Carlo events at the peak is (85.35 ± 0.05)%.

The contamination due to two-photon interactions is reduced to a negligible level by requiring the momentum of the leading track p_1 to be larger than $0.38\sqrt{s}$. After this cut, the fraction of accepted events at the peak is (85.13 ± 0.05)%. The distributions of the momentum of the leading track p_1 in events which fulfil the acceptance cuts and the momentum of the second fastest track p_2 in events which fulfil the p_1 cut are shown in Fig. 9.

To suppress the $\tau\tau$ background, additional cuts on the reconstructed event kinematics are applied. An event is retained if it fulfils at least one of the following conditions:

- The second highest momentum track track p_2 exceeds $0.38\sqrt{s}$ and the acollinearity η is smaller than 20°. In the approximation of only ISR photons, emitted by one beam

(Eq. 6), the effect of these cuts is to reject events with photon energy larger than $\simeq 12\,\mathrm{GeV}$. The fraction of events, after the p_1 cut, that passes this requirement is 95.12%.

- The acollinearity η is less than 10 mrad; this retains signal events with hard FSR ($E_\gamma > 10\,\mathrm{GeV}$), collinear to one of the muons. The fraction of events selected only by this cut is 0.95%.
- A photon is identified in the ECAL acceptance ($|\cos\theta_\gamma| < 0.98$) consistent in energy and position with the $\mu^+\mu^-\gamma$ hypothesis. This requires that the measured photon energy E_γ^{meas} be equal to the expected energy E_γ^{exp} within four times the estimated photon energy resolution; E_γ^{exp} is obtained from the directions of the two leading charged tracks and of the photon by imposing energy and momentum conservation:
$$E_\gamma^{\mathrm{exp}} = \frac{\sqrt{s}\sin\theta_{\mu^+\mu^-}}{\sin\theta_{\mu^+\mu^-} + \sin\theta_{\mu^+\gamma} + \sin\theta_{\gamma\mu^-}}.$$
In addition, the angle between the photon and the closest of the two leading tracks must be larger than 30 mrad and the event must be planar, that is $|\cos\theta_{\hat{n}\gamma}| < 0.1$, where $\theta_{\hat{n}\gamma}$ is the angle between the photon direction and the normal to the plane of the two leading charged particles. The sum of the photon energy and the momenta of the two leading tracks is required to exceed $0.85\sqrt{s}$. This set of cuts selects events with hard and non collinear FSR. The fraction of events selected only by this set of cuts is 2.69%.

The efficiency after all the above kinematic cuts is $(84.08 \pm 0.05)\%$ at the peak, with a dependence on centre-of-mass energy which is less than 2%.

Muon identification

The last step in the selection involves the identification of the muons (discussed in Section 3) to eliminate the Bhabha background, topologically very similar to the muon-pair events, and further reduce the $\tau\tau$ contamination. For all events selected by the kinematic selection, it is required that at least one of the two leading tracks be identified as a muon.

The muon identification efficiency is measured with data at each energy point by applying all cuts except muon identification and counting the events in which one or both muons are tagged. Since a bias on the efficiency measurement could be induced by the presence of a residual $\tau^+\tau^-$ contamination, charged tracks are required to be minimum ionising in ECAL and HCAL. According to Monte Carlo simulation this filter reduces the $\tau^+\tau^-$ contamination in the singly tagged events from 5% to 2.5% and the bias on the event identification efficiency $\varepsilon_{\mu\mu}^{\mathrm{id}}$ from -5.2×10^{-5} to -2.1×10^{-5}.

Correlations in the identification efficiency between the two muons introduced by the presence of inactive zones in the HCAL or muon chambers are evaluated with the $\mu^+\mu^-$ Monte Carlo simulation, leading to a correction factor on the efficiency of $1 + (0.318 \pm 0.020) \times 10^{-3}$. After all corrections, the mean identification efficiency is measured to be $\varepsilon_\mu^{\mathrm{id}} = 0.9763 \pm 0.0003$ for a single track and $\varepsilon_{\mu\mu}^{\mathrm{id}} = 0.99976 \pm 0.00001$ for the event, where the uncertainties are statistical only. The inefficiency is essentially due to aligned inactive zones in the HCAL and in the muon chambers.

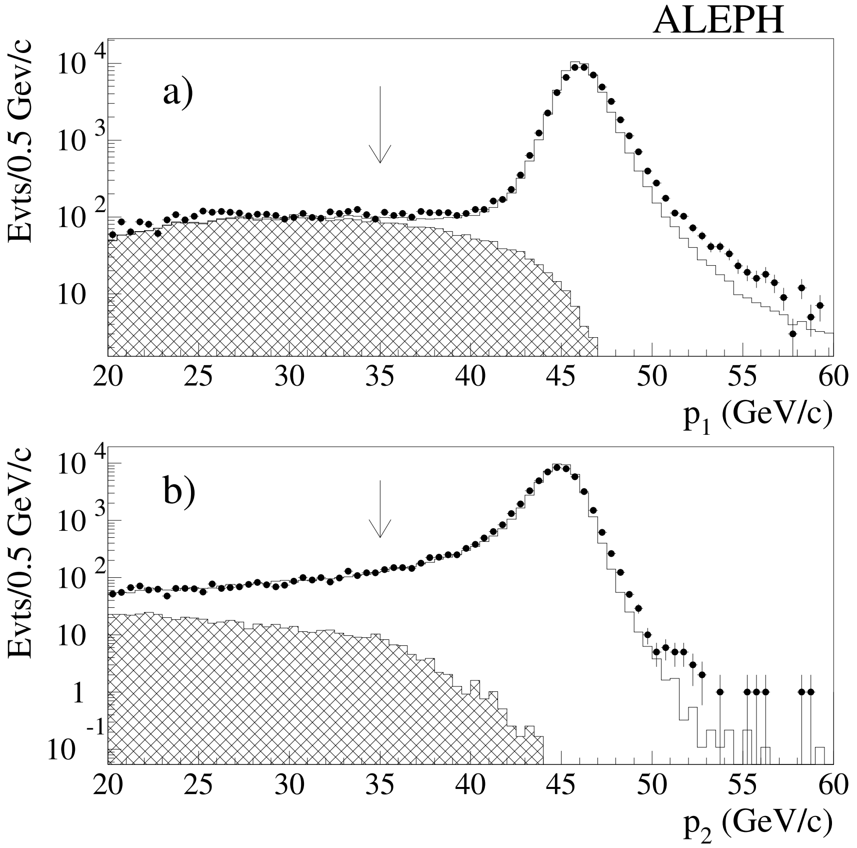

Figure 9: Exclusive $\mu^+\mu^-$ selection: distribution of (a) the momentum p_1 of the leading track in events that fulfil the acceptance cuts and (b) the momentum p_2 of the second fastest track in events that fulfil the p_1 cut. Only events with at least one identified muon are plotted here. The arrows indicate the applied cuts. Dots are the data, the open histogram is the Monte Carlo for signal plus background and the hatched histogram is the $\tau^+\tau^-$ Monte Carlo.

As a check of the systematic uncertainty, the efficiencies measured with this method were compared with those derived by using a sample of $\mu^+\mu^-$ events selected with the same kinematic cuts but requiring minimum ionising particles in ECAL only. The difference was found to be negligible with the exception of a period in 1995 when 1/12 of the HCAL and muon chamber barrel were affected by a readout problem. Therefore the 1995 peak, peak+2 and peak−2 efficiencies were corrected and an additional systematic error, 0.2×10^{-3} (relative) at the peak point, was assigned to the cross sections measured during these periods. The overall efficiency of this selection for 1994 is $\varepsilon_{\rm acc}\varepsilon_{\rm sel} = (84.06 \pm 0.05)\%$.

Background and $\ell\ell$V correction

After the complete selection, the most important source of background originates from $e^+e^- \rightarrow \tau^+\tau^-$ events. From Monte Carlo simulation, this background fraction $f_{\rm bkg}$ is estimated to be $(0.266 \pm 0.006)\%$ at the peak. The background from Bhabha events is also evaluated from simulated events and is found to be negligible. The residual cosmic-ray contamination is estimated for each energy point by loosening the $|z_0|$ cut and using the number of additional events found to estimate the number of background events accepted by the standard $|z_0|$ requirements. The average resulting background fraction is $(4.0\pm0.5)\times10^{-4}$.

The additional correction $\delta\sigma_{\mu\mu}^{\mu\mu\mathrm{V}}$ for the $\ell\ell$V events, evaluated as described in Section 10.3, amounts to 1.2 pb for the peak cross section.

Systematic checks

The study of the systematic uncertainties related to the acceptance cuts are described in Section 10.2. The systematic uncertainties related to the cut on the leading track momentum were studied by investigating both the momentum measurement calibration and resolution.

The momentum calibration was studied by rescaling the particle momenta in order to equalise the peak position of the muon momentum distributions in different polar angle regions and reselecting the events. The relative differences between the re-evaluated cross sections and the original ones are consistent with zero. A systematic error equivalent to the statistical accuracy of the test is therefore assumed, varying between 6×10^{-5} in 1994 and 2.4×10^{-4} in 1990. Because the momentum correction factors were evaluated year by year, this systematic uncertainty is considered to be correlated for data collected in the same year but uncorrelated from year to year.

The impact of the momentum resolution was investigated by applying to the simulated track momenta a Gaussian smearing, the width of which is a function of the polar angle, to match the resolution observed in the data. The relative change in the cross section and the statistical error on the change provide the related systematic uncertainties. These are of the order of 6×10^{-5} at the peak, with the exception of the 1990 data, where the uncertainty degrades to 5×10^{-4} due to the absence of VDET.

As described previously, about 2% of the simulated events are selected as $\mu^+\mu^-\gamma$ events with a photon detected in ECAL. For this class of events the most critical cut is that on the difference between the expected and measured photon energy, which is very efficient in reducing the $\tau\tau$ background. The systematic uncertainties related to this cut were investigated by changing the photon energies to make the $E_\gamma^{\mathrm{exp}} - E_\gamma^{\mathrm{meas}}$ distributions identical in data and Monte Carlo. The resulting relative systematic uncertainty on the cross sections is 5×10^{-4}, which is treated as correlated between all points since it is mainly due to the Monte Carlo description of the photon showers.

The simulation of the radiative events was also checked by comparing the results of the standard analysis with those obtained by applying a looser $(0.24\sqrt{s})$ momentum cut to the next-to-leading track, and no $\mu^+\mu^-\gamma$ selection. The systematic uncertainty estimated with this check is about 5×10^{-4}, correlated between all points.

Table 13 summarises the relative systematic uncertainties for data at peak energy. The correlation coefficients between points at equivalent centre-of-mass energies but from different years are typically in the range (75–90)%, decreasing to (15–35)% for points from the same year.

Table 13: Exclusive $\mu^+\mu^-$ selection: examples of relative systematic uncertainties (in %) for the 1994 (1995) peak points.

Source	$\Delta\sigma/\sigma$ (%)
Acceptance	0.05
Momentum calibration	0.006 (0.009)
Momentum resolution	0.005
Photon energy	0.05
Radiative events	0.05
Muon identification	$\simeq$ 0.001 (0.02)
Monte Carlo statistics	0.06
Total	0.10 (0.11)

10.4.2 Exclusive tau cross section measurement

Tau-pair event selection is mainly based on the following characteristics of $\tau^+\tau^-$ events: low particle multiplicity, narrow jets, and presence of undetected neutrinos.

Kinematic selection

The event selection makes use of the following energy-flow objects: charged particles having $|d_0| < 2$ cm and $|\cos\theta| < 0.95$, photons with energy greater than 1 GeV, and neutral hadrons with energy greater than 1.5 GeV. The selected energy-flow objects are used to calculate the thrust axis and the event is divided in hemispheres by a plane perpendicular to this axis. The tau directions are defined as the vector sum of the momenta of the selected objects in each hemisphere.

After the preselection cuts described in Section 9.1 are applied, events are retained if they have at least one charged track per hemisphere and at most eight charged tracks in total; the acceptance cuts described in Section 9.2 are then applied. According to the Monte Carlo, the fraction of signal events surviving these requirements is $\varepsilon_{\rm acc} = (82.56 \pm 0.07)\%$ at the peak. Further background rejection is obtained by requiring:

- either the total reconstructed energy $E_{\rm rec}$ to be larger than $0.175\sqrt{s}$ or the absolute difference between the transverse momenta of the jets to be greater than $0.033\sqrt{s}$; this is to reduce the two-photon background;
- the sum of the momenta of the leading charged track from each hemisphere to be smaller than $0.8\sqrt{s}$, in order to remove Bhabha and dimuon events;
- at least one charged track with $|z_0| < 5\,$cm and $|d_0| < 1\,$cm to reject cosmic-ray events.

Rejection of specific background sources

In the subsample of events (designated $\mathrm{q\overline{q}}$-like) which fulfil at least one of the following two additional criteria:

- the maximum hemisphere invariant mass is larger than 3 GeV/c^2,
- both hemispheres have more than one good charged particle or an invariant mass larger than 0.8 GeV/c^2,

the contamination from hadronic Z decays is further reduced by applying the following cuts:

- $\mathrm{N}_1^{\mathrm{obj}}\mathrm{N}_2^{\mathrm{obj}} < 50$ and $\theta_1^{\mathrm{op}}+\theta_2^{\mathrm{op}} < 0.30$ rad, where $\mathrm{N}_i^{\mathrm{obj}}$ is the number of energy-flow objects and θ_i^{op} is the largest angle between two charged tracks in the ith hemisphere,
- the minimum hemisphere invariant mass is required to be <1.8 GeV/c^2 (this cut is relaxed to 3 GeV/c^2 if at least one hemisphere has only one charged particle).

An event is said to be Bhabha-like if all charged tracks are identified as electrons. Here, charged tracks pointing less than 3 cm away from the ECAL cracks are also called electrons unless they are positively identified as muons. The fractions of $\mathrm{e}^+\mathrm{e}^-$ and $\tau^+\tau^-$ events tagged as Bhabha-like after the initial cuts are 99.5% and 8%, respectively.

Correspondingly, dimuon-like events have either both leading charged tracks identified as muons [6] or one leading charged track identified as a muon and the energy in the opposite hemisphere in excess of $0.45\sqrt{s}$. The fractions of $\mu^+\mu^-$ and $\tau^+\tau^-$ events tagged as dimuon-like at this level are 98.8% and 7%, respectively.

Final Bhabha and dimuon rejection is achieved by applying total energy related cuts to Bhabha-like and dimuon-like events. The total energy $\mathrm{E}_{\mathrm{tot}}$ is defined as $\mathrm{E}_{\mathrm{rec}} + \mathrm{E}_{\mathrm{rad}}$, where $\mathrm{E}_{\mathrm{rec}}$ is the total reconstructed energy and $\mathrm{E}_{\mathrm{rad}}$ is the energy of photon(s) collinear to the beam, computed from the jet directions and imposing four-momentum conservation. Possible losses of photons due to ECAL cracks are tagged using the variables $\mathrm{D}_{\gamma,i}$, defined by taking the tangent at the origin to the leading track in each hemisphere, extrapolating it to the ECAL, and computing the minimum distance from the cracks. Bhabha rejection is obtained by applying a staggered cut in the variables $\mathrm{D}_{\mathrm{min}} = \min(\mathrm{D}_{\gamma,i})$ and $\mathrm{E}_{\mathrm{tot}}$; events are retained if $\mathrm{E}_{\mathrm{tot}} < 0.8\sqrt{s}$ when $\mathrm{D}_{\mathrm{min}} > 6$ cm, or $\mathrm{E}_{\mathrm{tot}} < 0.7\sqrt{s}$ when $\mathrm{D}_{\mathrm{min}} < 6$ cm. Dimuon rejection is obtained by requiring $\max_{\mathrm{E}} = \max(P_{\ell,1}, P_{\ell,2}, \mathrm{E}_{\mathrm{tot}}/2) < 0.45\sqrt{s}$, where $P_{\ell,i}$ are the leading momenta.

Finally, events with two charged particles, momentum imbalance less than 15% of the sum of the reconstructed momenta and ECAL energy less than $0.3\sqrt{s}$ are required to have more than four ITC hits associated with the leading tracks, to reduce the cosmic-ray contamination.

The distributions for some of the variables used in defining the selection cuts are shown for 1994 data in Fig. 10.

Background

The background fractions are estimated using data and Monte Carlo simulations; as an example, the total contamination f_{bkg} and the breakdown of the contributing sources are given in Table 14, as determined for the 1994 data sample.

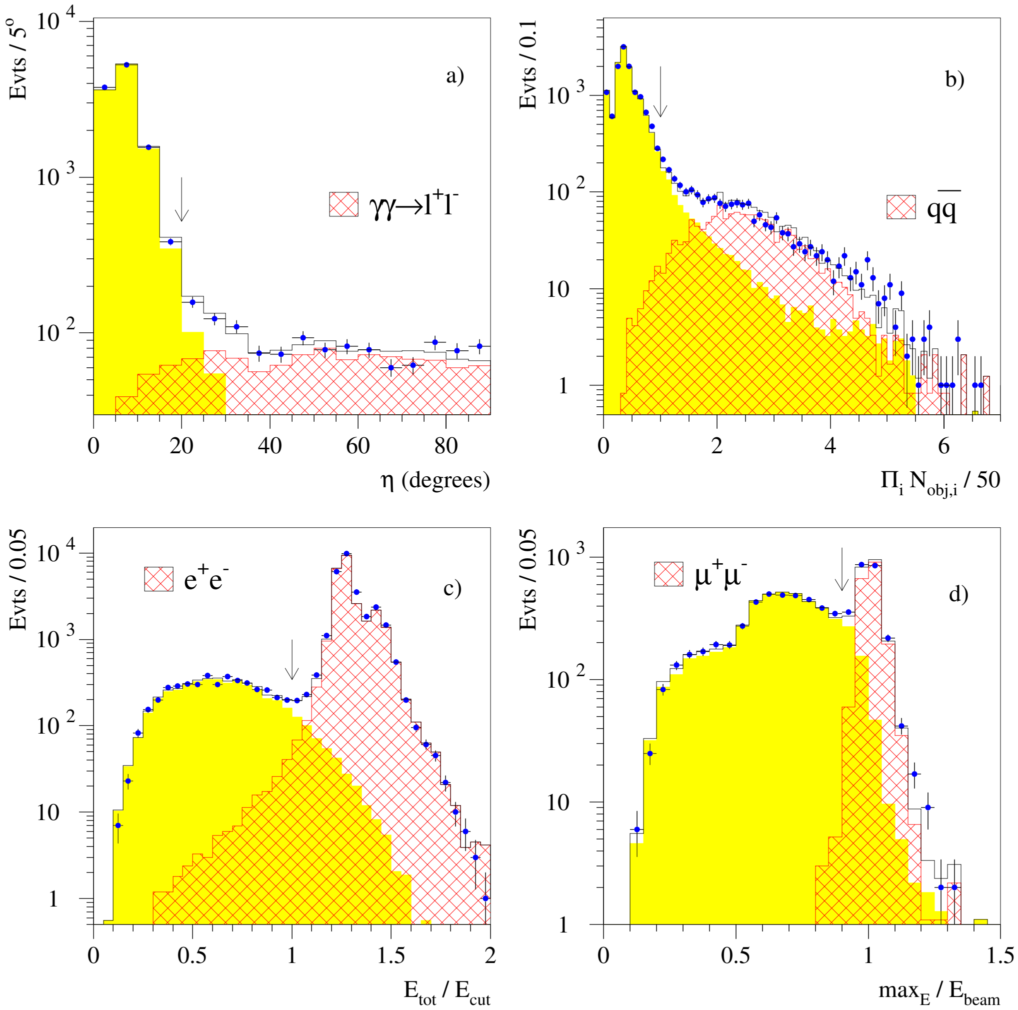

Figure 10: Exclusive $\tau^+\tau^-$ selection: distribution of some of the variables used in the selection; see text for the description of the variables. The dots represent the 1994 data, the shaded areas the $\tau^+\tau^-$ Monte Carlo and the crossed-hatched areas the dominant background rejected by the cut on the displayed variable. a) Acollinearity for events selected by applying all the other selection cuts; b) $\mathrm{N}_1^{\mathrm{obj}}\mathrm{N}_2^{\mathrm{obj}}$ for $\mathrm{q\bar{q}}$-like events, normalised to the value of the cut applied; c) $\mathrm{E_{tot}}$ for Bhabha-like events, normalised to the value of the cut applied; d) $\mathrm{max_E}$ for dimuon-like events. The arrows indicate the position of the cuts.

The hadronic and two-photon contaminations were measured on the data by fitting the distributions for the relevant Monte Carlo observables; these were checked on enriched samples of $q\bar{q}$ and two-photon events and the assigned errors (15% and 10%, respectively) reflect the observed level of agreement between data and Monte Carlo.

The contamination due to electron and muon pairs depends on the lepton identification

Table 14: Exclusive $\tau^+\tau^-$ selection: breakdown of the contributions to the total background contamination $f_{\rm bkg}$ in the 1994 data sample.

Source	Fraction (%)
e^+e^-	0.67 ± 0.05
$\mu^+\mu^-$	0.10 ± 0.02
$q\overline{q}$	0.28 ± 0.04
two-photon	0.36 ± 0.04
cosmic rays	0.01 ± 0.00
$f_{\rm bkg}$	1.42 ± 0.08

probabilities, which is not perfectly reproduced by the Monte Carlo, especially in the low polar angle regions of the detector. These were measured on data, using selected samples of electrons and muons. The errors on these measurements are the main systematic contribution to the estimates of the Bhabha and $\mu^+\mu^-$ background sources.

The error on the total background contamination translates into a systematic error on the $\tau^+\tau^-$ cross section of $\sim 0.8 \times 10^{-3}$. The bulk of the $\sqrt{s}$ dependence of the Bhabha, hadronic and dimuon background is taken into account automatically by the normalisation to the data. The remaining dependence is taken into account with the Monte Carlo. For two-photon processes a constant cross section is assumed over the $\sqrt{s}$ range considered.

Efficiency

The efficiency $\varepsilon_{\rm sel}$ of the selection cuts is obtained from the data using a sample of artificial $\tau^+\tau^-$ events. A tight tau selection, based on the information of one hemisphere, is designed to select on the opposite side an almost unbiased sample of tau hemispheres. The selected hemispheres are then paired to form artificial $\tau^+\tau^-$ events from which the efficiency is determined. At the peak, $\varepsilon_{\rm sel}$ is measured to be $\sim 94\%$.

This procedure introduces two systematic biases. The first arises from the loss of correlation between the hemispheres and from the angular dependence of the tagging efficiency. The second results from a background arising mainly from residual hadronic Z decays. These effects are taken into account by applying a correction estimated by Monte Carlo which induces a systematic uncertainty on the selection efficiency of 0.8×10^{-3}.

The $\sqrt{s}$ dependence of the selection efficiency is studied with simulated events. A small dependence (<1.6%) is found, arising from the variation of the hemisphere invariant mass distribution with $\sqrt{s}$ due to the different amounts of QED radiation. The size of the effect is checked with data using artificial tau pairs, and found to be in agreement with the Monte Carlo prediction. A systematic error of 20% of the correction was added in quadrature to the Monte Carlo statistical error.

Finally, as mentioned in Section 10.3, a small correction $\delta\sigma_{\tau\tau}^{\tau\tau\rm V}$ is applied to account for the different selection efficiency for events of the $\tau^+\tau^-V$ topology. The correction is 2.04 pb at the peak with a slight dependence on $\sqrt{s}$.

Table 15: Exclusive $\tau^+\tau^-$ selection: breakdown of final systematic uncertainties (in %) on the cross section measurement with the 1994 data set. Component A is common to all data points while component B is uncorrelated between data sets corresponding to different years of data taking.

Source	A	B	A⊕B
Acceptance	0.03	0.04	0.05
Efficiency			
Preselection cuts	0.05	0.04	0.07
$q\overline{q}$ cuts	0.06	0.09	0.11
Bhabha cuts	0.03	0.04	0.05
Dimuon cuts	0.03	0.03	0.05
Total Efficiency	0.08	0.11	0.14
Background			
$\gamma\gamma$	0.04	-	0.04
$q\overline{q}$	0.04	-	0.04
Bhabha	0.05	0.01	0.05
Dimuon	0.02	0.01	0.02
Total background	0.07	0.01	0.08
MC statistics	-	0.07	0.07
Total	0.12	0.13	0.18

Total systematic error

The total systematic uncertainty on the cross section at the peak for the 1994 data sets is 0.18%. The breakdown into the different sources is given in Table 15. To preserve sensitivity to possible variations of the detector performance with time, the above-mentioned systematic checks were performed separately for each year of data taking using the data collected at the peak. The sources of systematic uncertainty which are related to the Monte Carlo simulation are combined to give a smaller but fully correlated error (part A in the table). The remaining component (B), uncorrelated between data sets corresponding to different years of data taking, is dominated by the statistics of the sample of artificial events used to measure the efficiency.

The additional errors affecting off-peak points due to the $\sqrt{s}$ dependence of the acceptance and selection efficiencies are considered to be fully correlated.

The correlation coefficients between systematic errors assigned to peak points corresponding to different years of data taking range between 17% and 47%; for data taken at different centre-of-mass energies in the same year these coefficients are of the order of 80%.

10.4.3 Exclusive electron cross section measurement

The selection of wide-angle Bhabha events is based on kinematic cuts and requires tracks with high momenta and large energy deposition in ECAL. Since the event topologies are rather clean, particle identification is only used for event rejection.

Kinematic selection

First, the preselection conditions are tightened by retaining those events in which between two and six good tracks with $|d_0| < 2\,\mathrm{cm}$ and $|z_0| < 5\,\mathrm{cm}$ are selected. Then, in order to reject $\mu^+\mu^-$ and $\tau^+\tau^-$ final states, cuts are applied to the momenta of the two leading tracks in the event and to the associated shower energies measured in the ECAL. The possible loss of electromagnetic energy due to the radiation of a photon is corrected for, as is the energy which escapes through cracks in the ECAL but is detected by the HCAL.

The correction algorithm for the inclusion of photon or HCAL energy works as follows. Assuming a photon was radiated from the second highest momentum final state track, the expected position of the photon is $(\theta, \phi) = (\theta_2, \phi_1 \pm \pi)$, where the indices refer to the highest and second highest momentum track. The energy of the most energetic ECAL cluster not associated to a track is added, if its position matches the expected photon position within 20° in polar and azimuthal angles. The HCAL energy associated with either of the most energetic tracks is added only in the case of two-track events, in order to avoid enriching the background from $\tau^+\tau^-$ events.

The selection requires the sum of the momenta of the two selected tracks to exceed $0.05\sqrt{s}$, the sum of the track-associated ECAL energies to exceed $0.20\sqrt{s}$ and the sum of the momenta plus the sum of the energies including all corrections to be larger than $1.20\sqrt{s}$, the last being the most stringent cut. These cut values are optimised by studying Monte Carlo distributions of the signal and the main background sources, an example of which is given in Fig. 11. In order to remove radiative muon pairs further, an event is rejected if both tracks are identified as muons [6].

Acceptance

As described in Section 9.2, the analysis is performed inside an acceptance defined by $-0.9 \leq \cos\theta^* \leq +0.7$ and $\eta \leq 20^\circ$. In a small number of events (0.6%) both leading tracks have the same charge as a consequence of poorly measured tracks or photon conversions. In such events, the charge sign of the highest momentum track is used to define the positive and negative lepton in the calculation of $\cos\theta^*$. In those cases where the highest momentum track has a large momentum error ($\delta p/p > 0.5$) the charge sign of the second highest momentum track is used. Since the angular distribution of Bhabha events is very asymmetric due to the t channel, a wrong sign assignment may introduce a systematic error on the acceptance. The rate of same-sign events is measured to be approximately 30% higher in the data than in Monte Carlo. A rescaling factor is therefore applied to the Monte Carlo to accommodate this difference, leading to a correction on the acceptance of 1.1×10^{-4}, derived from the number of events where the positive and negative leptons are incorrectly assigned.

Efficiency and Background

The efficiency $\varepsilon_{\mathrm{sel}}$ of the selection within the acceptance is evaluated with the UNIBAB Monte Carlo. It is found to be essentially constant as a function of beam energy at a value of about 98.9%. The major sources of inefficiency are the charged track requirements ($\sim$0.4%), the $\Sigma(E+p)$ cut ($\sim$0.6%) and the ΣE cut ($\sim$0.1%).

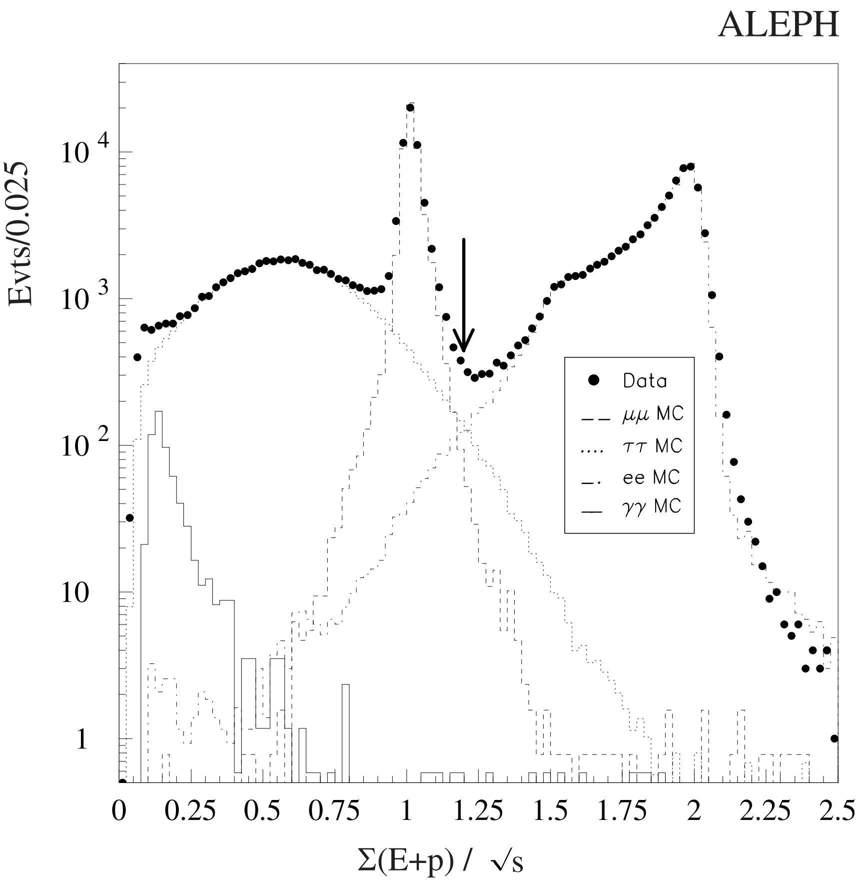

Figure 11: Exclusive e^+e^- selection: distribution of the sum of energy and momentum of lepton pair events, normalised to the centre-of-mass energy, for data and Monte Carlo before muon identification cuts.

To determine the contamination from background events a number of Monte Carlo samples were analysed with the selection criteria outlined above. In the case of $\mu^+\mu^-$, $\gamma\gamma$ and $q\overline{q}$ events the background contamination is negligible ($< 7 \times 10^{-5}$ for $q\overline{q}$, $< 4 \times 10^{-5}$ for $\gamma\gamma$ and $< 1 \times 10^{-5}$ for $\mu^+\mu^-$).

The only channel that contributes at a non-negligible level is the $\tau^+\tau^-$ final state. The Monte Carlo samples used to evaluate the tau contamination were corrected by re-calibrating the hadronic part of the energy deposited in the ECAL, i.e., that energy that is not associated to photons. This correction is a function of track momentum, polar angle and hadronic energy deposited in the ECAL. The magnitude of the correction is only appreciable at large $|\cos\theta|$, where it contributes typically 20% of the energy released in the ECAL by the track. Figure 12 shows the ratio of the energy deposited in the ECAL and the momentum of the hadron for π mesons originating from tau decays a) before and b) after this correction. The $\tau^+\tau^-$ background contamination is approximately 1.3% of the total s channel signal at the peak and shows little variation with centre-of-mass energy.

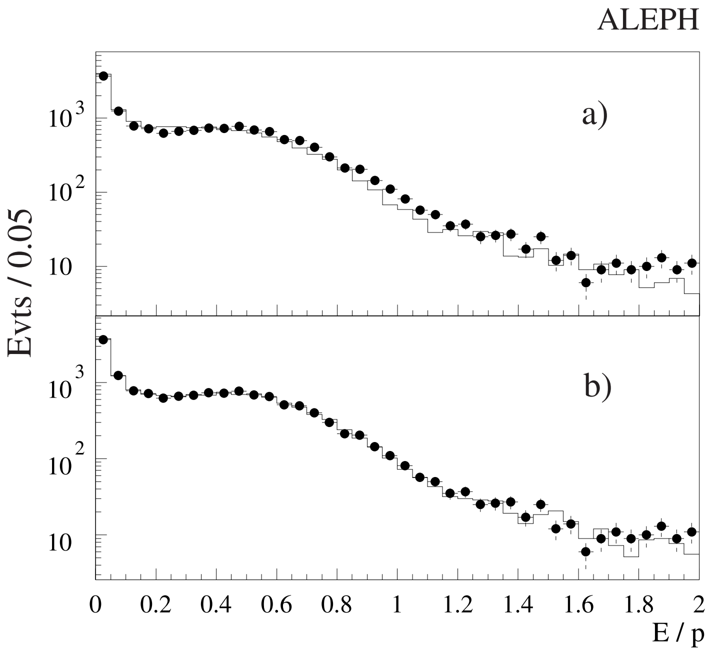

Figure 12: Exclusive e^+e^- selection: energy deposited by topologically selected pions in the ECAL divided by the hadron's momentum, a) before energy correction and b) after energy correction. Points represent the data, and the histogram is the Monte Carlo.

Systematic uncertainties

To evaluate the systematic uncertainty associated with the selection procedure, comparisons were made between Monte Carlo and data for the individually measured quantities that enter into the selection. In the Monte Carlo each quantity is smeared and shifted according to the difference between Monte Carlo and data plus one statistical standard deviation. The selection is then re-applied and the net impact on the final cross sections is measured. This exercise is repeated with data sets from all years and at all centre-of-mass energies. No significant difference between years and energies is observed, and consequently one systematic error is assumed for all data sets. In the case of the signal efficiency the uncertainty is 0.05% for the $\Sigma(E+p)$ cut and 0.02% for the ΣE cut. For the tau background the values are 0.07% for the $\Sigma(E+p)$ cut and 0.02% for the ΣE cut. In both cases the systematic error due to the Σp cut is completely negligible. Since these errors are evaluated for the entire data sample, full correlation is assumed between data points.

The hadronic energy correction is studied for systematic effects by varying the magnitude of the correction according to the statistical accuracy by which the correction factors are determined, i.e., 7.5% in the ECAL barrel and 9.5% in the ECAL endcaps. The variations are fully simulated and the net number of events gained or lost through this change results in a systematic uncertainty of typically 0.02%. Because the Monte Carlo samples are available for each energy point, this error is taken to be fully correlated between like energy points only.

Table 16: Exclusive e^+e^- selection: summary of the relative systematic errors (in %) for the electron cross section measurement for the 1994 peak data point.

Source	$\Delta\sigma/\sigma$ (%)
Acceptance	0.06
ΣE cut	0.02
$\Sigma(E+p)$ cut	0.05
$\tau^+\tau^-$ background	0.08
t channel subtraction	0.11
Hadronic energy correction	0.02
MC statistics	0.05
Total	0.17

Systematic errors due to the t channel subtraction are discussed in Section 9.3. This source of systematic error is the largest one, particularly for energies below the peak. The corrections $\delta\sigma_{\mathrm{ee}}^{\mathrm{eeV}}$ applied to the Bhabha cross sections (Section 10.3) vary slightly with centre-of-mass energy, reaching a maximum of 0.32 pb at the peak.

The systematic uncertainties for the different sources are listed in Table 16. The correlations between systematic errors for data samples in the same year are of the order of 80–90%. For data samples taken at equivalent centre-of-mass energies but in different years the correlation coefficients vary between 65 and 75% and are mainly due to the t channel subtraction.

10.4.4 Correlations between exclusive cross section measurements

In addition to the correlations between different data sets induced, within each lepton species, by the common systematic uncertainties discussed in the previous sections, there exist interspecies correlations of a statistical and systematic nature.

The statistical correlations arise from events which are in common between the selected samples. This event overlap is found to be non-negligible only between electrons and taus ($\sim$ 1%). The largest contribution to the correlations induced by systematic uncertainties arises from the errors assigned to the acceptance corrections (discussed in Section 10.2) which were evaluated in the same way for all selections and are therefore treated as fully correlated. Independent methods were used to evaluate the systematic uncertainties due to selection efficiency and background determination. The corresponding correlations are therefore expected to be small and are neglected.

The correlations were taken into account in the fitting procedure described in Section 13.2. Their combined effect is approximately 2% of the total error in the largest case (for the 1994 data sets).

10.5 Global analysis

In this section a new analysis based on a global selection of the dilepton sample is described. The aim is to optimise the measurement of R_ℓ by reducing the uncertainties and correlations arising from the flavour separation. The distinctive feature of this approach is the complete reconstruction and identification of both hemispheres of the dilepton candidates. This is then used to reject background and obtain a pure sample of dilepton events. Once this sample is obtained, flavour separation is performed, each event being allocated to one of the three flavours. This separation is needed in order to identify Bhabha events from which the t channel contribution must be subtracted.

First the preselection described in Section 9.1 is applied. Next, charged and neutral objects are defined, based on the reconstructed tracks of charged particles as well as electromagnetic and hadronic clusters; events with fewer than two objects are rejected. The event is then divided into hemispheres by the plane perpendicular to the thrust axis, thus defining two jets. Events with fewer than one good track per jet are rejected.

10.5.1 Particle identification and hemisphere classification

For both hemispheres of the dilepton candidates the charged and neutral particles are identified using the procedure described in Section 3. The identification is performed in two steps: first, electrons are identified and a search for converted photons is performed, then charged tracks not associated to a converted photon are identified. Charged tracks pointing to ECAL cracks are not identified. Charged tracks are therefore classified as electrons, muons, hadrons, or *unknown*.

Hemispheres are classified according to the number and nature of their particles. Four types of hemispheres are defined: electron (e), muon (μ), hadronic ($m\mathrm{h}+n\pi^0$) with or without additional photons, and unknown (u). In addition, hadronic hemispheres are classified according to the number of charged hadrons. For dilepton events the number of charged particles (i.e., prongs) in a hemisphere is necessarily odd; therefore if an even number of tracks is reconstructed, it is assumed that one track was lost. If a hemisphere contains an identified electron or muon accompanied by hadrons (or unknown tracks), it is classified as hadronic. This classification is used throughout the analysis, for background subtraction as well as for flavour separation. As an illustration, Fig. 13 shows the invariant mass distribution of hemispheres classified as hadronic in the dilepton data sample. The contribution of $\tau \to \rho\nu_\tau$ and $\tau \to \mathrm{a}_1\nu_\tau$ decays can be clearly identified.

10.5.2 Acceptance

The centre-of-mass scattering angle θ^* and the acollinearity are calculated as described in Section 9.1 and the standard acceptance definition is used (Section 9.2).

The polar angles of the two outgoing leptons are determined according to the hemisphere

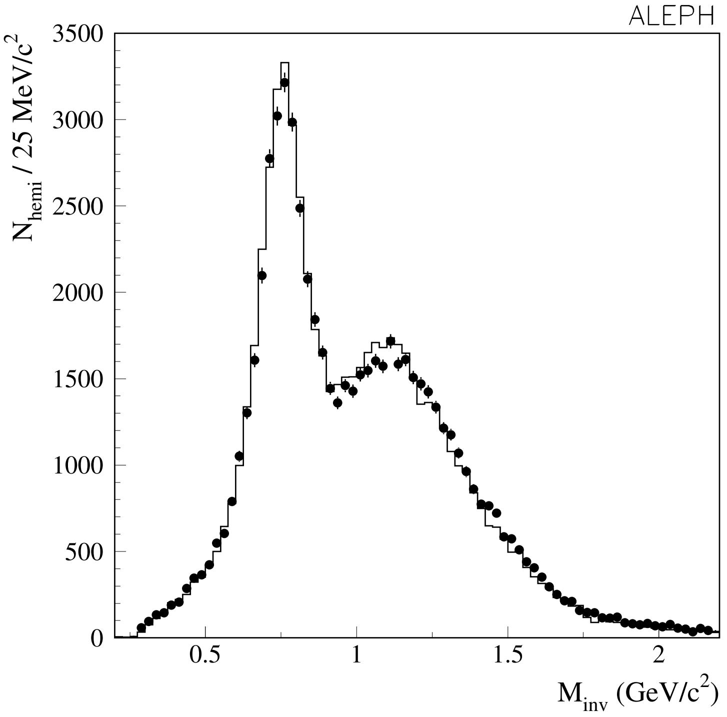

Figure 13: Global selection: invariant mass of hadronic hemispheres classified as mh+$n\pi^0$ with $m+n \geq 2$. The points represent the data, and the histogram the $\tau^+\tau^-$ Monte Carlo.

type. For hemispheres classified as electron, muon, one-prong hadronic with not more than one π^0 or unknown with not more than one π^0, the direction of the outgoing lepton is taken as the direction of the momentum of the leading track. For all other hemispheres the direction of the jet momentum is taken. The charge of the outgoing lepton is the charge of the leading track or that of the jet. If the jet has zero charge, the other hemisphere is used to assign the charge. Ambiguous cases where both hemispheres have the same charge are resolved using the sign of the track with the smallest $|d_0|$ value in the one-prong/one-prong case, the sign of the track rather than that of the jet in the one-prong/3-prong case and finally, the sign of the leading track of a jet in the 3-prong/3-prong case.

In the Monte Carlo simulation of the electron channel the wrong sign assignment introduces a variation of the acceptance of $(0.024 \pm 0.003)\%$. Data and Monte Carlo distributions for events with two like-sign hemispheres are compared. The shapes of the distributions are the same, however a rescaling factor of 1.6 must be applied to the Monte Carlo. This leads to a correction of $(0.015 \pm 0.003)\%$ on the acceptance.

Systematic errors associated with the preselection and with the acceptance cuts are described in Section 10.2. Table 17 gives these uncertainties in % of the dilepton cross sections for data taken in 1994.

10.5.3 Dilepton selection

A number of kinematic variables are defined, which are used for background subtraction or flavour separation.

For each hemisphere the following variables are defined:

- p denotes the momentum of the most energetic charged particle.
- E is the electromagnetic energy associated to this particle, measured in ECAL. If the particle points to an ECAL crack and if an HCAL cluster is associated to it, the energy of the corresponding HCAL cluster is added.
- E_γ is the energy of the most energetic photon (converted or not) contained inside a cone of 20° opening around this track.
- $E_{\mathrm{hem}} = E + E_\gamma$.
- M_{inv} denotes the invariant mass of the hemisphere.
- θ_{op}, the opening angle of a jet, is defined as the largest of the angles between any two charged particles of a jet.

The following variables are defined for each event:

- E_{tot} is the sum of the energies of all charged particles, π^0s and single photons.
- Δp_{t} is the difference in transverse momentum between the most energetic charged particles of each hemisphere.

Rejection of $\gamma\gamma$ background

The cut in acollinearity eliminates a large fraction of $\gamma\gamma$ events. The remaining background is estimated to be of $\sim$ 0.10 nb. To further reduce it, cuts are applied in the plane of total energy E_{tot} versus the transverse momentum difference Δp_{t}. If both hemispheres of the event are classified as e or μ the cut is $E_{\mathrm{tot}} + 10\Delta p_{\mathrm{t}} > 0.44\sqrt{s}$, otherwise it is $E_{\mathrm{tot}} > 0.14\sqrt{s}$ or $\Delta p_{\mathrm{t}} > 0.07 E_{\mathrm{beam}}$. The tighter cut in the former case reduces the dominant background arising from $\gamma\gamma \to \mathrm{e}^+\mathrm{e}^-$and $\gamma\gamma \to \mu^+\mu^-$events. This leaves a $\gamma\gamma$ background of (3.2 ± 0.2) pb as estimated from Monte Carlo, which represents $(0.26 \pm 0.02)\%$ of the $\tau^+\tau^-$ events inside the acceptance at $\sqrt{s} = M_{\mathrm{Z}}$. The resulting inefficiency for the $\tau^+\tau^-$ channel is $(1.53 \pm 0.02)\%$ inside the acceptance. It is a few 10^{-5} for the $\mu^+\mu^-$ events and is neglected in the following. For the Bhabha channel the inefficiency is $(0.042 \pm 0.003)\%$ for $|\cos\theta^*| < 0.9$ and $(0.017 \pm 0.003)\%$ in the interval $-0.9 < \cos\theta^* < 0.7$.

Rejection of hadronic background

Hadronic Z decays are characterised by a large number of objects, large jet opening angles and large hemisphere invariant masses.

For events with the one-prong/one-prong topology the $q\overline{q}$ background is very low. Hadronic events with such a low multiplicity are in general close to the acceptance limit, their total energy is small, and most of them are rejected by the cuts against $\gamma\gamma$ events. The contribution of this background is of the order of 0.3 pb at $\sqrt{s} = M_Z$ and no further attempt is made to remove it.

As explained in Section 10.3, four-fermion events of the $\ell^+\ell^-$V type are included in the dilepton sample. These events tend to have large jet opening angles and could therefore be rejected as $q\overline{q}$ background. In order to increase the efficiency for $\ell^+\ell^-$V final states, no cuts against $q\overline{q}$ are applied to events with fewer than five good tracks if at least one of the two following conditions is satisfied

- both hemispheres are classified as electron or muon
- at least one hemisphere is clearly leptonic, i.e., it is classified as electron and the leading track momentum is in excess of $0.55E_{\mathrm{beam}}$, as muon with a leading track momentum in excess of $0.77E_{\mathrm{beam}}$, or as hadronic one-prong (with at most one π^0) with $|\cos\theta| < 0.8$ and an invariant mass between 0.5 GeV/c^2 and 1.0 GeV/c^2.

The remaining sample, on which cuts against hadronic events are applied, contains 23% of the $\tau^+\tau^-$ events, less than 0.02% of the $\mu^+\mu^-$ events and less than 0.05% of the e^+e^- events.

Further rejection is based on likelihood estimators built for each hemisphere using Monte Carlo reference distributions. Different reference distributions are used for the barrel and endcap regions. For one-prong hemispheres the invariant mass and the number of reconstructed charged and neutral tracks are used to build the estimator; for hemispheres with three or more prongs the jet opening angle θ_{op} is added.

For each hemisphere i the normalised τ identification estimator is computed as $\mathcal{E}_{\tau,i} = e_\tau/(e_\tau + e_{\mathrm{had}})$, where e_τ and e_{had} are the values of the τ and hadronic estimators for the corresponding topology of the hemisphere [39]. For each event the normalised estimator is then given by $\mathcal{E}_{\tau^+\tau^-} = \mathcal{E}_{\tau,1} \times \mathcal{E}_{\tau,2}$. Figure 14 shows the distribution of $\mathcal{E}_{\tau^+\tau^-}$ in one-prong/three-prong events for $\tau^+\tau^-$ and $q\overline{q}$ Monte Carlo events and for data. The plot contains only those events on which cuts against $q\overline{q}$ are applied. The same figure also shows the distribution for three-prong/three-prong events. One-prong/three-prong events are rejected if $\mathcal{E}_{\tau^+\tau^-} < 0.04$ and three-prong/three-prong events are rejected if $\mathcal{E}_{\tau^+\tau^-} < 0.3$.

In order to avoid a statistical bias, Monte Carlo samples different from those used to build the estimators were used to measure the inefficiency and the background. The inefficiencies obtained from Monte Carlo are $(0.97 \pm 0.02)\%$ for $\tau^+\tau^-$, $(0.009 \pm 0.003)\%$ for $\mu^+\mu^-$ and $(0.002 \pm 0.001)\%$ for e^+e^- events. The remaining $q\overline{q}$ background is estimated to represent $(0.32 \pm 0.02)\%$ of the $\tau^+\tau^-$ events inside the acceptance.

The correction applied to the leptonic cross sections to take into account $\ell^+\ell^-$V events (Section 10.3) varies from 0.51 pb in the case of $\mu^+\mu^-$ V events, to 1.57 pb in the case of $\tau^+\tau^-$V events.

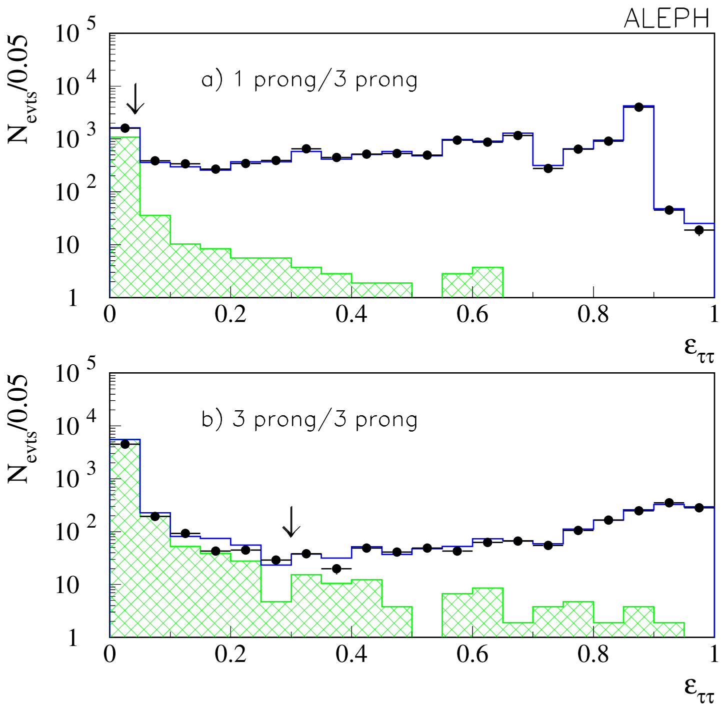

Figure 14: Global selection: distribution of the normalised estimator $\mathcal{E}_{\tau^+\tau^-}$ in (a) one-prong/three-prong events and (b) three-prong/three-prong events. The points represent the data, the open histogram the $\tau^+\tau^-$ Monte Carlo and the hatched histogram the $q\overline{q}$ Monte Carlo. The arrows indicate the position of the cuts.

The $\gamma\gamma$ and $q\overline{q}$ backgrounds as well as the resulting inefficiencies quoted in this section are estimated using Monte Carlo simulations and the errors quoted represent only the Monte Carlo statistics. Systematic uncertainties will be described in the following section.

Rejection of residual background

Cosmic-ray events occur randomly in time and space. For cosmic events which cross the detector during a beam crossing the correlation between the d_0 values of the leading tracks in the two hemispheres is used. Asynchronous events are rejected by the requirement that the total number of hits in the ITC be at least one. This cut also rejects $e^+e^- \rightarrow \gamma\gamma$ events in which the two photons converted after the ITC. Both the inefficiency introduced by this rejection and the remaining background are of the order of a few 10^{-5}.

10.5.4 Systematic errors arising from the dilepton selection

In this section the methods used to estimate systematic errors on the efficiencies and backgrounds are described.

Systematic errors on the efficiency

For e^+e^- and $\mu^+\mu^-$ final states the inefficiencies due to $\gamma\gamma$ rejection cuts are very small and therefore the agreement between data and Monte Carlo is difficult to check. Data and Monte Carlo predictions have been compared for high values of E_{tot}. No disagreement is found, but the statistical error of this test represents 100% of the predicted inefficiency. The final inefficiency inside the acceptance is $(0.017 \pm 0.017)\%$ for the e^+e^- channel and of the order of 10^{-5} for the $\mu^+\mu^-$ channel. The latter is safely neglected.

For the $\tau^+\tau^-$ channel the agreement between data and Monte Carlo is checked in a region of the phase space where the $\gamma\gamma$ contribution is low. Events in which both hemispheres are classified as electron or muon are considered if the acollinearity η is less than 10° and $E_{\text{tot}} + 10\Delta p_{\text{t}}$ is between $0.22\sqrt{s}$ and $0.44\sqrt{s}$. For all the other events it is required that E_{tot} be greater than $0.08\sqrt{s}$ and smaller than $0.14\sqrt{s}$. The remaining $\gamma\gamma$ contribution is estimated from Monte Carlo and subtracted from the data. The ratio of the number of selected events in data and Monte Carlo is consistent with unity, therefore no correction is applied to the Monte Carlo. The systematic uncertainty is derived from the statistical uncertainty on the ratio. The final inefficiency in the $\tau^+\tau^-$ channel arising from $\gamma\gamma$ rejection is $(1.54 \pm 0.06)\%$ inside the acceptance.

Since the data at all the energy points have the same behaviour and no correction is applied to the Monte Carlo, this study is performed globally and the resulting systematic error is fully correlated between energy points.

For most of the e^+e^- and $\mu^+\mu^-$ events no cuts against the hadronic background are applied. Inefficiencies are lower than 10^{-4} and the corresponding systematic errors are therefore neglected. The rejection of hadronic events mainly affects the $\tau^+\tau^-$ channel. An important reason for which $\tau^+\tau^-$ events are lost is nuclear interactions with the detector material. Such events tend to have high reconstructed invariant masses and large jet opening angles. Moreover nuclear interactions are not fully simulated in the Monte Carlo. The inefficiency was therefore estimated from the data. For this purpose $\tau^+\tau^-$ events are selected using tight selection criteria to flag tau-like hemispheres classified as electron or muon. With the sample of opposite hemispheres, artificial $\tau^+\tau^-$ events are constructed by associating two such back-to-back hemispheres and the $q\overline{q}$ selection is applied. Figure 15 shows the distribution of the normalised estimator $\mathcal{E}_{\tau^+\tau^-}$ for the data and Monte Carlo samples of artificial $\tau^+\tau^-$ events.

In order to assess the validity of this method and to correct for possible biases, two different Monte Carlo reference samples are used. On the first sample the same procedure of artificial $\tau^+\tau^-$ events is applied, on the second one the $q\overline{q}$ selection is applied directly. The final inefficiency in data is $(1.00 \pm 0.11)\%$ of the $e^+e^- \to \tau^+\tau^-$ events inside the acceptance. The error reflects the statistical uncertainty of the data and Monte Carlo artificial samples. Independent studies are performed for each year of data taking, therefore this uncertainty is uncorrelated between energy points of different years.

Systematic errors on the background

The systematic error on the $\gamma\gamma$ background is obtained by comparing data and Monte

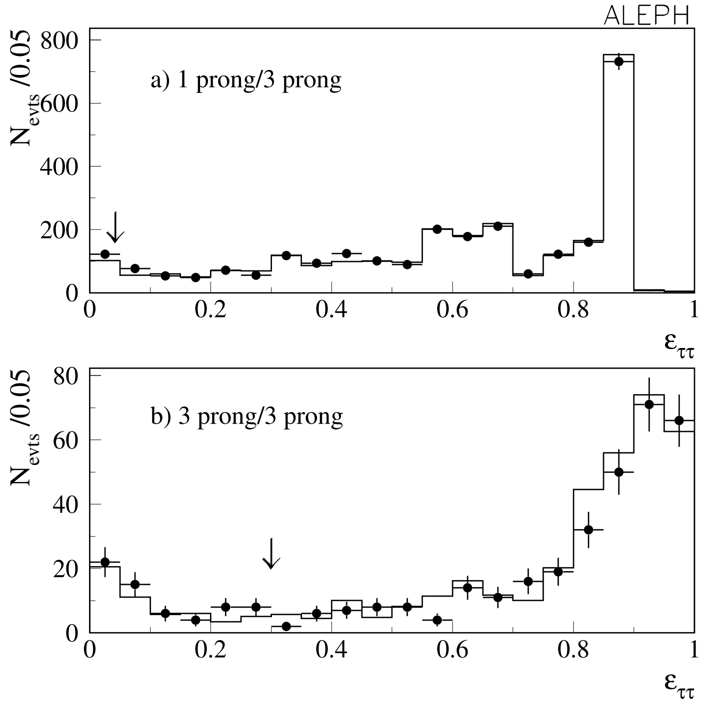

Figure 15: Global selection: distribution of the normalised estimator $\mathcal{E}_{\tau^+\tau^-}$ (a) for artificial one-prong/three-prong events and (b) three-prong/three-prong events. The points represent the data, and the histogram the $\tau^+\tau^-$ Monte Carlo. The arrows indicate the position of the cuts.

Carlo for events lying outside the acceptance cut in acollinearity ($20° < \eta < 40°$), where $\gamma\gamma$ events are dominant. The comparison is performed separately for events identified as e/e and μ/μ in order to check both the $\gamma\gamma \to e^+e^-$and $\gamma\gamma \to \mu^+\mu^-$ Monte Carlo simulations. The agreement is good for the e/e sample but a rescaling factor of 1.1 must be applied for the μ/μ events. Inside the acceptance but close to its limit ($10° < \eta < 20°$) the same behaviour is observed, however because in this case the dilepton contribution is no longer negligible the values obtained for the background outside the acceptance are used, with a systematic error corresponding to the error obtained for $10° < \eta < 20°$. A global study was performed for all energy points and the resulting $\gamma\gamma$ background is (3.1 ± 0.2) pb.

Hadronic events that survive the dilepton selection are pathological, low multiplicity events and one can expect that they are not well simulated in the Monte Carlo. As explained in Section 10.5.3, for a large fraction of the dilepton candidates no cuts against $q\overline{q}$ events are applied. The resulting background, as estimated from Monte Carlo, is very small; it represents only 0.05% of the $\tau^+\tau^-$ sample. The agreement between data and Monte Carlo has been verified on events with a small value of the normalised estimator $\mathcal{E}_{\tau^+\tau^-}$. Although no disagreement is found, the statistical significance of the test is low and therefore the Monte Carlo prediction is used with a 50% systematic uncertainty assigned as systematic uncertainty.

For the remaining sample, the systematic error is estimated by comparing the distribution of the normalised estimator $\mathcal{E}_{\tau^+\tau^-}$ in data and Monte Carlo independently for events with

Table 17: Global selection: systematic uncertainties in % of dilepton cross sections for peak 1994 data. Correlations between lepton flavours are taken into account in the $\ell^+\ell^-$ column.

	e^+e^-	$\mu^+\mu^-$	$\tau^+\tau^-$	$\ell^+\ell^-$
Global selection				
Preselection and acceptance	0.06	0.04	0.04	0.05
$\gamma\gamma$ cuts (*)	0.02	-	0.05	0.02
$q\overline{q}$ cuts	-	-	0.11	0.04
$\gamma\gamma$ background (*)	-	-	0.02	-
$q\overline{q}$ background(*)	-	-	0.04	0.01
Flavour separation				
$\mu^+\mu^-/\tau^+\tau^-$	-	0.03	0.03	-
$e^+e^-/\tau^+\tau^-$ $\cos\theta^* < 0.7$	0.08	-	0.07	0.01
$e^+e^-/\tau^+\tau^-$ $\cos\theta^* \geq 0.7$	-	-	0.06	0.02
t channel subtraction				
(*)	0.11	-	-	0.04
Monte Carlo statistics				
	0.05	0.06	0.07	0.04
Total	0.16	0.08	0.19	0.09

(*) uncertainties fully correlated between energy points.

the one-prong/three-prong and three-prong/three-prong topologies. A first check is made on events which have been rejected by $q\overline{q}$ cuts in each topology. The number of events found in data and Monte Carlo agree for the one-prong/three-prong topology, but for the three-prong/three-prong events a rescaling factor of 0.8 must be applied to the $q\overline{q}$ Monte Carlo. Next, the shapes of the $\mathcal{E}_\tau$ distributions for one-prong and three-prong hemispheres are compared in data and Monte Carlo. The agreement is good at the level of a few % for one-prong hemispheres over the entire distribution of $\mathcal{E}_\tau$. It is however only at the level of 20% at high values of the estimator for three-prong hemispheres. A systematic uncertainty of 20% is therefore assigned to the background estimate in one-prong/three-prong events and 40% in the three-prong/three-prong topology. A global study has been performed on all the energy points, and the $q\overline{q}$ background at centre-of-mass energy $\sqrt{s}$ is taken to be $(3.6 \pm 0.6)\,\mathrm{pb} \times (\sigma_{q\overline{q}})(\sqrt{s})/\sigma_{q\overline{q}}(M_Z))$.

All the systematic errors described in this section are summarised in Table 17 for data taken in 1994.

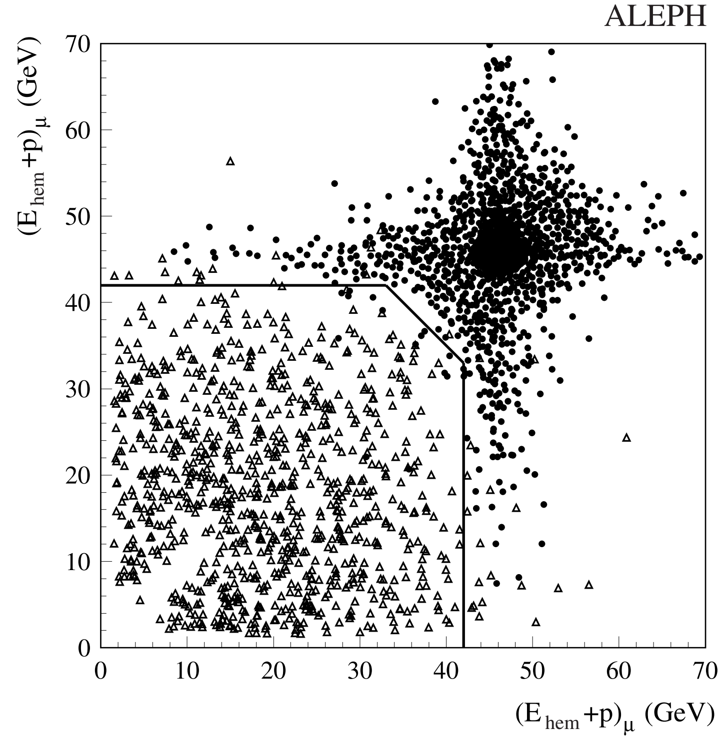

Figure 16: Global selection: $E_{\text{hem}} + p$ in hemisphere 1 versus hemisphere 2 for events identified as μ/μ. The triangles represent the $\tau^+\tau^-$ Monte Carlo, the full circles the $\mu^+\mu^-$ Monte Carlo. The lines indicate the cuts that define the $\mu^+\mu^-$ sample.

10.5.5 Flavour separation

The great majority of Bhabha events (97%) have both hemispheres classified as electron or unknown; the remaining ones consist of one electron hemisphere, the other hemisphere being one-prong hadronic. Dimuon final states are found to yield two hemispheres classified as muon (98%), or muon and one-prong hadronic. Particle identification and hemisphere classification are therefore sufficient for $\mu^+\mu^-$ and Bhabha separation and the two resulting samples are totally uncorrelated.

In order to select $\mu^+\mu^-$ and Bhabha final states it is therefore only necessary to distinguish them from $\tau^+\tau^-$ events. For this purpose, kinematic cuts are applied in the two-dimensional distribution of the sums $E_{\text{hem}} + p$ in the two hemispheres of an event (Section 10.5.1). These cuts depend on the event topology and hemisphere classification. For example, Fig. 16 shows the two-dimensional plot of the sum of the energy and momentum of each hemisphere in events identified as μ/μ. All dilepton events which are not selected as $\mu^+\mu^-$ or e^+e^- are called $\tau^+\tau^-$. Table 18 gives the fraction of Monte Carlo events attributed to each lepton flavour.

For e^+e^- and $\mu^+\mu^-$ events classified as $\tau^+\tau^-$ there are two possible sources of systematic errors in the flavour separation: the first arises from e and μ identification, and the second one from energy and momentum measurement.

The agreement between data and Monte Carlo for electron and muon identification has been checked using Bhabha and $\mu^+\mu^-$ events with one clear high momentum e or μ hemisphere. In the sample of opposite hemispheres there are fewer muons and electrons misidentified as hadrons in the Monte Carlo than in the data, and a correction factor of 1.30 ± 0.04 must be applied. This leads to a systematic uncertainty of 0.02% for the $\mu^+\mu^-$ channel and of 0.03% for the e^+e^- channel.

Systematic uncertainties on the energy and momentum measurements arise from imperfect simulation of initial and final state radiation, as well as from the not optimal modelling of the energy measurement in the electromagnetic calorimeter. These effects are estimated by comparing data and Monte Carlo in appropriate regions of the phase space. The most important contribution to the systematic error is due to the imperfect modelling of the energy measurement in the electromagnetic calorimeter. This is shown in Fig. 17 where the distribution of the sum of energy and momentum for Bhabha-like hemispheres is given for data and Monte Carlo. The quality of the agreement in the region of low values of $E_{\mathrm{hem}}+p$ (between 40 and 60 GeV) leads to a systematic uncertainty of 0.01% and 0.03% for the $\mu^+\mu^-$ and e^+e^- channels, respectively.

An additional contribution to the systematic error comes from $\tau^+\tau^-$ events misidentified as e^+e^- or $\mu^+\mu^-$. This is estimated with data, using the method of artificial events described in Section 10.5.4. For this study τ-like hemispheres are selected in the one-prong hadronic sample, in order to reduce background from e^+e^- and $\mu^+\mu^-$. The systematic error reflects the statistics of the data and Monte Carlo samples. In the 1994 data, $(0.92 \pm 0.07)\%$ of the $\tau^+\tau^-$ events are identified as e^+e^- and $(0.21 \pm 0.02)\%$ as $\mu^+\mu^-$.

In the case of Bhabha events the systematic errors are different in the regions $-0.9 < \cos\theta^* < 0.7$ and $\cos\theta^* > 0.7$. In the first case the error affects both the Bhabha and $\tau^+\tau^-$ channels, whereas in the second case only the $\tau^+\tau^-$ channel is concerned.

The systematic uncertainties arising from flavour separation are estimated independently

Table 18: Global selection: fraction of Monte Carlo events attributed to each lepton flavour in %. The columns correspond to the generated flavours and the rows to the reconstructed ones. The errors are due to the statistics of the Monte Carlo samples.

Flavour	$\mu^+\mu^-$	$\tau^+\tau^-$	e^+e^- ($\cos\theta^* < 0.7$)	e^+e^- ($\cos\theta^* \geq 0.7$)
$\mu^+\mu^-$	99.842 ± 0.006	0.172 ± 0.007	< 0.001	< 0.001
$\tau^+\tau^-$	0.158 ± 0.006	98.917 ± 0.017	0.587 ± 0.017	0.670 ± 0.021
e^+e^- $\cos\theta^* < 0.7$	< 0.001	0.671 ± 0.013	99.413 ± 0.017	-
e^+e^- $\cos\theta^* \geq 0.7$	< 0.001	0.240 ± 0.008	-	99.330 ± 0.021

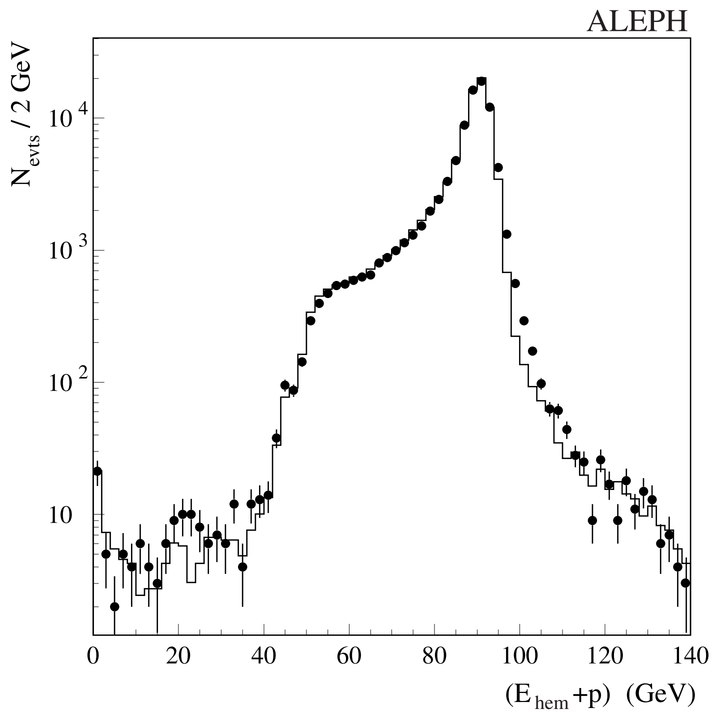

Figure 17: Global selection: $E_{\rm hem} + p$ for Bhabha-like hemispheres in data (points) and Bhabha Monte Carlo (histogram).

for each year of data taking. Table 17 gives the values of these errors for data taken in 1994.

The subtraction of the t channel contribution to the Bhabha cross section and the associated systematic errors are described in Section 9.3.

10.6 Combination of exclusive and global cross section measurements

The two sets of analyses presented in the previous sections have both high efficiency and low contamination. The overlap between the selected samples, which is given in Table 19, is therefore large, especially for Bhabha and muon events. The systematic uncertainties of the analyses are summarised for the 1994 data in Table 20. For $\mu^+\mu^-$ the difference in the acceptance comes from the fact that for the exclusive analysis the acollinearity cut is included in the background rejection cuts; moreover, the error on the background contamination contains only the Monte Carlo statistics, the uncertainty from muon identification being included in the efficiency error.

As can be seen in Table 20, the performance of the two sets of analyses are very similar, with a slightly higher efficiency for the global one. In fact, the main difference arises from the correlation matrices, the evaluation of which was discussed in the previous sections.

Table 19: Comparison of dilepton analyses: statistical overlap between 1994 datasets; values are expressed in % of the *OR* of the two samples.

	Common	Exclusive only	Global only
$\mu^+\mu^-$	97.7	1.1	1.2
$\tau^+\tau^-$	90.6	3.3	6.1
e^+e^-	97.7	1.5	0.8

Table 20: Comparison of the dilepton analyses: acceptance, efficiency, background and associated systematic uncertainties for the two sets of analyses; values (in %) refer to 1994 data.

$\mu^+\mu^-$		
	Exclusive	Global
Acceptance	85.35 ± 0.05	84.51 ± 0.06
Efficiency	98.49 ± 0.05	99.79 ± 0.02
Background	0.27 ± 0.01	0.20 ± 0.03

$\tau^+\tau^-$		
	Exclusive	Global
Acceptance	82.56 ± 0.07	82.82 ± 0.08
Efficiency	94.51 ± 0.14	96.41 ± 0.16
Background	1.42 ± 0.08	1.91 ± 0.08

e^+e^-		
	Exclusive	Global
Acceptance	72.10 ± 0.08	72.04 ± 0.06
Efficiency	99.24 ± 0.06	99.25 ± 0.08
Background	1.20 ± 0.08	0.81 ± 0.07
t–channel	0.11	0.11

The agreement between the analyses can be judged by taking the ratios of cross sections and comparing them with the statistical fluctuation allowed by the uncommon events. These ratios are shown in Fig. 18. In general the agreement is good. In the Bhabha channel a discrepancy is observed for the 1991 data points which is caused by the different corrections applied for the $\tau^+\tau^-$ contamination. This difference is covered by the associated systematic uncertainty, which is not included in the plot.

The results of the exclusive and global analyses are combined with *a priori* weights of 50% in order to minimise the impact of the lack of detailed knowledge of the correlation of systematic errors. Statistical correlations between the analyses, although greater than 95%, are taken into account explicitly. Systematic errors are treated as fully correlated; the possibility of reducing the systematic errors in the average by disentangling the uncorrelated parts is therefore not exploited. The combined cross sections are reported in Table 21 of Section 12. As a cross-check, the results were also combined at the level of the fit results, as described in Section 13.2.

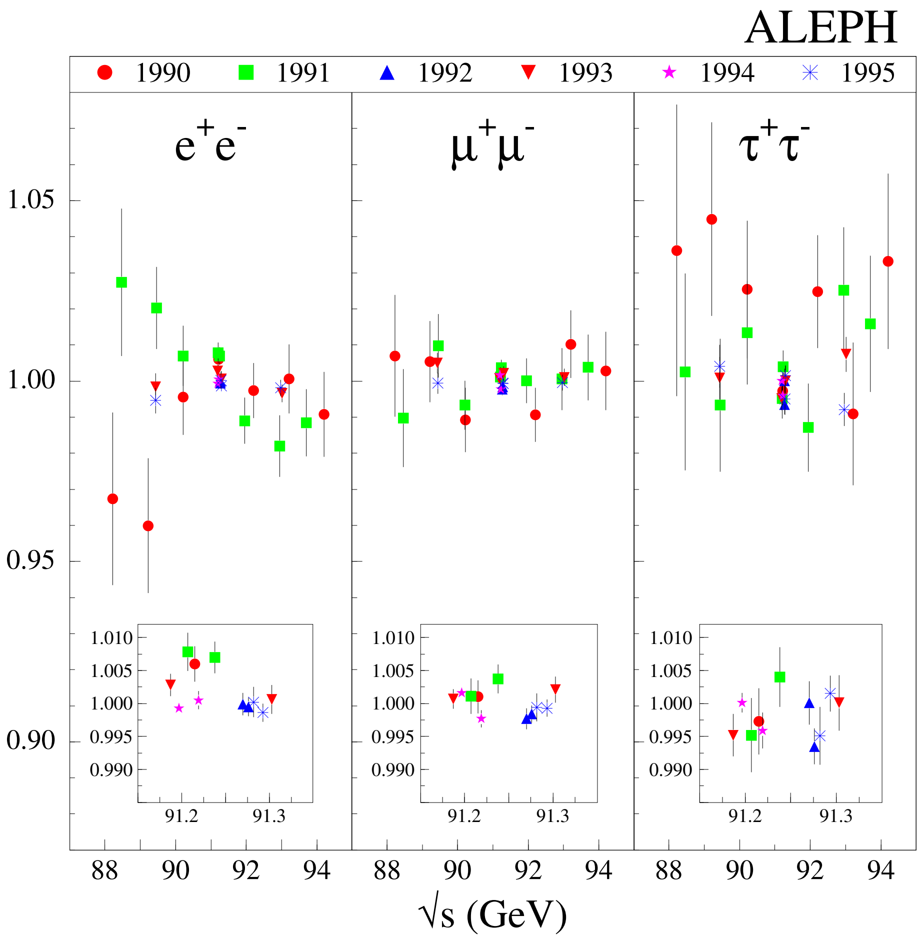

Figure 18: Comparison of dilepton analyses: ratio of exclusive to global cross section for the three lepton species. Only errors from uncommon statistics are shown.

11 Measurement of the lepton forward-backward asymmetry

For s channel Z and γ exchange, the differential cross section for the reaction $e^+e^- \to \ell^+\ell^-$ is expected to be of the form

$$\frac{d\sigma}{d\cos\theta^*} \propto \left(1+\cos^2\theta^* + \frac{8}{3}A_{\mathrm{FB}}\cos\theta^*\right) , \tag{8}$$

where θ^* is the centre-of-mass angle between the incoming electron and the outgoing negative lepton, as described in Eq. (5), and A_{FB} is the lepton forward-backward asymmetry. In the absence of initial state radiation this equation also describes the distribution in $\cos\theta$, where θ is the equivalent angle in the laboratory frame. This distribution is valid for muons and taus, while for electrons the additional contribution arising from the t channel γ exchange and the interference with the s channel diagrams must be included.

In contrast to the cross section, the measurement of the forward-backward charge asymmetry is not sensitive to the overall efficiency but to the dependence of the efficiency on $\cos\theta^*$. Around the Z mass the asymmetry varies rapidly with $\sqrt{s'}$, equivalent to the invariant mass $m_{\ell\ell}$ of the dilepton final state in the absence of final state radiation. This variation is induced by the γ-Z interference term. Acollinearity and energy cuts induce a dependence of the inefficiencies and contaminations on $m_{\ell\ell}$. Such effects, whilst marginal for the cross section estimation, will bias the asymmetry measurement and therefore require correction.

To minimise these effects, dedicated selections were designed for the muon and tau channels. They rely on the particle identification described in Section 3 and are based on loose acollinearity cuts. In addition, a maximum likelihood fit to the differential cross section removes the sensitivity to any variation of the efficiency symmetric in $\cos\theta^*$ (as discussed in Section 11.1.3). For Bhabha events, the t channel subtraction requires full knowledge of the efficiency as a function of $\cos\theta^*$, which must be estimated by Monte Carlo. Therefore, while similar analysis methods are used for the muon and tau channels, a different procedure is followed for the electron channel.

11.1 Muon and tau forward-backward asymmetry

11.1.1 Muon channel selection

Two good tracks are required and their directions are used to define the muon polar angles. The acceptance is defined by the $|\cos\theta|$ of the negative track being less than 0.9. Events with the same charge for both hemispheres are rejected. The mismeasurement of the charge, due mostly to bad reconstruction, is $(1.3 \pm 1.3) \times 10^{-5}$ and is neglected. The cosine of the acollinearity angle between the tracks is required to be larger than 0.8. The $|d_0|$ of at least one of the tracks must be smaller than 0.2 cm.

Two cases are considered:

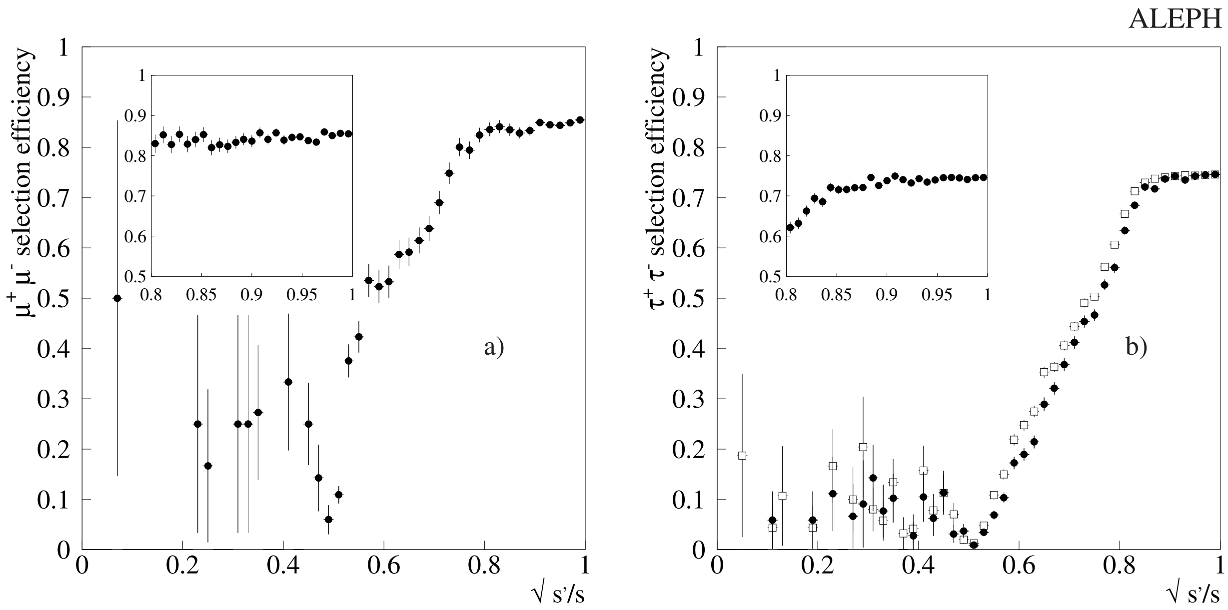

Figure 19: Overall efficiency as a function of $\sqrt{s'/s}$ for the a) muon and b) tau selections. The white squares in Fig. b) indicate the contribution of the acollinearity cut alone; to facilitate the comparison, this contribution has been normalised to have the same content in the last bin as the total efficiency. The inserts show an enlargement of the regions $0.8 < \sqrt{s'/s} < 1$.

- If the two tracks are both identified as muons, the kinematic cuts needed to remove the $\gamma\gamma$ and tau events are very loose: the missing mass squared is required to be less than 250 $(\mathrm{GeV}/c^2)^2$ or both momenta to be above $0.75E_{\mathrm{beam}}$. This identification selects 97.9% of the events, most of them being accepted through the missing mass criterion (0.16% of the events are accepted through only the momentum cut). Of the $\mathrm{e}^+\mathrm{e}^- \rightarrow \mu^+\mu^-$ events with two identified muons, only 0.08% are rejected by the kinematic cuts.

- If only one track is identified as a muon, the opposite hemisphere is required to have an energy in the ECAL not exceeding what is expected from a minimum ionising particle as well as satisfying one of the two following conditions: a missing mass squared smaller than 150 $(\mathrm{GeV}/c^2)^2$ or both momenta above $0.85E_{\mathrm{beam}}$. This additional selection increases the efficiency by 0.8%.

The overall efficiency (including angular acceptance) for the $\mathrm{Z} \rightarrow \mu^+\mu^-$ channel is measured on Monte Carlo to be 84.5%. The shape of the efficiency as a function of $m_{\ell\ell}$ estimated from a simulation based on KORALZ is shown in Fig. 19 a).

The contamination from the $\mathrm{Z} \rightarrow \tau^+\tau^-$ channel is $(4.8 \pm 0.1) \times 10^{-4}$ and from two-photon processes $(5.2 \pm 1.7) \times 10^{-4}$. Their contributions to the asymmetry are found to be negligible.

11.1.2 Tau channel selection

The sum of the charged track momenta in each hemisphere is used to define the tau polar angles. The acceptance is defined by the $|\cos\theta|$ of the negative track being less than 0.9 Events with the same charge for both hemispheres are rejected. The mis-measurement of the charge is at the level of $(3.5 \pm 0.2) \times 10^{-3}$ and its systematic impact on the asymmetry measurement is discussed in Section 11.1.4. The cosine of the acollinearity angle is required to be larger than 0.9 and the $|d_0|$ of at least one of the tracks to be smaller than 0.2 cm. The more restrictive acollinearity cut than for the muon channel is needed to reduce the $\gamma\gamma$ background.

To suppress the Bhabha background, at least one of the tracks must be identified as a pion or a muon and if only one pion (and no muon) is identified, the maximum ECAL energy measured in each of the two hemispheres is required to be less than $0.8E_{\mathrm{beam}}$. This implies that the events in which both taus decay into an electron are not used for the asymmetry measurement.

To suppress the $\mu^+\mu^-$ background, events with one muon of momentum larger than 20 GeV/c and missing mass squared smaller than 250 $(\mathrm{GeV}/c^2)^2$ are rejected.

The $\gamma\gamma \to \mu^+\mu^-$ background is reduced by cutting on the missing transverse momentum, $p_{\mathrm{t}}^{\mathrm{miss}}$. Events with $p_{\mathrm{t}}^{\mathrm{miss}}$ smaller than 1 GeV/c are rejected if one of the tracks appears as a minimum ionising particle in the ECAL, whereas events with $p_{\mathrm{t}}^{\mathrm{miss}}$ smaller than 3 GeV/c are rejected only if there are two identified muons.

To reject the $\mathrm{q\bar{q}}$ background, the cosine of the angle between any two particles, charged tracks or photons, in the same hemisphere is required to be greater than 0.92 (or 0.98, if the number of charged tracks plus photons is larger than nine); moreover, an estimator discriminating taus from hadrons, built from charge multiplicity, opening angles and track momenta [39], is used in those cases where one hemisphere has more than one charged track.

Finally the Bhabha background is suppressed by applying a cut, hereafter called the "circular cut", in the plane of the total ECAL wire energy versus the scalar sum of the momenta, requiring $\sqrt{E_{\mathrm{ECAL}}^2 + p_{\mathrm{TPC}}^2} < 0.9\sqrt{s}$.

The overall selection efficiency is 73.7%. The $\mu^+\mu^-$ contamination has been checked to present a symmetric angular distribution and its level of less than 2×10^{-3} is therefore negligible. The Bhabha background, the most dangerous source of asymmetry, is estimated from the $\mathrm{e} \to \pi$ misidentification rate measured on data to be $(3.4 \pm 2.0) \times 10^{-3}$. This level of contamination has been checked using an estimator of the likelihood for a hemisphere to be part of a Bhabha event. It is based on the particle identification probability, the track momentum and the ECAL wire energy. It finds a contamination of $(2.2 \pm 1.0) \times 10^{-3}$, a completely consistent value. All other background sources are negligible.

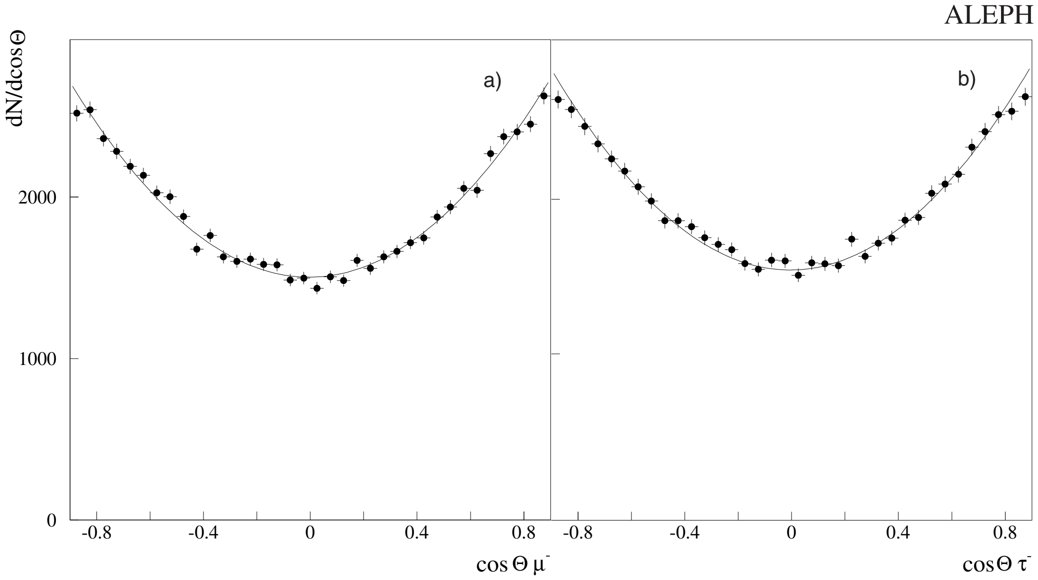

Figure 20: Angular distributions of the negative lepton at the peak energy in 1994, for muons a) and taus b). The curves are the result of the maximum likelihood fits. The loss of efficiency at large $|\cos\theta|$ comes from the angular acceptance cut.

11.1.3 Method to extract the forward-backward asymmetry

The forward-backward asymmetry $A_{\rm FB}(s)$ at each centre-of-mass energy is extracted by fitting the angular distribution not corrected for acceptance with the function given by Eq. (8), using an unbinned maximum-likelihood method. This procedure is valid as long as the acceptance is forward-backward or charge symmetric, which is true for this selection and for the detector. To be compatible with ZFITTER [40], the analytical program used to estimate the bias from the inefficiency, the $\cos\theta$ distribution of the negatively charged lepton is analysed rather than the $\cos\theta^*$ distribution. With this choice of angle, the events with initial state radiation slightly modify the measured distribution with respect to Eq. (8). This effect does not introduce a bias in the fit because the distortion induced by the boost retains the forward-backward symmetry of the initial state radiation. The measured angular distributions at the peak energy in 1994 for muon and tau events are shown in Fig. 20. The loss of efficiency at large $|\cos\theta|$ induced by the fiducial cut is also symmetric and does not bias the fit.

The dependence of the efficiency on s'/s is computed from a KORALZ Monte Carlo with full detector simulation. Using the Monte Carlo information, s' is computed as the mass squared $m_{\ell\ell}$ of the final lepton system without final state radiation. This matches the s' definition used in ZFITTER and avoids any ambiguity in the final state radiation definition. The shape of the s'/s distribution is dominated by the effect of the acollinearity cut which, at a given polar angle, corresponds to an s'/s cut, as shown in Eq. (6). This is illustrated in Fig. 19, which shows the efficiency as a function of $\sqrt{s'/s}$ including all cuts for the muon and tau channels. In the latter case the efficiency for the acollinearity cut alone is also shown.

A correction of the bias introduced by the inefficiency, calculated with ZFITTER, has been preferred to a direct use of the efficiency as a function of $\cos\theta$ obtained by Monte Carlo simulation, on the grounds that such a simulation does not include the interference between initial and final state radiation, and introduces an additional statistical uncertainty.

The correction is estimated in two ways. The first is based on the approximation that the loss of efficiency at low $\sqrt{s'/s}$ is due to the acollinearity cut; the correction is computed by introducing this cut in ZFITTER and comparing the result to that obtained without the cut. The second uses the $\sqrt{s'/s}$ efficiency distribution with the assumption that the inefficiency does not bias the asymmetry in the bin under consideration; the correction to the asymmetry is calculated as

$$\delta A_{\mathrm{FB}} = \frac{\sum \varepsilon_i \sigma_i A_i}{\sum \varepsilon_i \sigma_i} - \frac{\sum \sigma_i A_i}{\sum \sigma_i}, \tag{9}$$

where A_i is the asymmetry, σ_i the cross section and ε_i the efficiency in bin i. The corrections are small and similar for the two methods. They range for muons (taus) from -0.0083 (-0.0038) at 88 GeV to 0.0043 (0.0030) at 94 GeV. They are very close to zero (0.0003 and 0.0004, for μ and τ, respectively) at the peak. The asymmetry from ZFITTER is computed with the same maximum likelihood fit as used on the data, on cross sections computed in $\cos\theta$ bins.

The values computed with the second method are used for the corrections. The corrections for taus are smaller than those for muons even though the cut on acollinearity is tighter, due to the different amount of final state radiation.

11.1.4 Systematic uncertainties

Three sources of systematic uncertainties have been investigated, those due to the applied corrections, those due to the presence of background, and those due to possible detector asymmetries.

The first uncertainty is taken as the difference between the two ways of computing the corrections. The systematic uncertainty due to the acollinearity cut being negligible, this means that the full effect of the other cuts is taken as the systematic uncertainty. The correction has been checked by estimating the impact of the acollinearity cut on the asymmetry from Monte Carlo (KORALZ). It is found to be $(3.7 \pm 1.4) \times 10^{-4}$ at the peak, in agreement with the 2.5×10^{-4} estimated with the first method. The effect of the cuts other than the acollinearity has also been directly checked on Monte Carlo by measuring the change in asymmetry introduced by these cuts on a sample selected in acollinearity at the level of the kinematic generation. It is found to be $(2 \pm 5) \times 10^{-4}$.

The background sources are different for muons and taus. For the muon channel, the $\gamma\gamma \to \mu^+\mu^-$ background, although the dominant one, has been reduced to a negligible amount. For the tau channel the $\mathrm{e}^+\mathrm{e}^- \to \mu^+\mu^-$ contamination is negligible. Bhabha events are, by far, the dominant background to this channel. Their contribution to the asymmetry is determined by varying the circular cut described in the selection. The measurement of contamination and asymmetry for three different values of the cut gives the possibility of extrapolating the asymmetry to its value without contamination and provides an estimate, which is statistically limited, of the uncertainty. The corrections are smaller than the quoted systematic uncertainties, which are about 10% of the statistical uncertainties.

The selection eliminates almost entirely $\mu^+\mu^-$V and $\tau^+\tau^-$V events. This induces a bias on the asymmetry smaller than 10^{-4} which is included in the systematic uncertainty.

The systematic error related to the detector is subtle as it originates from a simultaneous sensitivity to both detector and charge asymmetries. Such a sensitivity could arise from events where both tracks end up in a crack between modules; this effect has been measured to be small and not to yield a bias. The mismeasurement of the charge in the tau channel is at the level of $(3.5 \pm 0.2) \times 10^{-3}$ in the data and $(2.5 \pm 0.1) \times 10^{-3}$ in the Monte Carlo, the events showing an asymmetry consistent with the full sample. Such a mismeasurement arises from badly reconstructed five-prong events, nuclear interactions or converted photons where tracks are lost because of the track selection cuts. Corrections due to charge dependent momentum distortions which depend on θ and ϕ are also applied. A variation of these corrections on the measured value of A_{FB} is negligible, as can be expected from the small impact on the signal sample of the momentum cuts. All this is summarised in an overall 5×10^{-4} uncertainty.

These systematic uncertainties are to be compared with the statistical error on A_{FB} of 0.0025.

11.2 Electron forward-backward asymmetry

11.2.1 Selection and efficiencies

The selection of Bhabha events for the asymmetry measurement is identical to that outlined in Section 10.4.3 for the Bhabha cross section with the exception of the treatment of the "same-sign events". These events, which occur at the 0.6% level, are excluded from the data for the asymmetry measurement. A comparison between data and Monte Carlo indicates that their $\cos\theta^*$ distribution is well-reproduced by the Monte Carlo.

Due to the presence of the t channel, an asymmetric angular acceptance is used. Consequently, the efficiency must be fully estimated as a function of $\cos\theta^*$.

11.2.2 Evaluation of the electron forward-backward asymmetry

The acceptance is defined by the range $[-0.9, 0.7]$ in $\cos\theta^*$ and a cut on the acollinearity ($\eta \leq 20°$). The angular acceptance is covered by 16 bins in $\cos\theta^*$. The number of events in a bin is the sum of the Bhabha events and the τ background. It can be written for a centre-of-mass energy $\sqrt{s}$ and a $\cos\theta^*$ bin i as

$$\mathrm{N}(i) = \mathrm{C}[\varepsilon_{\mathrm{ee}}(i)\varepsilon_{\mathrm{acol}}(i) + \varepsilon_{\tau\tau}(i)]\sigma_s(i) + \mathcal{L}\varepsilon_{\mathrm{ee}}(i)\sigma_t(i). \tag{10}$$

In this expression, C is an overall normalisation factor, proportional to the integrated luminosity but allowed to vary in the maximum likelihood fitting procedure; $\varepsilon_{\mathrm{ee}}(i)$ is the selection efficiency for bin i as measured from the Bhabha Monte Carlo (UNIBAB), which includes all selection cuts except the acollinearity cut; $\varepsilon_{\mathrm{acol}}(i)$ is a correction factor that varies with $\cos\theta^*$ and has a mean value of approximately 0.985; it is calculated from an s-channel-only Monte Carlo (KORALZ) and is defined as the ratio of the number of events generated in bin i with the acollinearity cut to that without the acollinearity cut; $\varepsilon_{\tau\tau}(i)$ is, for bin i, the efficiency on taus of the selection including all cuts; $\sigma_s(i)$ arises from the integral in bin i of the expression for $d\sigma/d\cos\theta^*$ given by Eq. (8); $\mathcal{L}$ is the integrated luminosity at this energy; $\sigma_t(i)$ is the t channel plus interference cross section inside the acollinearity cut as calculated from the program ALISTAR [36].

The factor $\varepsilon_{\mathrm{acol}}(i)$ takes into account the acollinearity cut and therefore the s'/s effect, which, as observed before, is almost entirely related to the acollinearity.

A maximum likelihood fit is performed with two variables, namely C and A_{FB}, as free parameters, the predicted number of events as given above being compared with the observed number of events in that $\cos\theta^*$ bin.

11.2.3 Systematic uncertainties and correlations

The systematic errors associated with the selection procedure have already been described in detail in Section 10.4.3 in connection with the discussion of the Bhabha cross section. The systematic effects induced by the same-sign event removal and by $\mathrm{e^+e^-V}$ events are negligible compared with other sources of systematic error. The dominant source of systematic error for most of the data points is that due to the t channel subtraction. It amounts to 0.0011 at the peak and it is estimated by rescaling all bins according to the required systematic uncertainty as tabulated in Table 11 and then re-performing the fit.

The estimate of the efficiencies relies on the KORALZ and UNIBAB generators which do not include the interference between initial and final state radiation. The effect of the interference on the asymmetry has been estimated with ZFITTER to be at the level of a few 10^{-4}.

The nature of the correlations of the systematic errors is identical to that for the cross section calculation. For two data points from the same year but of different energies the correlation coefficient is of the order of (80–90)%; for two same energy points from different years the coefficient is of a similar magnitude.

Two sources of correlation between the measurements of $\sigma_{\mathrm{e^+e^-}}$ and $A^{\mathrm{e}}_{\mathrm{FB}}$ are identified, which are related to the subtraction of the very asymmetric t channel and to the choice of an asymmetric acceptance.

The t channel uncertainty affects the cross section and asymmetry measurements in a correlated manner. It is of statistical and systematic origin. The effect at the peak for a change of the t channel uncertainty (discussed in Section 9.3) by ±1 standard deviation is

∓ 1.5 pb on the cross section and ∓ 0.0011 on the asymmetry. In addition, measurements at the same energy point are affected by statistical fluctuations of the t channel contribution, amounting to a correlation coefficient of 11% between the statistical errors of $\sigma_{\mathrm{e^+e^-}}$ and $A_{\mathrm{FB}}^{\mathrm{e}}$ at the peak. A detailed correlation matrix for all energy points was constructed to take these effects into account.

The second source of correlation between $\sigma_{\mathrm{e^+e^-}}$ and $A_{\mathrm{FB}}^{\mathrm{e}}$ arises from the choice of an asymmetric acceptance. This leads to a dependence on the value of the asymmetry when extrapolating the s channel cross section to full acceptance. In order to take this effect into account, the detailed dependence of the peak cross section on the assumed value of $A_{\mathrm{FB}}^{\mathrm{e}}$ at the peak was studied with ZFITTER and was dealt with by means of a parametrisation applied at the fitting stage, as explained in Section 13.1.

12 Summary of results

Table 21 summarises the cross sections for hadrons and lepton pairs as a function of centre-of-mass energy. The first error on the cross sections is statistical (due to event selection and luminosity) and the second one systematic (due to event selection only). The values of the cross sections are corrected for the effect of the centre-of-mass energy spread of LEP, as described in Section 13. The lepton cross sections represent the average of the exclusive and global analyses.

The lepton forward-backward asymmetries are shown in Table 22. The results are also corrected for the effect of the centre-of-mass energy spread of LEP, although this is noticeable only for the electron asymmetry due to the particular energy dependence on the t channel contribution. These corrections lead to a reduction of $\mathrm{A_{FB}^{0,e}}$ (defined by Eq. (16)) by 0.0002.

The full set of cross section and lepton forward-backward asymmetry measurements including systematic errors and their correlation matrices is available in Ref. [41].

Table 21: Hadronic and leptonic cross sections: the uncertainties are statistical (due to event selection and luminosity) and experimental systematic, respectively. The error on the electron cross sections includes the uncertainty from the t channel subtraction. For the energy points labelled with †, only the ratio of hadrons to leptons is meaningful due to the lack of a precise luminosity measurement.

Year	$\sqrt{s}$ (GeV)	$\mathcal{L}$(nb^{-1})	σ_{had} (nb)	$\sigma_{\mathrm{e^+e^-}}$ (nb)	$\sigma_{\mu^+\mu^-}$ (nb)	$\sigma_{\tau^+\tau^-}$ (nb)
1990	88.223	482	$4.63 \pm 0.11 \pm 0.01$	$0.241 \pm 0.038 \pm 0.002$	$0.244 \pm 0.025 \pm 0.001$	$0.183 \pm 0.023 \pm 0.003$
	89.217	520	$8.44 \pm 0.15 \pm 0.01$	$0.330 \pm 0.041 \pm 0.003$	$0.498 \pm 0.034 \pm 0.001$	$0.400 \pm 0.032 \pm 0.004$
	90.217	447	$18.43 \pm 0.26 \pm 0.02$	$0.914 \pm 0.063 \pm 0.003$	$0.903 \pm 0.050 \pm 0.002$	$0.895 \pm 0.050 \pm 0.007$
	91.215	3624	$30.43 \pm 0.14 \pm 0.03$	$1.473 \pm 0.026 \pm 0.004$	$1.428 \pm 0.022 \pm 0.003$	$1.537 \pm 0.024 \pm 0.009$
	92.207	555	$21.84 \pm 0.25 \pm 0.03$	$1.083 \pm 0.054 \pm 0.004$	$1.009 \pm 0.047 \pm 0.003$	$1.072 \pm 0.050 \pm 0.007$
	93.209	597	$12.44 \pm 0.17 \pm 0.02$	$0.627 \pm 0.040 \pm 0.002$	$0.637 \pm 0.036 \pm 0.002$	$0.591 \pm 0.036 \pm 0.005$
	94.202	642	$8.00 \pm 0.12 \pm 0.01$	$0.402 \pm 0.031 \pm 0.002$	$0.430 \pm 0.029 \pm 0.001$	$0.394 \pm 0.028 \pm 0.003$
1991	91.238	4609	$30.64 \pm 0.12 \pm 0.03$	$1.451 \pm 0.023 \pm 0.003$	$1.476 \pm 0.020 \pm 0.002$	$1.490 \pm 0.021 \pm 0.006$
	88.464	668	$5.50 \pm 0.10 \pm 0.01$	$0.266 \pm 0.034 \pm 0.002$	$0.260 \pm 0.022 \pm 0.001$	$0.278 \pm 0.024 \pm 0.002$
	89.455	797	$10.06 \pm 0.13 \pm 0.01$	$0.533 \pm 0.038 \pm 0.002$	$0.541 \pm 0.029 \pm 0.001$	$0.509 \pm 0.029 \pm 0.003$
	90.212	753	$18.14 \pm 0.20 \pm 0.02$	$0.879 \pm 0.047 \pm 0.003$	$0.917 \pm 0.039 \pm 0.002$	$0.923 \pm 0.040 \pm 0.004$
	91.207	2937	$30.65 \pm 0.15 \pm 0.03$	$1.534 \pm 0.029 \pm 0.003$	$1.543 \pm 0.025 \pm 0.002$	$1.493 \pm 0.026 \pm 0.006$
	91.952	693	$25.39 \pm 0.27 \pm 0.03$	$1.207 \pm 0.051 \pm 0.004$	$1.196 \pm 0.046 \pm 0.003$	$1.328 \pm 0.050 \pm 0.007$
	92.952	677	$14.67 \pm 0.17 \pm 0.02$	$0.687 \pm 0.039 \pm 0.002$	$0.655 \pm 0.034 \pm 0.002$	$0.711 \pm 0.037 \pm 0.004$
	93.701	797	$10.15 \pm 0.13 \pm 0.01$	$0.506 \pm 0.031 \pm 0.002$	$0.503 \pm 0.028 \pm 0.001$	$0.512 \pm 0.029 \pm 0.003$
1992	91.276	12298	$30.734 \pm 0.071 \pm 0.022$	$1.493 \pm 0.014 \pm 0.003$	$1.488 \pm 0.012 \pm 0.001$	$1.496 \pm 0.013 \pm 0.004$
	91.270	8749	$30.632 \pm 0.070 \pm 0.022$	$1.509 \pm 0.017 \pm 0.003$	$1.490 \pm 0.014 \pm 0.001$	$1.488 \pm 0.015 \pm 0.004$
1993	91.303	5314	$30.645 \pm 0.089 \pm 0.022$	$1.496 \pm 0.021 \pm 0.003$	$1.470 \pm 0.018 \pm 0.002$	$1.488 \pm 0.019 \pm 0.004$
	89.432	8070	$9.891 \pm 0.037 \pm 0.011$	$0.489 \pm 0.012 \pm 0.002$	$0.4810 \pm 0.0085 \pm 0.0010$	$0.4984 \pm 0.0090 \pm 0.0024$
	91.187	9135	$30.468 \pm 0.068 \pm 0.021$	$1.459 \pm 0.016 \pm 0.003$	$1.484 \pm 0.014 \pm 0.002$	$1.489 \pm 0.014 \pm 0.004$
	93.015	8690	$14.032 \pm 0.043 \pm 0.013$	$0.699 \pm 0.011 \pm 0.002$	$0.6724 \pm 0.0097 \pm 0.0015$	$0.703 \pm 0.010 \pm 0.003$
1994	(†) 91.219	12440	$30.454 \pm 0.071 \pm 0.022$	$1.488 \pm 0.014 \pm 0.002$	$1.473 \pm 0.012 \pm 0.001$	$1.489 \pm 0.012 \pm 0.003$
	91.197	42695	$30.390 \pm 0.031 \pm 0.022$	$1.4938 \pm 0.0075 \pm 0.0024$	$1.4808 \pm 0.0065 \pm 0.0013$	$1.4771 \pm 0.0066 \pm 0.0027$
1995	(†) 91.293	12396	$30.669 \pm 0.071 \pm 0.022$	$1.479 \pm 0.014 \pm 0.003$	$1.500 \pm 0.012 \pm 0.002$	$1.496 \pm 0.012 \pm 0.004$
	89.440	8121	$9.978 \pm 0.041 \pm 0.012$	$0.495 \pm 0.012 \pm 0.002$	$0.4927 \pm 0.0086 \pm 0.0011$	$0.4897 \pm 0.0089 \pm 0.0021$
	91.282	4873	$30.53 \pm 0.12 \pm 0.02$	$1.497 \pm 0.022 \pm 0.003$	$1.464 \pm 0.019 \pm 0.002$	$1.468 \pm 0.020 \pm 0.004$
	92.968	9373	$14.297 \pm 0.049 \pm 0.013$	$0.697 \pm 0.011 \pm 0.002$	$0.7114 \pm 0.0097 \pm 0.0016$	$0.703 \pm 0.010 \pm 0.003$

Table 22: Forward-backward asymmetries for all three lepton species as a function of centre-of-mass energy. The errors are statistical and systematic, respectively. The systematic error on the electrons includes the uncertainty from the t channel subtraction. For the analysis of the muon and tau asymmetries in 1991 and 1994 the two points at the peak were combined into a single point labelled with †.

Year	$\sqrt{s}$ (GeV)	$A_{\mathrm{FB}}^{\mathrm{e}}$	A_{FB}^{μ}	A_{FB}^{τ}
1990	88.223	$-0.40 \pm 0.26 \pm 0.01$	$-0.12 \pm 0.10 \pm 0.00$	$-0.23 \pm 0.11 \pm 0.01$
	89.217	$-0.48 \pm 0.21 \pm 0.01$	$-0.326 \pm 0.062 \pm 0.001$	$-0.073 \pm 0.078 \pm 0.003$
	90.217	$-0.176 \pm 0.085 \pm 0.004$	$-0.164 \pm 0.052 \pm 0.001$	$-0.065 \pm 0.059 \pm 0.012$
	91.215	$-0.014 \pm 0.019 \pm 0.002$	$-0.001 \pm 0.015 \pm 0.001$	$0.003 \pm 0.015 \pm 0.001$
	92.207	$0.147 \pm 0.050 \pm 0.001$	$0.100 \pm 0.046 \pm 0.001$	$0.112 \pm 0.047 \pm 0.003$
	93.209	$0.238 \pm 0.060 \pm 0.002$	$0.150 \pm 0.052 \pm 0.001$	$0.255 \pm 0.057 \pm 0.007$
	94.202	$0.150 \pm 0.080 \pm 0.002$	$0.155 \pm 0.064 \pm 0.001$	$0.289 \pm 0.068 \pm 0.005$
1991	91.238	$0.015 \pm 0.017 \pm 0.001$		
	88.464	$-0.22 \pm 0.18 \pm 0.01$	$-0.327 \pm 0.074 \pm 0.001$	$-0.174 \pm 0.080 \pm 0.005$
	89.455	$-0.136 \pm 0.089 \pm 0.005$	$-0.263 \pm 0.048 \pm 0.001$	$-0.118 \pm 0.057 \pm 0.009$
	90.212	$-0.182 \pm 0.067 \pm 0.003$	$-0.076 \pm 0.040 \pm 0.001$	$-0.093 \pm 0.043 \pm 0.004$
	91.207	$-0.003 \pm 0.021 \pm 0.001$		
	(†)91.228		$-0.003 \pm 0.010 \pm 0.001$	$-0.006 \pm 0.011 \pm 0.001$
	91.952	$0.065 \pm 0.045 \pm 0.002$	$0.106 \pm 0.037 \pm 0.001$	$-0.003 \pm 0.038 \pm 0.003$
	92.952	$0.015 \pm 0.060 \pm 0.002$	$0.073 \pm 0.050 \pm 0.001$	$0.145 \pm 0.051 \pm 0.002$
	93.701	$0.200 \pm 0.061 \pm 0.002$	$0.081 \pm 0.052 \pm 0.001$	$0.165 \pm 0.056 \pm 0.004$
1992	91.276	$0.002 \pm 0.010 \pm 0.001$	$0.0045 \pm 0.0074 \pm 0.0005$	$0.0019 \pm 0.0080 \pm 0.0019$
	91.270	$0.027 \pm 0.012 \pm 0.001$	$0.0139 \pm 0.0093 \pm 0.0005$	$-0.001 \pm 0.010 \pm 0.002$
1993	91.303	$-0.002 \pm 0.015 \pm 0.001$	$0.029 \pm 0.012 \pm 0.001$	$0.019 \pm 0.013 \pm 0.003$
	89.432	$-0.170 \pm 0.030 \pm 0.004$	$-0.179 \pm 0.017 \pm 0.001$	$-0.182 \pm 0.018 \pm 0.004$
	91.187	$0.020 \pm 0.012 \pm 0.001$	$0.0100 \pm 0.0092 \pm 0.0005$	$-0.0004 \pm 0.0098 \pm 0.0009$
	93.015	$0.126 \pm 0.016 \pm 0.002$	$0.120 \pm 0.014 \pm 0.001$	$0.141 \pm 0.014 \pm 0.002$
1994	91.219	$0.003 \pm 0.010 \pm 0.001$		
	(†)91.201		$0.0020 \pm 0.0037 \pm 0.0005$	$0.0027 \pm 0.0040 \pm 0.0007$
	91.197	$0.0049 \pm 0.0054 \pm 0.0012$		
1995	91.293	$0.002 \pm 0.010 \pm 0.001$	$0.0087 \pm 0.0077 \pm 0.0005$	$0.0096 \pm 0.0089 \pm 0.0007$
	89.440	$-0.190 \pm 0.030 \pm 0.004$	$-0.155 \pm 0.017 \pm 0.001$	$-0.157 \pm 0.019 \pm 0.001$
	91.282	$0.013 \pm 0.016 \pm 0.001$	$0.003 \pm 0.012 \pm 0.001$	$0.007 \pm 0.014 \pm 0.001$
	92.968	$0.102 \pm 0.015 \pm 0.002$	$0.096 \pm 0.013 \pm 0.001$	$0.110 \pm 0.015 \pm 0.001$

13 Determination of the Z resonance parameters

From the measured cross sections the electroweak parameters describing the Z resonance are extracted after correction for QED effects. The dominant QED process is bremsstrahlung from the initial state, which leads to an effective reduction of the centre-of-mass energy for the e^+e^- annihilation process. Photonic corrections are taken into account by convoluting the electroweak cross section $\sigma^{\rm ew}$ with a "radiator function" $H(s,s')$, which describes the probability for the effective centre-of-mass energy-squared to be reduced from s to s' due to photon radiation. The convolution integral is

$$\sigma(s)_{\rm f\bar{f}} = \int_{s_{\rm min}}^{s} \sigma^{\rm ew}_{\rm f\bar{f}}(s')H(s,s')ds' \,. \tag{11}$$

Here, $s_{\rm min}$ is the minimum invariant mass squared of the $\rm f\bar{f}$ system, which is set to the same value used in the Monte Carlo event generation when determining detector acceptances (Section 6.2). The electroweak cross section near $\sqrt{s} = M_{\rm Z}$ is completely dominated by the Z exchange. The parametrisation is based on a Breit-Wigner shape with an s-dependent width, and is given in the "improved Born approximation" by

$$\sigma^{\rm ew}_{\rm f\bar{f}}(s) \;=\; \sigma^0_{\rm f\bar{f}}\, \frac{1}{1+\delta_{\rm QED}}\, \frac{s\Gamma^2_{\rm Z}}{\left(s-M^2_{\rm Z}\right)^2 + s^2\Gamma^2_{\rm Z}/M^2_{\rm Z}} \;+\; \sigma_\gamma \;+\; \sigma_{\gamma \rm Z} \,, \tag{12}$$

where the parameters are the Z mass $M_{\rm Z}$, the width $\Gamma_{\rm Z}$, and the peak cross section $\sigma^0_{\rm f\bar{f}}$ and $\delta_{\rm QED} = 3\alpha(M_{\rm Z})/4\pi$. The γ exchange and γZ interference terms, σ_γ and $\sigma_{\gamma\rm Z}$, respectively, are small near the resonance peak, with contributions of about 1 % at the peak for the first and less than 0.2 % within 3 GeV of the peak for the second. The peak cross section $\sigma^0_{\rm f\bar{f}}$ can be written in terms of partial decay widths of the initial and final states, $\Gamma_{\rm ee}$ and $\Gamma_{\rm f\bar{f}}$,

$$\sigma^0_{\rm f\bar{f}} = \frac{12\pi}{M^2_{\rm Z}} \frac{\Gamma_{\rm ee}\Gamma_{\rm f\bar{f}}}{\Gamma^2_{\rm Z}} \,. \tag{13}$$

Here $\Gamma_{\rm f\bar{f}}$ represents the physical partial width of the Z into the fermion pair $\rm f\bar{f}$ and includes by definition all radiative corrections. Since the initial state radiation is taken into account by the convolution procedure, the contribution of the QED final state radiation correction $\delta_{\rm QED}$ is removed from the initial state width $\Gamma_{\rm ee}$ in Eq. (12), thus avoiding a double counting.

The inclusive partial widths are given by

$$\Gamma_{\rm f\bar{f}} = \frac{G_{\rm F} M^3_{\rm Z}}{6\pi\sqrt{2}} N^{\rm f}_c (g^2_{V_{\rm f}}\, R^{\rm f}_V + g^2_{A_{\rm f}}\, R^{\rm f}_A) \,, \tag{14}$$

where $g_{V_{\rm f}}$ and $g_{A_{\rm f}}$ are the effective vector and axial vector couplings of the Z to fermion species f that absorb electroweak radiative corrections, and $N^{\rm f}_c$, the number of colours, is 1 for leptons and 3 for quarks. The factors $R^{\rm f}_V$ and $R^{\rm f}_A$ include QED and QCD final-state radiation and fermion mass effects. At leading order, without mass effects, they are given by $R^{\rm f}_V = R^{\rm f}_A \simeq (1 \,+\, 3\,Q^2_{\rm f}\,\alpha(M_{\rm Z})/4\pi \,+\, \alpha_s(M_{\rm Z})/\pi)$, where $Q_{\rm f}$ is the fermion charge and the QCD correction applies only for quarks.

The peak cross sections $\sigma^0_{\mathrm{f\bar{f}}}$ for each fermion species f have in common the statistical and systematic error from the luminosity determination. It is therefore preferable to use the ratios of peak cross sections in the parametrisation of the lepton channels,

$$R_\ell = \frac{\sigma^0_{\mathrm{had}}}{\sigma^0_{\ell^+\ell^-}} \equiv \frac{\Gamma_{\mathrm{had}}}{\Gamma_{\ell^+\ell^-}} \tag{15}$$

for $\ell^+\ell^- = \mathrm{e^+e^-}, \mu^+\mu^-, \tau^+\tau^-$. The measurements of the lepton forward-backward asymmetries can be condensed into one single parameter per lepton species in the final state, the peak asymmetry $\mathrm{A^{0,f}_{FB}}$. This is given by the following combinations of effective couplings:

$$\mathrm{A^{0,f}_{FB}} \equiv \frac{3}{4}\mathcal{A}_\mathrm{e}\mathcal{A}_\mathrm{f} \tag{16}$$

with

$$\mathcal{A}_\mathrm{f} \equiv \frac{2 g_{V_\mathrm{f}} g_{A_\mathrm{f}}}{g^2_{V_\mathrm{f}} + g^2_{A_\mathrm{f}}} \,. \tag{17}$$

Due to higher order electroweak corrections the effective couplings are complex numbers, however with small imaginary parts. Depending on the fitting procedure used, the partial widths are either defined in terms of the real parts of the couplings, ignoring the imaginary parts, as is the case in MIZA [42], or the imaginary parts are included in the definition of the widths [43], as in ZFITTER [40] or TOPAZ0 [44]. The effect of the imaginary parts on the partial widths is of $\mathcal{O}(10^{-2}\%)$. For the forward-backward asymmetries, the non-negligible contributions from the imaginary parts of the photon vacuum polarisation and from the effective couplings are set to their Standard Model expectations, but conventionally not included in the definition of $\mathrm{A^{0,f}_{FB}}$. The relative contribution of these imaginary parts to the peak asymmetry is of $\mathcal{O}(1\%)$. Hereafter, the symbols g_{V_f} and g_{A_f} refer to the real parts of the effective couplings.

From the above discussion it is clear that the parameters describing the differential cross section can only be extracted from the measured cross sections and forward-backward asymmetries with some theoretical input, and are therefore denoted as "pseudo-observables".

13.1 The fit procedure

The nine pseudo-observables M_Z, Γ_Z, σ^0_{had}, R_e, R_μ, R_τ, $\mathrm{A^{0,e}_{FB}}$, $\mathrm{A^{0,\mu}_{FB}}$, and $\mathrm{A^{0,\tau}_{FB}}$ were fitted to the whole set of cross sections and forward-backward lepton asymmetries. The fit used the latest version of program ZFITTER (Version 6.10) and was cross-checked with TOPAZ0 (Version 4.4) and with the more model-independent MIZA approach, which was also used in earlier publications [1–4]. These codes provide parametrisations of the fermion pair production cross sections and of the forward-backward asymmetries at energies around the Z resonance in terms of effective couplings. They also calculate pure QED corrections to full $\mathcal{O}(\alpha^2)$ with leading $\mathcal{O}(\alpha^3)$ and exponentiation of the soft part, taking into account the interference between photons radiated from the initial and final states to first order. Radiation from the initial state includes fermionic pairs. QCD corrections are included up to third order in $\alpha_s(M_\mathrm{Z})$ with correct treatment of non factorisable QED and QCD corrections.

In the parametrisation of the electroweak cross section, the pure photon exchange and γZ interference contributions to the cross sections are fixed to their Standard Model values, as are the imaginary parts of the couplings.

The measured cross sections and forward-backward asymmetries are treated in a χ^2 minimisation procedure to extract the nine pseudo-observables with their errors and correlations. The full error matrix ($\mathcal{V}$) of the input measurements includes the statistical and experimental systematic errors and their correlations, the statistical and systematic errors of the luminosity measurements, the LEP beam energy uncertainties, the theoretical uncertainties on the small-angle Bhabha cross section and on the t channel contribution to the wide-angle Bhabha events.

The correlation between the electron cross sections and asymmetries arising from the choice of an asymmetric acceptance region of $-0.9 < \cos\theta^* < 0.7$ in the electron channel is taken into account by correcting the predicted electron cross sections in the fits by a factor depending on the measured forward-backward asymmetry:

$$\sigma'_{\mathrm{e}} = \sigma_{\mathrm{e}} \left(1 + c \left[\mathrm{A}_{\mathrm{FB}}^{0,\mathrm{e}} - (\mathrm{A}_{\mathrm{FB}}^{0,\mathrm{e}})^{\mathrm{MC}}\right]\right) .$$

Here, the coefficient $c = -0.225$ represents the dependence of R_{e} on $\mathrm{A}_{\mathrm{FB}}^{0,\mathrm{e}}$, and $(\mathrm{A}_{\mathrm{FB}}^{0,\mathrm{e}})^{\mathrm{MC}} = 0.0154$ is the value of the asymmetry originally chosen for the acceptance calculations in the Monte Carlo generators. If lepton universality is assumed, the only change in the above formula is that $\mathrm{A}_{\mathrm{FB}}^{0,\mathrm{e}}$ is replaced by $\mathrm{A}_{\mathrm{FB}}^{0,\ell}$.

In the fit procedure, the interference between the s and t channels in the $\mathrm{e}^+\mathrm{e}^- \to \mathrm{e}^+\mathrm{e}^-$ process, which has a dependence on M_{Z}, is evaluated for a Z mass equal to the LEP average value. The error on the uncertainty on M_{Z} is taken into account as a systematic error, as explained in Section 9.3. It was checked that an alternative fit procedure in which the interference term is parametrised as a function of M_{Z} changes the correlation coefficients between M_{Z} and R_{e} ($\mathrm{A}_{\mathrm{FB}}^{0,\mathrm{e}}$) by +15% (-13%) and the central values of R_{e} and $\mathrm{A}_{\mathrm{FB}}^{0,\mathrm{e}}$ by approximately 10% of their errors.

13.1.1 Treatment of energy errors

The error matrix elements $(\mathcal{V}^E)_{i,j}$ from the determination of the centre-of-mass energy, as specified in Section 5, are propagated into errors on the measured cross sections via

$$(\mathcal{V})_{i,j}^{\mathrm{energy}} = \frac{d\sigma(E_i)}{dE}(\mathcal{V}^E)_{i,j}\frac{d\sigma(E_j)}{dE} .$$

The dispersion of the centre-of-mass energy due to the natural spread in energy of the beam particles leads to a correction on the measured cross sections and asymmetries. The measurements represent a folding with the energy distribution of the beam particles, which is assumed to be of a Gaussian form with a width of δE in centre-of-mass energy. To arrive at measurements at a single, sharp value in energy, a correction is needed which is given in leading order by

$$\delta\sigma(E) \approx -\frac{1}{2}\frac{d^2\sigma(E)}{dE^2}\delta E^2 \ .$$

The values for the energy spread at each energy point are given in Table 3 of Section 5. The corrections are calculated numerically based on the line shape parametrisation given above, with parameter values corresponding to the best-fit point. The energy-spread correction induces a change in the cross section at $\sqrt{s} = M_{\mathrm{Z}}$ of 0.16%, which results in a decrease of the total Z width of about 5 MeV with negligible error. The effect on M_{Z} and the other parameters is negligible compared to the experimental errors.

13.2 Five- and nine-parameter fits

As mentioned in Section 10.6, fits were performed separately using the dilepton cross sections from the exclusive and global analyses. The results of the two fits are in good agreement; using independent statistical errors only, the hypothesis of no difference in the central values for R_e, R_μ and R_τ has a value of χ^2 per degree of freedom of 4.5/3, corresponding to a confidence level of 20%. The average of the two fits agrees well with a fit to the combined cross sections, given in Table 21; differences in the central values of the fitted parameters between the two approaches amount to 2 % of the total error at most, and therefore all results given in the following will be based on the combined cross sections of Table 21.

The results of the nine-parameter fit with ZFITTER are shown in Table 23 and the correlation matrices in Table 24. The value of the electron peak asymmetry was corrected by -0.00015 to take into account the difference in the QED correction originating from the use of $\cos\theta^*$ in the electron asymmetry analysis. Since this is not implemented in ZFITTER, this particular correction was calculated with MIZA. The MIZA results are also given in the table for comparison.

The agreement of the measurements with the parametrisation is good, indicated by the value of χ^2 per degree of freedom of approximately 169/176, which corresponds to a confidence level of 63%. Figures 21 and 22 show the data points with a solid curve representing the fit results.

The values obtained for R_ℓ and $\mathrm{A}_{\mathrm{FB}}^{0,\ell}$ for the different lepton species are identical within errors, in agreement with the assumption of universality of the Z couplings to leptons. Mass corrections lead to a value of R_τ which is expected to be about 0.2% larger than for the light leptons. The fits were repeated with five free parameters and assuming universal quantities R_ℓ and $\mathrm{A}_{\mathrm{FB}}^{0,\ell}$. Here, the lepton width is defined as the partial Z decay width into a pair of massless leptons. The results are also shown in Table 23. These five measurements constitute the minimal set of parameters needed to describe the dominant dependence on Z parameters of the differential cross section near the Z resonance. The contour lines of the ratios of hadronic and lepton widths and of the peak asymmetries from the nine- and five-parameter fits are shown in Fig. 23 and illustrate the good agreement among the lepton species.

Table 23: Results of the five and nine parameter fits to the cross section and asymmetry data.

	ZFITTER	MIZA
nine-parameter fit		
M_Z (GeV/c^2)	91.1886±0.0031	91.1888±0.0031
Γ_Z (GeV)	2.4952±0.0043	2.4957±0.0043
σ^0_{had} (nb)	41.558±0.058	41.539±0.058
R_e	20.677±0.075	20.684±0.075
R_μ	20.799±0.056	20.802±0.056
R_τ	20.707±0.062	20.715±0.063
$A^{0,e}_{FB}$	0.0188±0.0034	0.0188±0.0034
$A^{0,\mu}_{FB}$	0.0171±0.0024	0.0170±0.0025
$A^{0,\tau}_{FB}$	0.0170±0.0028	0.0166±0.0028
five-parameter fit		
M_Z (GeV/c^2)	91.1885±0.0031	91.1888±0.0031
Γ_Z (GeV)	2.4951±0.0043	2.4956±0.0043
σ^0_{had} (nb)	41.559±0.058	41.540±0.058
R_ℓ	20.725±0.039	20.731±0.039
$A^{0,\ell}_{FB}$	0.0173±0.0016	0.0171±0.0016

Table 24: Correlation matrices of the measurements shown in Table 23.

nine-parameter correlation matrix									
	M_Z	Γ_Z	σ^0_{had}	R_e	R_μ	R_τ	$A^{0,e}_{FB}$	$A^{0,\mu}_{FB}$	$A^{0,\tau}_{FB}$
M_Z	1.00	0.03	−0.09	−0.05	0.00	0.00	0.08	0.07	0.06
Γ_Z		1.00	−0.38	0.00	0.01	0.00	0.00	0.00	0.00
σ^0_{had}			1.00	0.15	0.17	0.15	−0.01	0.00	0.00
R_e				1.00	0.09	0.07	−0.39	0.01	0.01
R_μ					1.00	0.10	0.00	0.01	0.00
R_τ						1.00	0.00	0.00	0.01
$A^{0,e}_{FB}$							1.00	0.00	0.00
$A^{0,\mu}_{FB}$								1.00	0.02
$A^{0,\tau}_{FB}$									1.00

five-parameter correlation matrix					
	M_Z	Γ_Z	σ^0_{had}	R_ℓ	$A^{0,\ell}_{FB}$
M_Z	1.00	0.03	−0.09	−0.02	0.12
Γ_Z		1.00	−0.38	0.01	0.00
σ^0_{had}			1.00	0.25	0.00
R_ℓ				1.00	−0.08
$A^{0,\ell}_{FB}$					1.00

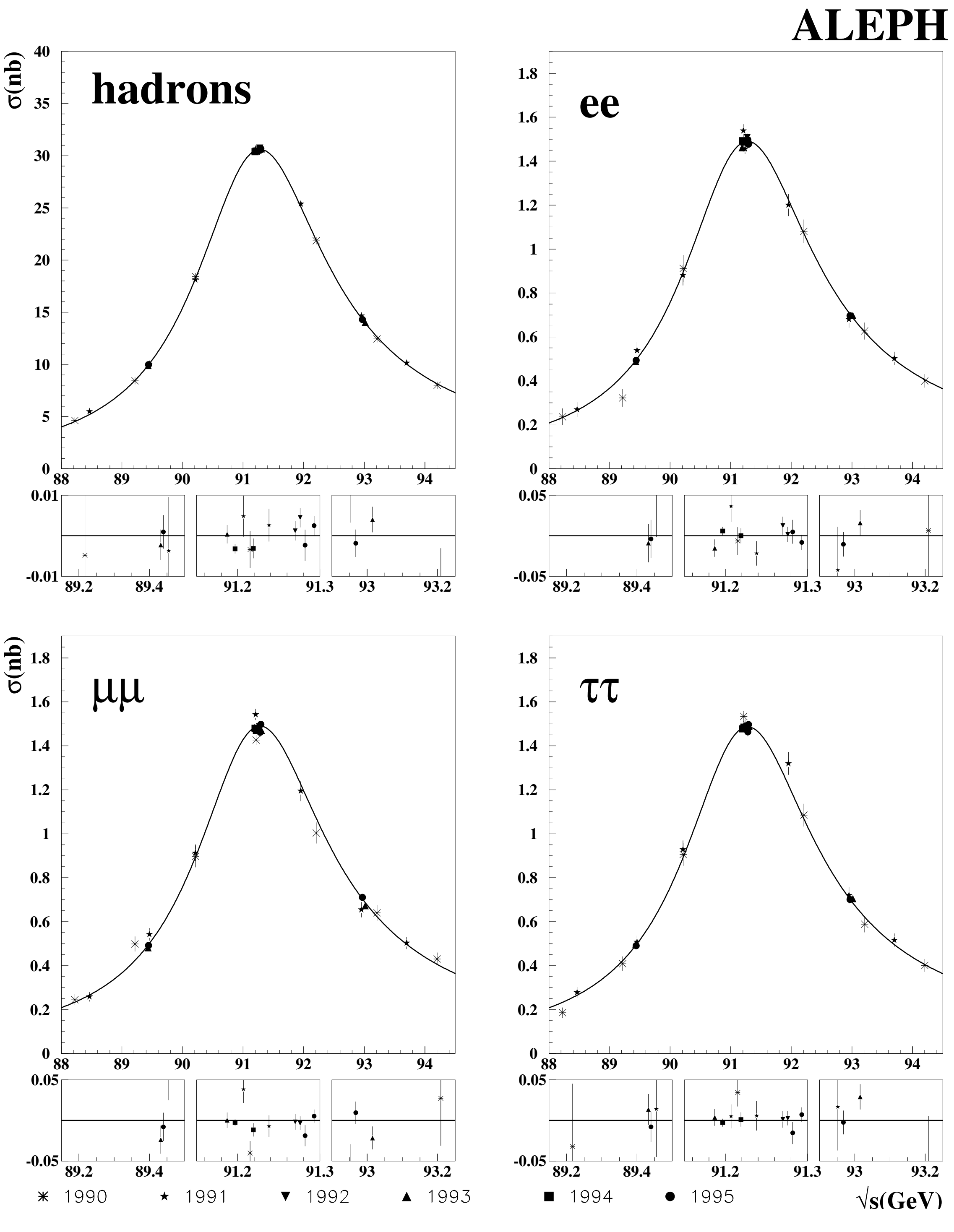

Figure 21: Measurement of cross sections. The solid lines show the result of the Standard Model fit. The inserts show enlarged views of the peak, peak−2 and peak+2 regions for the relative difference between data and fit.

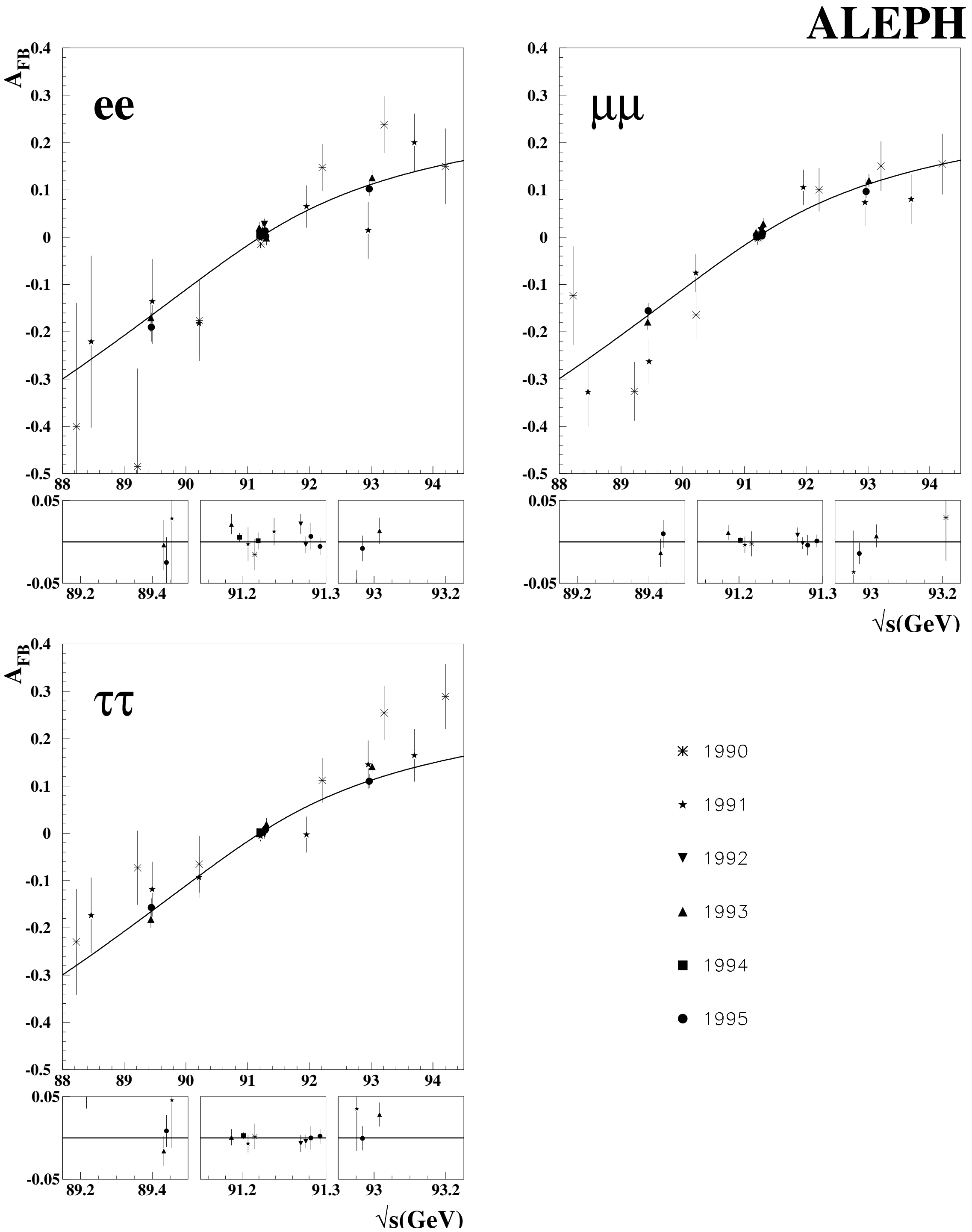

Figure 22: Measurements of forward-backward asymmetries. The solid lines show the results of the Standard Model fit. The inserts show enlarged views of the peak, peak−2 and peak+2 regions for the difference between data and fit.

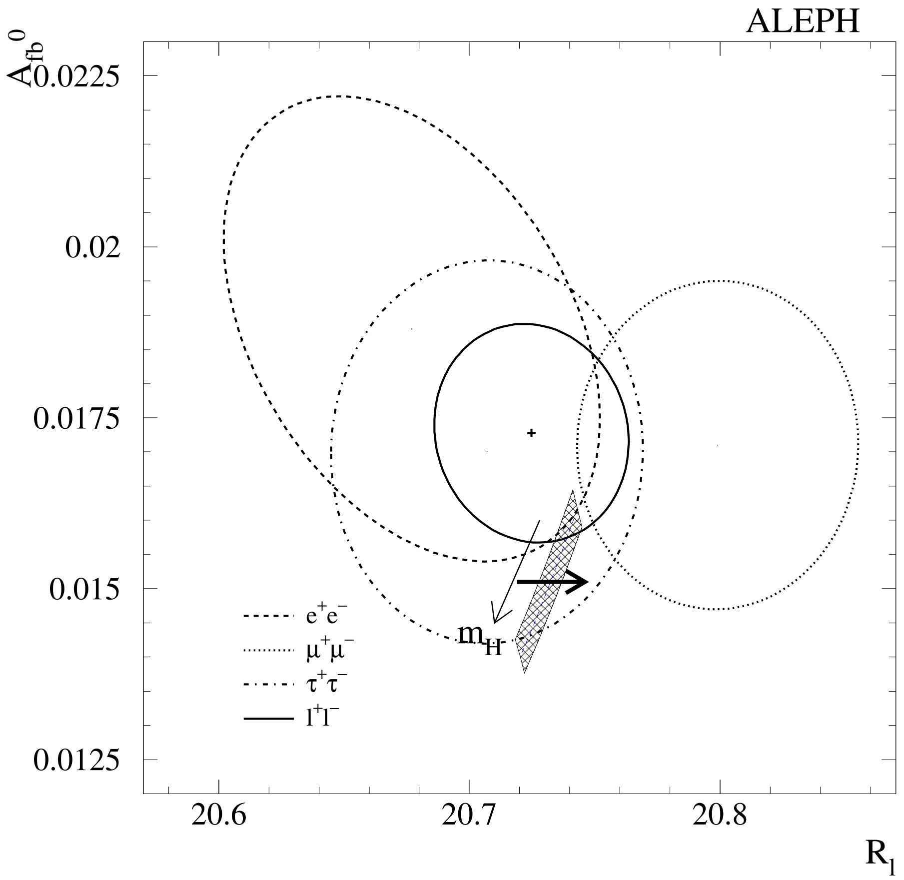

Figure 23: The peak asymmetry vs the ratio of hadronic and lepton widths for all lepton species separately and assuming lepton universality. Shown are the one-σ contours (39.3 % CL). The shaded area shows the Standard Model expectation for $M_t = 174 \pm 5$ GeV/c^2 and $90 < M_H/\text{GeV}/c^2 < 1000$; the horizontal arrow shows the change if the strong coupling constant is varied within $\alpha_s(M_Z) = 0.119 \pm 0.002$.

13.2.1 Discussion of errors

The errors given in Table 23 include statistical and experimental systematic errors as well as the uncertainties induced by the uncertainty in the centre-of-mass energy and its spread and also the dominant theoretical uncertainties. Details on these errors are discussed in the following, and a breakdown is shown in Table 25.

Effect of experimental systematic errors

The effect of purely experimental errors on the fitted parameters was determined from special fits which considered only subsets of the error components on the cross sections and asymmetries. By comparison with the fit including all errors, the experimental statistical and systematic uncertainties were obtained by taking the differences in quadrature of the

Table 25: Breakdown of the errors on the results of Table 23. These numbers serve as an illustration only, since the effects of correlations between the various errors do not allow the calculation of the total uncertainties by adding the individual components in quadrature.

	stat.	exp. syst.	beam energy	spread in $\sqrt{s}$	luminosity	Bhabha t chan.	theory
M_Z (GeV/c^2)	0.0024	0.0002	0.0017	0.0001			0.0005
Γ_Z (GeV)	0.0038	0.0009	0.0013	0.0003			0.0005
σ^0_{had} (nb)	0.030	0.026	0.010	0.004	0.025		0.010
R_e	0.062	0.033	0.013			0.026	0.003
R_μ	0.053	0.021	0.006				0.003
R_τ	0.054	0.033	0.006				0.003
$A^{0,e}_{FB}$	0.0031	0.0006	0.0002			0.0013	0.0001
$A^{0,\mu}_{FB}$	0.0024	0.0005	0.0002				0.0001
$A^{0,\tau}_{FB}$	0.0026	0.0011	0.0002				0.0001
R_ℓ	0.033	0.020	0.002			0.005	0.003
$A^{0,\ell}_{FB}$	0.0015	0.0004	0.0001			0.0002	0.0001

Table 26: Covariance matrix of the most important errors arising from the uncertainty in the energy of the LEP beams.

	M_Z (GeV/c^2)	Γ_Z (GeV)	σ^0_{had} (nb)
M_Z (GeV/c^2)	0.0017^2		
Γ_Z (GeV)	-0.0006^2	0.0013^2	
σ^0_{had} (nb)	-0.0027^2	-0.0028^2	0.011^2

corresponding errors. All measurements except that of the hadronic peak cross section are dominated by statistical errors.

Errors from LEP beam energy uncertainty

The contributions of the energy-related uncertainties to the errors on the nine fitted parameters were determined by comparing two fits with the experimental errors entering into the matrix scaled by $\pm 10\,\%$, while the energy-related errors remained unchanged. The contribution of energy errors to the covariance matrix of the fitted pseudo-observables was then extracted analytically. The energy-related errors on the fitted parameters are shown in Table 26. Compared with other errors, only the contributions to the errors on M_Z and Γ_Z are important, amounting to 1.7 MeV/c^2 and 1.3 MeV, respectively.

The uncertainties in the energy spread, given in Table 3 of Section 5, lead to an uncertainty of ± 0.3 MeV on Γ_Z, and a negligible contribution of ± 0.004 nb to the error on σ^0_{had}; they are totally negligible for other parameters.

As a further check on the quality of the beam energy calibration, the Z mass was determined for three periods of data taking, namely for data before and including 1992, for 1993–1994 and for 1995. The results are $M_Z^{90-92} = 91.1922 \pm 0.0092$ GeV/c^2, $M_Z^{93-94} = 91.1915 \pm 0.0046$ GeV/c^2 and $M_Z^{95} = 91.1852 \pm 0.0043$ GeV/c^2. They are consistent within

Table 27: Correlations between energy points of the uncertainties on the theoretical predictions for the t channel.

	peak−3	peak−2	peak−1	peak	peak+1	peak+2	peak+3
peak−3	1.0	1.0	1.0	0.0	0.0	0.0	0.0
peak−2		1.0	1.0	0.0	0.0	0.0	0.0
peak−1			1.0	0.0	0.0	0.0	0.0
peak				1.0	0.0	0.0	0.0
peak+1					1.0	1.0	1.0
peak+2						1.0	1.0
peak+3							1.0

their estimated independent errors.

Theoretical luminosity error

The error of 0.06 % on the theoretical Bhabha cross section directly translates into an uncertainty on the hadronic peak cross section of 25 pb. The uncertainties on the other parameters are not significantly affected by this.

Theoretical uncertainty from t channel

Measurements of cross section and forward-backward asymmetries in the Bhabha channel are affected by uncertainties in the theoretical predictions of the t channel. These were assumed to have correlations between energy points of the form given by Table 27. Their contribution to the errors on R_{e} and $\mathrm{A}_{\mathrm{FB}}^{0,\mathrm{e}}$ were determined by repeating the fit to the data assuming the minimal and maximal t channel contributions within errors. This resulted in anticorrelated errors of ± 0.026 on R_{e} and ∓ 0.0013 on $\mathrm{A}_{\mathrm{FB}}^{0,\mathrm{e}}$. The terms in the matrix with correlation set to zero are essentially unknown. They were varied between -1 and 1 in order to assess the error.

Theoretical uncertainties

Theoretical errors in the fitting tools arise from QED radiative corrections, residual Standard Model dependencies, and ambiguities in the exact definition of the fitted pseudo-observables.

Corrections for QED initial state corrections are known to full second order [45] and leading logarithmic corrections of third order [46, 47]. The latter are implemented using two different exponentiation schemes, namely YFS [33]/JSW [46] and KF [48] in both ZFITTER and MIZA. The estimated error due to the missing higher order corrections including quark pair production on the peak cross sections is $\pm 2 \times 10^{-4}$ [49, 50]. Comparison of the different implementations of initial state pair production in ZFITTER and MIZA revealed differences of 0.3 MeV/c^2 in M_{Z} and 0.5 MeV in Γ_{Z}. These differences are taken as the error estimates.

Changes of Standard Model parameters also influence the fit results. As the default values, the Higgs boson mass was set to $M_{\mathrm{H}} = 150$ GeV/c^2 and varied between 90 GeV/c^2 and 1000 GeV/c^2. The top quark mass was taken from recent measurements by CDF and DØ at the Tevatron as $M_{\mathrm{t}} = 174{\pm}5$ GeV/c^2 [51], and the electromagnetic coupling constant at the scale of the Z mass is $\alpha(M_{\mathrm{Z}})^{-1} = 128.886{\pm}0.090$ [52]. Uncertainties on other Standard Model parameters do not lead to visible effects on the fit results. Parameter variations are significant only for M_{Z}, which is sensitive to the precise energy dependence of the cross sections via the γZ interference term. In the Standard Model, this term is proportional to the product of the effective vector couplings of the initial and final state fermions; it therefore depends on the effective weak mixing angle, which itself is determined by the Standard Model parameters. The observed changes are ± 0.3 MeV/c^2 in M_{Z}, where the dominant effect comes from the unknown Higgs boson mass.

In addition to such "parametric" uncertainties, genuine theoretical errors may arise from the detailed treatment of the residual Standard Model dependencies. Their effect was estimated by comparing ZFITTER and TOPAZ0 for various options implemented in these programs, as suggested in Ref. [43]. The resulting uncertainty on the fitted pseudo-observables is dominated by the difference between TOPAZ0 and ZFITTER with default options in each program. They amount to at most 10 % of the total experimental error.

The importance of the exact definition of the fit parameters may also be estimated by comparison with the different and less model-dependent approach used by MIZA (Table 23). The differences in central values are of the same order of magnitude as the theoretical errors estimated above and small compared to the experimental errors.

13.3 Interpretation of results

By parameter transformation of the pseudo-observables, information on the decay widths of the Z to hadrons and leptons and on the vector and axial vector coupling constants of the Z to leptons are extracted.

13.3.1 Partial Z decay widths

From the parameters Γ_{Z}, σ^0_{had} and R_ℓ, for $\ell = \mathrm{e}, \mu, \tau$, together with their correlations, the partial decay widths into hadrons and leptons and the decay width into invisible particles, given by $\Gamma_{\mathrm{inv}} = \Gamma_{\mathrm{Z}} - \Gamma_{\mathrm{had}} - \Gamma_{\ell\ell}\ (3 + \delta_m)$, are determined. Here, $\delta_m = -0.0023$ is a small correction which accounts for the τ mass effect. The results are summarised in Table 28. The comparison of the partial decay widths of the Z into e, μ and τ shows good consistency with lepton universality.

13.3.2 Z decay to light neutrinos and limit on other invisible decay modes

To check whether the invisible width is completely explained by decays into the three neutrinos, the "number of neutrino species" N_ν is calculated according to

$$\frac{\Gamma_{\mathrm{inv}}}{\Gamma_{\ell\ell}} = N_\nu \left(\frac{\Gamma_\nu}{\Gamma_{\ell\ell}}\right)_{\mathrm{SM}} . \tag{18}$$

Table 28: Partial Z decay widths, obtained by parameter transformation from the nine- and five-parameter fits of Table 23.

	without	with
	lepton universality	
Γ_{had} (MeV)	1747.0±4.2	1744.0±3.4
Γ_{inv} (MeV)	495.7±3.7	499.1±2.5
$\Gamma_{\mathrm{inv}}/\Gamma_{\ell\ell}$	-	5.940±0.026
$\Gamma_{\ell\ell}$ (MeV)	-	84.02±0.15
Γ_{ee} (MeV)	83.88±0.19	-
$\Gamma_{\mu\mu}$ (MeV)	84.02±0.28	-
$\Gamma_{\tau\tau}$ (MeV)	84.38±0.31	-

The Standard Model value for the ratio of the partial widths to neutrinos and to charged leptons is 1.991±0.001, where the uncertainty arises from variations of the top quark mass within its experimental error and of the Higgs mass within 90 GeV/c^2 < M_{H} < 1000 GeV/c^2. With the measured value of $\Gamma_{\mathrm{inv}} \,/\, \Gamma_{\ell\ell} = 5.940 \pm 0.026$, the following result is obtained:

$$N_\nu = 2.983 \pm 0.013\,. \tag{19}$$

With $\Gamma_{\nu\nu}^{\mathrm{SM}} = 167.1 \pm 0.2$ MeV, the measurement of the invisible width can be turned into a limit on any non-Standard Model contribution to the invisible width,

$$\begin{aligned} \Gamma_{\mathrm{inv}}^{\mathrm{x}} &= \Gamma_{\mathrm{inv}} - 3\,\Gamma_{\nu\nu}^{\mathrm{SM}} \\ &= -2.2 \pm 2.5 \text{ MeV} \\ &< 3.7 \text{ MeV at } 95\,\% \text{ CL}\,, \end{aligned}$$

where $\Gamma_{\mathrm{inv}}^{\mathrm{x}}$ was allowed to take only positive values when deriving the limit.

13.3.3 Z couplings to charged leptons

Lepton universality is tested by fitting for individual effective couplings, $g_{V_{\mathrm{e}}}$, g_{V_μ}, g_{V_τ}, $g_{A_{\mathrm{e}}}$, g_{A_μ} and g_{A_τ}. The measurements described in this paper do not allow, by themselves, to determine the signs of the couplings. To derive them, the following procedure is followed. The sign of $g_{A_{\mathrm{e}}}$ is derived from the sign of the Z coupling to neutrinos, conventionally taken as positive, in $\mathrm{e}\overset{(-)}{\nu}_{\mathrm{e}}$ scattering experiments. The energy dependence of the muon and tau forward-backward asymmetries shows that g_{A_μ} and g_{A_τ} have the same sign as $g_{A_{\mathrm{e}}}$. This also solves the ambiguity between $g_{V_{\mathrm{f}}}$ and $g_{A_{\mathrm{f}}}$ showing that $g_{A_{\mathrm{f}}}$ is the larger coupling. Finally, the various asymmetry measurements (including the left-right asymmetry) demonstrate that $g_{V_{\mathrm{f}}}$ and $g_{A_{\mathrm{f}}}$ have the same sign for all leptons. The results are summarised in Table 29 and in Fig. 24.

The effective lepton couplings can be re-expressed in terms of the parameters $\rho_{\mathrm{eff}}^{\mathrm{lept}}$ and the effective weak mixing angle $\sin^2\theta_{\mathrm{eff}}^{\mathrm{lept}}$, by

$$\begin{aligned} g_{A_\ell} &= \sqrt{\rho_{\mathrm{eff}}}\, I_3\,, \\ g_{V_\ell} &= \sqrt{\rho_{\mathrm{eff}}}\,(I_3 - 2\,q\,\sin^2\theta_{\mathrm{eff}}^{\mathrm{lept}})\,, \end{aligned}$$

Table 29: Effective lepton vector and axial vector couplings

g_{V_e}	-0.0400 ± 0.0037	g_{A_e}	-0.50166 ± 0.00057
g_{V_μ}	-0.0362 ± 0.0061	g_{A_μ}	-0.50046 ± 0.00093
g_{V_τ}	-0.0361 ± 0.0068	g_{A_τ}	-0.50216 ± 0.00100
g_{V_μ}/g_{V_e}	0.91 ± 0.21	g_{A_μ}/g_{A_e}	0.9976 ± 0.0022
g_{V_τ}/g_{V_e}	0.90 ± 0.22	g_{A_τ}/g_{A_e}	1.0010 ± 0.0024
g_{V_ℓ}	-0.0383 ± 0.0018	g_{A_ℓ}	-0.50150 ± 0.00046

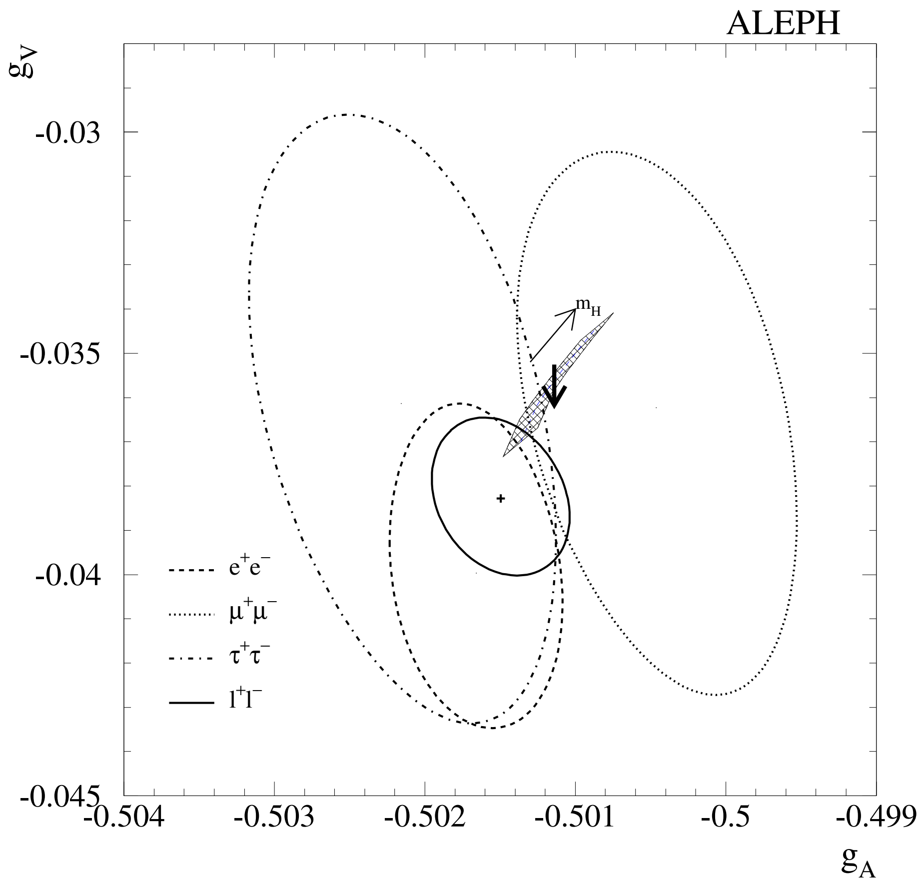

Figure 24: Effective lepton couplings. Shown are the one-σ contours (39.3 % CL). The shaded area indicates the Standard Model expectation for $M_t = 174 \pm 5$ GeV/c^2 and $90 < M_H/\mathrm{GeV}/c^2 < 1000$; the vertical arrow shows the change if the electromagnetic coupling constant is varied within its error. This figure shows that the data favour a light Higgs boson.

where I_3 is the third component of the weak isospin and q is the electric charge.

Information on the ρ parameter comes essentially from the lepton partial width with a small contribution from the invisible width. The peak asymmetries depend on the ratio of effective vector and axial vector couplings and hence on the effective weak mixing angle. The results are

$$\begin{aligned} \rho_{\mathrm{eff}}^{\mathrm{lept}} &= 1.0064 \pm 0.0018\,, \\ \sin^2\theta_{\mathrm{eff}}^{\mathrm{lept}} &= 0.23089 \pm 0.00089\,. \end{aligned}$$

The value of the ρ parameter differs from its tree-level value of one by 3.6 standard deviations. This measurement alone therefore shows the existence of genuine electroweak corrections.

13.4 Standard Model fits

As a last step, fits with ZFITTER and TOPAZ0 were performed to the pseudo-observables using the Standard Model, with the Z mass M_{Z}, the top quark mass M_{t}, and the strong coupling constant $\alpha_s(M_{\mathrm{Z}})$ as free parameters. Information on the Higgs boson mass from the ALEPH results alone is marginal and strongly correlated with M_{t}; M_{H} is therefore fixed in the fit, or an external constraint within errors on M_{t} to its present experimental value is applied. Here, constraining a parameter means that a measurement of that parameter is added as a data point, while it is still treated as a variable in the fit. The electromagnetic coupling constant at the scale of the Z mass is constrained to $\alpha(M_{\mathrm{Z}})^{-1} = 128.886 \pm 0.090$ [52]. All other input parameters, such as the fermion masses and the Fermi constant G_{F}, are fixed to their present experimental values [53].

As a cross-check, an alternative procedure was also used based on a direct Standard Model fit of the cross sections and asymmetries, thus avoiding the intermediate step of the five or nine pseudo-observables. The resulting fit, with a constrained top quark mass, has a χ^2 per degree of freedom of 174/182, which corresponds to a confidence level of 65 %, i.e., the measurements are in good agreement with the Standard Model. Compared to the fit that uses the five parameter results as input, the central values and errors of the Higgs boson mass and the strong coupling constant are found to be in excellent agreement. The differences amount to 2 % of the error for $\alpha_s(M_{\mathrm{Z}})$ and less than 1 % of the error for $\log_{10}[M_{\mathrm{H}}/(\mathrm{GeV}/c^2)]$. However, the Z mass is 0.5 MeV/c^2 lower, which is largely explained by the low central value of the Higgs mass favoured by these data, while M_{H} was fixed to 150 GeV/c^2 in the fit to the pseudo-observables.

13.4.1 The coupling constant of the strong interaction and the top quark mass

Within the Standard Model framework, the lineshape and asymmetry measurements are particularly sensitive to the strong coupling constant and to the top quark mass. This is shown in Fig. 25, which compares the ALEPH results for a fixed Higgs mass with the present world averages. The results are

$$\begin{aligned} M_{\mathrm{t}}(\mathrm{GeV}/c^2) &= 192^{+12}_{-13} + 23\,\log_{10}\left[\frac{M_{\mathrm{H}}}{150\,\mathrm{GeV}/c^2}\right] \\ \alpha_s(M_{\mathrm{Z}}) &= 0.114 \pm 0.004 \pm 0.002_{\mathrm{QCD}} + 0.005\,\log_{10}\left[\frac{M_{\mathrm{H}}}{150\,\mathrm{GeV}/c^2}\right]. \end{aligned}$$

Here, the second error on $\alpha_s(M_{\rm Z})$ reflects uncertainties on the QCD part of the theoretical prediction on $\Gamma_{\rm had}$ [54]. As a result of recent theoretical improvements, uncertainties arising from the treatment of non factorisable QED and QCD contributions and from deviations between different electroweak calculations [55] have become negligible.

13.4.2 The Higgs boson mass

With the full set of five or nine measured parameters as inputs and the top quark mass constraint, the Higgs mass can also be left as a free parameter in the fit. In addition, the strong coupling constant is constrained to $\alpha_s(M_{\rm Z}) = 0.119 \pm 0.002$ [53]. The fit results are shown in Table 30. The constraining measurements $M_{\rm t}$, $\alpha_s(M_{\rm Z})$ and $\alpha(M_{\rm Z})$ improve slightly if combined with the results reported here.

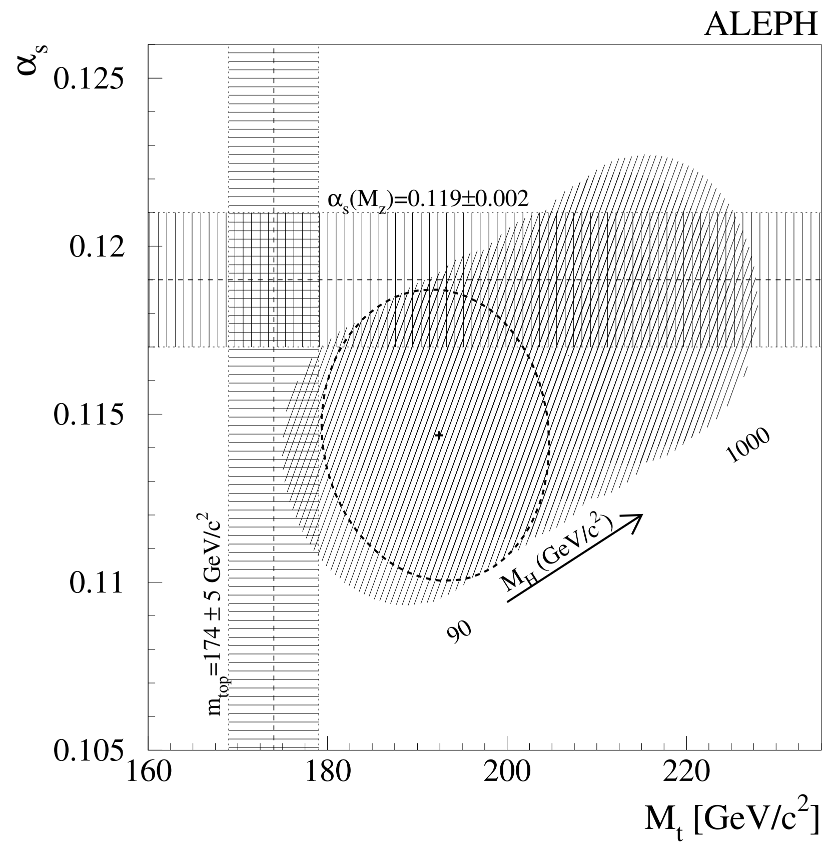

Figure 25: One-σ contour lines in the plane of the top quark mass versus the strong coupling constant, for $M_{\rm H} = 150$ GeV$/c^2$. The horizontal and vertical bands represent the world averages of other measurements. The shaded area indicates variations of the Higgs boson mass between 90 GeV$/c^2$ and 1000 GeV$/c^2$.

Table 30: Standard Model parameters determined from the five parameter fit results, with external experimental constraints on the top quark mass and the electromagnetic and strong coupling constants.

Standard Model fit results	
$M_{\mathrm{Z}}(\mathrm{GeV}/c^2)$	91.1886±0.0031
$M_{\mathrm{t}}(\mathrm{GeV}/c^2)$	175.1±4.7
$\alpha_s(M_{\mathrm{Z}})$	0.1180±0.0018
$\alpha(M_{\mathrm{Z}})$	128.886±0.088
$\log_{10}M_{\mathrm{H}}/\mathrm{GeV}/c^2$	1.72±0.56
$M_{\mathrm{H}}(\mathrm{GeV}/c^2)$	$52\ ^{+140}_{-38}$

Neglecting the lower limit on the Higgs boson mass of $\sim$95 GeV/c^2 from direct searches [56], the one-sided 95% confidence level upper limit on M_{H} is 360 GeV/c^2 .

14 Conclusions

From the data collected by ALEPH at LEP, corresponding to an integrated luminosity of 160 pb^{-1}, the following parameters of the Z resonance are measured if lepton universality is assumed:

$$\begin{aligned} M_{\mathrm{Z}} &= (91.1885 \pm 0.0031)\,\mathrm{GeV}/c^2, \\ \Gamma_{\mathrm{Z}} &= (2.4951 \pm 0.0043)\,\mathrm{GeV}, \\ \sigma^0_{\mathrm{had}} &= (41.559 \pm 0.058)\,\mathrm{nb}, \\ R_\ell &= 20.725 \pm 0.039. \end{aligned}$$

The corresponding number of light neutrino species is $N_\nu = 2.983 \pm 0.013$. From the ratio of the hadronic and leptonic widths, the pole cross section and the Z width, the strong coupling constant is measured to be $\alpha_s(M_{\mathrm{Z}}) = 0.114 \pm 0.004 \pm 0.002_{\mathrm{QCD}} + 0.005\ \log_{10}\left[\frac{M_{\mathrm{H}}}{150\,\mathrm{GeV}/c^2}\right]$. The lepton forward-backward asymmetry is measured to be $\mathrm{A}^{0,\ell}_{\mathrm{FB}} = 0.0173 \pm 0.0016$, from which the effective weak mixing angle is derived: $\sin^2\theta^{\mathrm{lept}}_{\mathrm{eff}} = 0.23089 \pm 0.00089$. The measurement of the leptonic partial width $\Gamma_{\ell\ell} = 84.02 \pm 0.15$ MeV leads to a determination of the effective ρ parameter $\rho^{\mathrm{lept}}_{\mathrm{eff}} = 1.0064 \pm 0.0018$.

All these results are in good agreement with the measurements by the other LEP and SLC experiments [57–60]. The data support the Standard Model and favour a light Higgs boson.

Acknowledgements

It is a pleasure to congratulate our colleagues from the accelerator divisions for the successful operation of LEP and for the precise measurement of the LEP energy. We wish to thank

D. Bardin, W. Beenakker, S. Jadach, G. Passarino, M. Skrzypek, B.F.L. Ward and Z. Wąs for many discussions about theoretical issues, advice and practical help. We are indebted to the engineers and technicians at our home institutes without whose dedicated help this work would have not been possible. Those of us from non-member states wish to thank CERN for its hospitality and support.

References

[1] ALEPH Collaboration, *Measurement of Electroweak parameters from Z decays into fermion pairs*, Z. Phys. **C48** (1990) 365.

[2] ALEPH Collaboration, *Improved measurements of Electroweak parameters from Z decays into fermions pairs*, Z. Phys. **C53** (1992) 1.

[3] ALEPH Collaboration, *Update of Electroweak parameters from Z decays*, Z. Phys. **C60** (1993) 71.

[4] ALEPH Collaboration, *Z Production Cross Sections and Lepton Pair Forward-Backward Asymmetries*, Z. Phys. **C62** (1994) 539.

[5] ALEPH Collaboration, *ALEPH: A detector for electron-positron annihilation at LEP*, Nucl. Instrum. Methods **A294** (1990) 121.

[6] ALEPH Collaboration, *Performance of the ALEPH detector at LEP*, Nucl. Instrum. Methods **A360** (1995) 481.

[7] B. Mours *et al.*, Nucl. Instrum. Methods **A379** (1996) 101.

[8] D. Bederede *et al.*, *SICAL - a high precision silicon-tungsten calorimeter for ALEPH*, Nucl. Instrum. Methods **A365** (1995) 117.

[9] ALEPH Collaboration, *Tau leptonic branching ratios*, Z. Phys. **C70** (1996) 561.

[10] ALEPH Collaboration, *Improved Tau Polarisation Measurement*, Z. Phys. **C69** (1996) 183.

[11] ALEPH Collaboration, *Tau hadronic branching ratios*, Z. Phys. **C70** (1996) 579.

[12] T. Camporesi *et al.*, *Report from the Bunch Train Working Group*, CERN/LEPC 94-13, 5 September 1994.

[13] LEP Energy Working Group, ALEPH, DELPHI, L3 and OPAL Collaborations, L. Arnaudon *et al.*, Phys. Lett. **B307** (1993) 187;
LEP Energy Working Group, L. Arnaudon *et al.*, *The Energy Calibration of LEP in 1992*, CERN SL/93-21 (DI), April 1993.

[14] LEP Energy Working Group, R. Assmann *et al.*, Z. Phys. **C66** (1995) 567;
Calibration of centre-of-mass energies at LEP1 for precise measurements of Z properties, Eur. Phys. J. **C6** (1999) 187.

[15] L. Arnaudon *et al.*, Phys. Lett. **B284** (1992) 431.

[16] A. Blondel, *Systematic Uncertainties on LEP Electroweak Observables Due to Unknown Residual Longitudinal Beam Polarisation*, http://www.cern.ch/LEPECAL/reports/reports.html, to be submitted to a publication.

[17] J.E. Campagne and R. Zitoun, Z. Phys. **C43** (1989) 469.

[18] T. Sjöstrand, Comp. Phys. Comm. **82** (1994) 74.

[19] G. Marchesini *et al.*, Comp. Phys. Comm. **67** (1992) 465.

[20] L. Lönnblad, Comp. Phys. Comm. **71** (1992) 15.

[21] H. Anlauf *et al.*, Comp. Phys. Comm. **79** (1994) 466.

[22] S. Jadach, B.F.L. Ward and Z. Wąs, Comp. Phys. Comm. **66** (1991) 276; **79** (1994) 503;
S. Jadach *et al.*, Comp. Phys. Comm. **76** (1993) 361.

[23] S. Jadach, B.F.L. Ward and Z. Wąs, Phys. Lett. **B449** (1999).

[24] J.A.M. Vermaseren, Proceedings of the IV International Workshop on Gamma Gamma Interactions, eds. G. Cochard and P. Kessler (1980).

[25] ALEPH Collaboration, *An Experimental Study of $\gamma\gamma \rightarrow$ hadrons at LEP* Phys. Lett. **B355** (1995) 595.

[26] J.M. Hilgart, R. Kleiss and F. Le Diberder, Comp. Phys. Comm. **75** (1993) 191.

[27] G. Barbiellini, B. Borgia, M. Conversi and R. Santonico, Atti Accad. Naz. Lincei **44** (1968) 233;
J.F. Crawford, E.B. Hughes, L.H. O'Neill and R.E. Rand, Nucl. Instrum. Methods **127** (1975) 173.

[28] ALEPH Collaboration, *Measurement of the absolute luminosity with the ALEPH detector*, Z. Phys. **C53** (1992) 375.

[29] S. Jadach *et al.*, Phys. Lett. **B353** (1995) 362;
S. Jadach *et al.*, Phys. Lett.**B353** (1995) 349.

[30] S. Jadach *et al.*, BHLUMI 4.04, Comp. Phys. Comm. **102** (1997) 229;
S. Jadach and O. Nicrosini, *Event generators for Bhabha scattering*, in *Physics at LEP2*, CERN 96-01 Vol. 2, February 1996.

[31] B.F.L. Ward, S. Jadach, M. Melles and S.A. Yost, UTHEP-98-0501, *New Results on the Theoretical Precision of the LEP/SLC Luminosity*, September 1998.

[32] M. Böhm, A. Denner and W. Hollik, Nucl. Phys. **B304** (1988) 687; F.A. Berends, R. Kleiss and W. Hollik, Nucl. Phys. **B304** (1988) 712; Computer program BABAMC, courtesy of R. Kleiss.

[33] D.R. Yennie, S.C. Frautschi and H. Suura, Ann. Phys. (NY) **13** (1961) 379.

[34] W. Beenakker and B. Pietrzyk, Phys. Lett. **B296** (1992) 241; **B304** (1993) 366.

[35] S. Jadach, B. Pietrzyk, E. Tournefier, B.F.L. Ward and Z. Wąs, *Initial-Final State Interference in the LEP Z Lineshape Fits*, preprint LAPP-EXP-99.05, to be submitted to Phys. Lett..

[36] W. Beenakker, F.A. Berends and S.C. van der Marck, Nucl. Phys. **B349** (1991) 323; Phys. Lett. **B251** (1990) 299.

[37] W. Beenakker and G. Passarino, hep-ph/9710376, Phys. Lett. **B425** (1998) 199.

[38] ALEPH Collaboration, *Study of the four-fermion final state at the Z resonance*, Z. Phys. **C66** (1995) 3.

[39] ALEPH Collaboration, *A study of tau decays involving eta and omega mesons*, Z. Phys. **C74** (1997) 263.

[40] D. Bardin *et al.*, Z. Phys. **C44** (1989) 493; Comp. Phys. Comm. **59** (1990) 303; Nucl. Phys. **B351**(1991) 1; Phys. Lett. **B255** (1991) 290; CERN-TH 6443/92 (May 1992) and hep-ph/9412201; *ZFITTER v.6.10 A Semi-Analytical Program for Fermion Pair Production in* $\mathrm{e^+e^-}$ *Annihilation*, DESY 99-070, June 1999.

[41] ALEPH Collaboration, *Complementary information on the paper "Measurement of the Z Resonance Parameters at LEP"*, http://alephwww.cern.ch/ALPUB/paper/paper_99.html, ALEPH 99-086, PHYSIC 99-033.

[42] Ll. Garrido *et al.*, Z. Phys. **C49** (1991) 645;
M. Martinez and F. Teubert, Z. Phys. **C65** (1995) 267, updated with results summarized in [50] and [61].

[43] D. Bardin, G. Passarino and M. Grünewald, *Precision Calculation Project Report*, hep-ph/9902452 .

[44] G. Montagna *et al.*, Nucl. Phys. **B401** (1993) 3; Comp. Phys. Comm. **76** (1993) 328; **93** (1996) 120;
G. Montagna, O. Nicrosini, G. Passarino and F. Piccinini, hep-ph/9804211.

[45] F.A. Berends, W.L. van Neerven and G.J.H. Burgers, Nucl. Phys. **B297** (1988) 429.

[46] S. Jadach, M. Skrzypek and B.F.L. Ward, Phys. Lett. **B257** (1991) 173;
M. Skrzypek and S. Jadach, Z. Phys. **C49** (1991) 577;
M. Skrzypek, Acta Phys. Pol. **B23** (1992) 135.

[47] G. Montagna *et al.*, Phys. Lett. **B406** (1997) 243.

[48] E.A. Kuraev and V.S. Fadin, Sov. J. Nucl. Phys. **41** (1985)466.

[49] M. Martinez and B. Pietrzyk, Phys. Lett. **B324**(1994)492.

[50] S. Jadach, B. Pietrzyk and M. Skrzypek, Phys. Lett. **B456** (1999) 77.

[51] W. Yao, CDF Collaboration, Proceedings 29th International Conference on High Energy Physics (ICHEP 98), Vancouver, B.C., Canada, 23–29 July 1998;
E. Barberis, DØ Collaboration, Proceedings 29th International Conference on High Energy Physics (ICHEP 98) Vancouver, B.C., Canada, 23–29 July 1998.

[52] S. Eidelmann and F. Jegerlehner, Z. Phys. **C67** (1995) 585;
H. Burkhardt and B. Pietrzyk, Phys. Lett. **B356** (1995) 398;
M. Steinhauser, Phys. Lett. **B249** (1998) 158.

[53] C. Caso *et al.* (Particle Data Group), Eur. Phys. J. **C3** (1998) 1.

[54] T. Hebbeker, M. Martinez, G. Passarino and G. Quast, Phys. Lett. **B331** (1994) 165, and references therein.

[55] D. Bardin and G. Passarino, *Upgrading of Precision Calculations for Electroweak Observables*, hep-ph/9803425 .

[56] M. Felcini, talk at the XXXIV Rencontres de Moriond on ElectroWeak Interactions and Unified Theories, 13–20 March 1999, Les Arcs, France.

[57] DELPHI Collaboration, *Improved Measurements of Cross Sections and Asymmetries at the Z Resonance*, Nucl. Phys. **B418** (1994) 403.

[58] L3 Collaboration, *Measurement of Cross Sections and Leptonic Forward-Backward Asymmetries at the Z Pole and Determination of Electroweak Parameters*, Z. Phys. **C62** (1994) 551.

[59] OPAL Collaboration, *Improved Measurements of the Neutral Current from Hadron and Lepton Production at LEP*, Z. Phys. **C61** (1994) 19.

[60] SLD Collaboration, *An Improved Measurement of the Left-Right Z^0 Cross-Section Asymmetry*, Phys. Rev. Lett. **78** (1997) 2075.

[61] *Reports of the working group on precision calculations for the Z resonance*, eds. D. Bardin, W. Hollik and G. Passarino, CERN Yellow Report 95-03, Geneva, 31 March 1995 and references therein.